UCSF

UC San Francisco Electronic Theses and Dissertations

Title

Immune-vascular Interactions in the Prenatal Brain: Linking Transcriptomics with Functional Implications

Permalink

https://escholarship.org/uc/item/167118dq

Author

Chen, Jiapei

Publication Date

2023

Peer reviewed|Thesis/dissertation

Immune-vascular Interactions in the Prenatal Brain: Linking Transcriptomics with Functional
 Implications

by
Jiapei Chen

DISSERTATION
Submitted in partial satisfaction of the requirements for degree of
DOCTOR OF PHILOSOPHY

in

Biomedical Sciences

in the

GRADUATE DIVISION
of the
UNIVERSITY OF CALIFORNIA, SAN FRANCISCO

Approved:

DocuSigned by:

Anna Victoria Molofsky _____   Anna Victoria Molofsky
7148719D502F43A...   Chair

DocuSigned by:

_____   Arnold Kriegstein
B98B956E784E486...

_____

DocuSigned by:

Michael Oldham _____   Michael Oldham
DocuSigned by: ...430...

DocuSigned by:

Eric Huang _____   Eric Huang
9A805C3F0428410...   Committee Members

Dedication

Mom, I owe my education to your persistence and inspiration.

You are dearly missed in every aspect of my life.

Acknowledgements

First and foremost, my doctoral journey would not have been possible without the generous support and guidance of my mentor, Dr. Eric Huang. I had not known anything about microglia or the germinal matrix before coming to UCSF, and it was thanks to his enthusiasm in these research topics that I became engrossed in the beauty of microglia and their "hands" in almost every process of neurodevelopment. Eric has taught me much about human neuroanatomy, often showing me his 3D model of the human brain in his office. I am extremely grateful for the opportunity to conduct research with Eric on prenatal brain injury, which is a condition that my sister suffers from and I hope that one day we would develop therapeutic cures for. In addition to providing me with the resources to be successful, Eric has been unwavering in his belief in me and that alone has been a tremendous source of motivation. Outside of lab work, I will miss chatting with Eric about indie movies and the food scene in SF.

My scientific journey at UCSF is also graciously supported by my thesis committee: Drs. Arnold Kriegstein, Anna Molofsky, and Michael Oldham. Thank you for sharing your expertises in brain development, neuroimmunology, and bioinformatics, providing feedback for my manuscript, and helping my project evolve into its final form.

Many collaborators have worked diligently for parts of my thesis project, and I would like to give my sincere thanks to all of their hard work and time invested. To start with, my collaborator since rotating at the Huang lab, Dr. Elizabeth Crouch, has been so thoughtful and supportive, both in my research and career development. I am very grateful to have you as my mentor and friend. My appreciation also extends to members of the Crouch lab, including Edward, Janeth, Loukas, and Kaylee, all of whom have

endured late nights with me in the lab with good humor. Many thanks also to the labs of Drs. Julieta Alfonso, Jose Manuel Garcia-Verdugo, Matthew Kutys, Maria Lehtinen, and Alexis Combes, for their experimental expertises in improving my thesis project.

I am also grateful for the daily support from people in the Huang lab, past and present. In particular, Jennifer, Avani, and Shamari have directly worked with me on my project and I am thankful for their assistance. Everyone in the Huang lab has been welcoming and generous, offering help when needed and providing valuable feedback during our weekly lab meetings.

Beyond research, I am lucky to have a group of friends that I can laugh with and grind through the hard times. Thank you David, Tyler, and Irene from my UCSF PhD cohort, with whom I have shared many wonderful meals, home-cooked or otherwise. We first bonded over eating spicy chicken wings (a la the Hot Ones challenge) and the rest is history. Thank you Naznin, my fellow PhD student in the Huang lab, for the fun times exploring our creativity through figure drawing or checking out the latest exhibits at art museums. Thank you to my regular bar trivia groups at Blackthorn and Dogpatch Saloon, which include and not limited to Kadellyn, Mohini, Max, and friends, and may our Smooth Brain team take the crown someday so we can feel accomplished with the amount of random knowledge in our smooth brains.

Outside of UCSF, I would also like to thank the continued support of friends I have made at every stage of life, dating back to elementary school. These following mentions are by no means exhaustive, and I appreciate every little kindness being offered to me in the past six years of graduate school. First, thank you to my comrade Theo, whom I have known since high school and shamelessly solicited feedback and

Contributions

Chapters 1, 4, and 5 were written by Jiapei Chen.

Chapter 2 and 3 was adapted from the following article, currently under review:

Chen, J., Crouch, E.E., Zawadzki, M.E., Jacobs, K.A., Mayo, L.N., Choi, J.J., Shaikh, S., Tsui, J., Gonzalez-Granero, S., Waller, S., Kelekar, A., Kang, G., Valenzuela, E.J., Birrueta, J.O., Diafos, L.N., Wedderburn-Pugh, K., Di Marco, B., Xia, W., Han, C.Z., Coufal, N.G., Glass, C.K., Fancy, S.P.J., Alfonso, J., Kriegstein, A.R., Oldham, M.C., Garcia-Verdugo, J.M., Kutys, M.L., Lehtinen, M.K., Combes, A.J., Huang, E.J. (2023). Proinflammatory milieu disrupts homeostatic microglia-vascular interactions to promote germinal matrix hemorrhage.

Additional author contributions for Chapter 2 and 3 are described in the Acknowledgements and Author Contributions section at the end of Chapter 3.

Epigraph

You know the fishermen sometimes find horses out at sea. A man I know towed a colt in one time and the horse lay down for a long time before he got up. And he was perfect. Tiredness was all it was, after being out so long.

Claire Keegan, *Foster*

Immune-vascular Interactions in the Prenatal Brain:

Linking Transcriptomics with Functional Implications

by Jiapei Chen

Abstract

My thesis investigates the role of brain-resident immune cells, particularly microglia, in angiogenesis during brain development and their impact on germinal matrix hemorrhage (GMH) in premature infants. While microglia were postulated to promote cerebrovascular formation, the exact mechanism remains unclear. To address this question, I developed a multidisciplinary approach to examine the distribution, transcriptomics, and functions of immune cell subtypes in distinct brain regions and ages. My findings showed that prenatal microglia age-dependently interact with nascent vasculature and that ablation of these cells reduces angiogenesis in the ganglionic eminences (GE), which correspond to the human germinal matrix. Furthermore, single-cell transcriptomics and flow cytometry showed that distinct subsets of immune cells employ diverse signaling mechanisms to promote vascular formation in the GE. In contrast, immune cells from preterm infants with GMH included neutrophils/monocytes that produce bactericidal factors and chemokine, which can disrupt vascular integrity and lead to GMH. Finally, my results showed that changes in microglia states adversely affect neural progenitor density and positioning. Taken together, this project offers insights into the complex tripartite interplay among immune, vascular, and neuronal cells during brain development, shedding light on their implications for GMH pathogenesis.

Table of Contents

List of Figures

Chapter 1: Background

Life Cycle of Microglia

Microglia are brain-resident macrophages implicated in a variety of functions during brain development, including synapse formation, neurogenesis, and angiogenesis. Recent studies have done tremendous work using fate-mapping and single-cell RNA sequencing (scRNA-seq) to elucidate the origins of microglia, which are not born in the brain parenchyma. Instead, they originate from erythromyeloid progenitors (EMPs; c-Kit$^+$ CD45$^-$ F4/80$^-$ CD206$^-$) in the yolk sac and colonize the brain between embryonic days 8.5 and 9.5 (E8.5-9.5), which has been extensively proven using lineage tracing, parabiosis, and neonatal bone marrow transplant studies (Ginhoux et al., 2010; Li and Barres, 2018). In particular, fate-mapping using a tamoxifen pulse at E7-7.25 during primary EMP generation in Runx1-CreERT x LacZ mice labels only microglia and not other tissue-resident macrophages (Ginhoux et al., 2010). EMP-derived yolk sac macrophages then travel via blood circulation to reach the brain, driven by CX3CR1 signaling. In CX3CR1 knockout mice, more macrophage precursors accumulate in the yolk sac and fetal liver instead of becoming tissue-resident macrophages (Li and Barres, 2018). Matrix metalloproteinases (MMPs) also help microglia precursors to invade the developing brain, particularly MMP8 and MMP9. With inhibitors against MMPs at E14.5, mice produce fewer CD45$^+$ CX3CR1$^+$ cells and have dysregulated microglia distribution (Kierdorf et al., 2012).

In the human brain, microglia are observed at relatively earlier developmental stages at 4.5-5.5 gestational weeks (GW) close to the meninges, choroid plexus, and in the ventricular zone (Monier et al., 2006). Notably, 5.5 GW coincides with peak hematopoiesis and microglia appear in the brain before the formation of blood vessels. However, a significant population of amoeboid microglia are found to be closely associated with the endothelium around 10 GW (Menassa et al., 2018).

Once inside the brain, the local environment further supports microglia differentiation. Important factors in this process include IRF8, TGFβ, SALL1, and NRROS. IRF8 is a transcription factor required for the maturation of migratory macrophage precursors that contribute to microglia as well as meningeal macrophages (Li and Barres, 2018). TGFβ is essential but not sufficient to promote microglia specification and homeostasis, as supported by *in vitro* studies and mouse models lacking either *Tgfbr1* or *Tgfbr2* (Li and Barres, 2018). Similarly, in mouse models lacking microglia-specific *Sall1* or containing mutant NRROS, microglia are found to downregulate canonical genes such as *Tmem119* and *P2ry12* while upregulating other tissue macrophage-specific genes, such as *Mrc1*, *Cd74*, *Stard13*, *Cd69*, and *Ahr* (Li and Barres, 2018; Buttgereit et al., 2016). Interestingly, SALL1 is expressed only in microglia and not in other mononuclear phagocytes or infiltrating myeloid cells such as neutrophils, nor could its expression be induced in microglia derived from iPSCs in organoids (Buttgereit et al., 2016; Han et al., 2023). Thus, the true microglia identity is maintained by an intricate interplay between their ontogeny from the yolk sac and external factors produced by the brain environment, requiring both nature and nurture. Indeed, microglia are quick to shed their transcriptional and epigenetic identity once

separated from the brain niche, and bone marrow-derived monocytes cannot fully attain microglia differentiation even after transplanted into adult brain (Gosselin et al., 2017).

Microglia density is the highest near the developing white matter tracts, as well as at the cortical plate-subplate junction around 9-13 GW in the prenatal human brain (Verney et al., 2010). It remains unclear why microglia are accumulated at certain regions in the developing brain, but cues such as IL-34, CSF1, CXCL12, and CX3CL1 have been suggested to attract microglia (Casano et al., 2016).

Under homeostasis in the postnatal and adult brain, microglia self-maintain their numbers independently of external contributions including circulating monocytes and bone marrow-derived cells, as shown by hematopoietic cell transplantation, bone marrow chimera, and parabiotic mouse models (Ginhoux et al., 2010). Curiously, different brain regions maintain different microglia turnover rates, with the highest in the olfactory bulb at 8-month-long full turnover rate, in contrast to cortical microglia that are long-lived with a median lifespan of more than 15 months (Li and Barres, 2018).

Microglia vs Perivascular Macrophages

It is now recognized that microglia are not the only resident immune cells in the brain. In addition, there are several well-documented border-associated macrophages (BAMs), including choroid plexus, meningeal, and perivascular macrophages. For the scope of this paper, I will focus on perivascular macrophages, and how they may differ from canonical microglia.

First, perivascular macrophages have been debated to have different origins from microglia. A recent study elucidated that perivascular macrophages differentiate

from perinatal meningeal macrophages shortly after birth, using markers *Hexb* and *Mrc1* (CD206) in lineage-tracing (Masuda et al., 2022). This study further showed that perivascular macrophage differentiation depends on integrins and the presence of arterial vascular smooth muscle cells (VSMCs). After postnatal development, perivascular macrophages preferentially localize around $\alpha SMA^+ SOX17^+ TfR^-$ arteries and arterioles, and are rarely found near αSMA^+ capillaries, veins, and venules (Masuda et al., 2022). In humans, however, it is unknown whether perivascular macrophages follow the same developmental trajectory as that observed in mice.

Next, perivascular macrophages express distinct markers from microglia. Based on extensive studies in mice, perivascular macrophages are distinguished by markers like *Mrc1*, *Lyve1*, *Cd163*, $CD45^{high}$, $MHC-II^{high}$. In contrast, microglia express markers such as *Tmem119*, *Hexb*, *P2ry12*, *Sall1*, $CD45^{low}$, $MHC-II^{low}$ (Masuda et al., 2022; Li and Barres, 2018).

Finally, perivascular macrophages and microglia occupy different milieu during development. $CD206^+$ perivascular macrophages are rarely found in the perivascular compartment until after birth at P10 in mice and 41 GW in humans (Masuda et al., 2022). Instead, the perivascular compartment is occupied by $P2RY12^+ CD206^-$ microglia in the embryonic brain. Electron microscopy has revealed a primitive blood-brain barrier at E14.5, lacking basal lamina and VSMCs in arteries and arterioles (Masuda et al., 2022). This further lends to the hypothesis that microglia precursors can use blood vessels as one of their pathways to colonize the brain.

Microglia Isolation and Heterogeneity

To interrogate diversity within microglia, it is important to first clarify the criteria used by previous literature to isolate microglia. One of the first studies to isolate human microglia used CD11b$^+$ CD45^{low} CD64$^+$ CX3CR1^{high} in FACS (Gosselin et al., 2017).

To isolate mouse microglia, c-Kit$^-$ CD45$^+$ was used for gating embryonic microglia at E14.5, and CD11b$^+$ CD45^{low} was used for gating postnatal and aging microglia (Li et al., 2019). In contrast, CD11b$^+$ CD45^{high} was used for gating non-microglia myeloid cells.

Human prenatal and early postnatal microglia contain diverse subtypes. Using Weighted Gene Co-expression Network Analysis (WGCNA), a recent study reported that prenatal microglia are enriched in genes related to cell cycling, phagocytosis and oxidative phosphorylation, whereas postnatal microglia are enriched in genes related to cytokine signaling, myeloid activation, and MHC protein complex (Han et al., 2023). Applying scRNA-seq on a combination of pre- and postnatal microglia samples, this study highlighted subtypes related to immune modulation (marker genes: *Lgals3*, *Ucp2* for prenatal microglia; *Cd83*, *Il18*, *Ch25h* for postnatal microglia), lipid metabolism (*Fabp7*), interferon response (*Ifit1*, *Ifit3*, *Mx1*), and neural progenitors (*Dcx*, *Sox11*). The last subtype co-expressing neural progenitor genes may constitute microglia that are closely attached to or have phagocytosed neural progenitors, though these possibilities remain to be investigated. This dataset also includes some peripheral immune cell subtypes including monocytes (*Lyz*) and border-associated macrophages (*Lyve1*).

Several subtypes of embryonic and early postnatal microglia have also been identified in mice. In particular, proliferative-region-associated microglia (PAM) are highly enriched at this developmental stage, showing low expressions of microglia

homeostatic genes and enrichment of disease-associated microglia (DAM) genes such as *Spp1, Gpnmb, Igf1, Clec7a, Lpl, Lgals1*, and *Apoe* (Li et al., 2019; Hammond et al., 2019). Amoeboid CLEC7A$^+$ PAM are found at high density in the subventricular zone, corpus callosum, and cerebellar white matter regions, where they often locate close to apoptotic oligodendrocytes and have the ability to phagocytose pyknotic nuclei. Their density in these regions peak at P3-7 (Ueno et al., 2013). Interestingly, scRNA-seq in embryonic and early postnatal microglia also show more "contamination" of neuronal and endothelial cell-specific genes, perhaps indicating their phagocytosis of these cell types or close association with them. Microglia at E14.5 and P7 are also highly proliferative and upregulate metabolic pathways such as oxidative phosphorylation, glycolysis, and beta oxidation (Li et al., 2019; Hammond et al., 2019). In contrast, adult mouse microglia show limited heterogeneity across different brain regions.

Mouse Models of Microglia Depletion

Since this thesis project uses mouse models of microglia depletion, here is an overview of different options used by previous studies.

One of the most common models to deplete and even ablate microglia is based on *Csf1r*. CSF1R is required for the proliferation, differentiation, and survival of yolk sac macrophages, as well as maintenance of adult microglia. Thus, mice with mutant CSF1R lack yolk sac and tissue-resident macrophages, including microglia. Current models with loss of CSF1R expression include Csf1r^{dex5} (loss of exon 5 in *Csf1r*) and Csf1r$^{\Delta FIRE}$ (loss of intron 2 in *Csf1r*, a site of a super-enhancing Fms intronic regulatory element where many macrophage transcription factors bind to).

Similarly, administration of a CSF1R blocking antibody at E6.5 and E7.5 eliminates fetal macrophages, including microglia (Squarzoni et al., 2014). Intriguingly, this is only a transient depletion, since microglia repopulate by P7. Pharmacologically, two CSF1R inhibitors have been widely tested: PLX3397 and its improved version, PLX5622. Continuous treatment of PLX3397 in chow over 7 days can eliminate up to 99% of adult microglia. PLX5622 is superior to PLX3397 due to its higher specificity to CSF1R against other receptor kinases such as FLT3, PDGFR, and KIT (Spangenberg et al., 2019). PLX5622 also has a higher brain penetration rate at 20%, compared to 5% for PLX3397. Pharmacological approaches like these also enable studies on repopulating microglia-like populations after stopping the inhibitor administration.

CSF1R most likely acts downstream of the transcription factor PU.1, as PU.1-deficient mice lack microglia, tissue-resident macrophages, and circulating monocytes. Mice lacking CSF1 or IL-34, which are both ligands of CSF1R, also contain decreased density of adult microglia (Li and Barres, 2018).

Aside from *Csf1r*-based models, this study also considered using ones that are based on *CD11b*. Specifically, this study includes data from the CD11b-DTR model in which diphtheria toxin (DT) cell type-specifically ablates microglia and peripheral macrophages. Previous studies have shown that up to 50% microglia could be depleted within 12 hours in this mouse model at P3-4 in the subcortical white matter, followed by microglia repopulation within 36 hours after the last DT injection (Ueno et al., 2013). Disadvantages in this mouse model include side effects from DT as a biological toxin, and non-specific expression of *CD11b* in other tissue-resident macrophages.

Another popular way to deplete microglia is using *Cx3cr1*. However, the main limitation with this marker is that it is also highly expressed in neuroectodermal cells, peripheral immune cells, and bone marrow myeloid precursors (Dumas et al., 2021).

Some more recent models to deplete microglia include using markers such as *Sall1*, *Tmem119*, *P2ry12*, and *HexB* (Dumas et al., 2021). Sall1-CreERT2 and Sall1-GFP mice can distinguish microglia from BAMs and can label embryonic microglia. However, they also contain ectopic expressions in neurons, other glial cells, and kidney mesenchymal cells. Although *Tmem119* is a microglia-specific marker, *Tmem119*-based mouse models do not label embryonic microglia (before E17.5) and have ectopic expression in peripheral tissues such as blood vessels. *P2ry12*-based mouse models are more specific than those based on *Cx3cr1* (no labeling in perivascular and meningeal macrophages), but still contain ectopic expressions in dura mater, choroid plexus, spleen, and liver macrophages. *HexB* is a recently highlighted marker that is relatively specific to microglia, but still labels other tissue-resident macrophages and blood cells (Dumas et al., 2021). More innovative models like a split-Cre system using both Sall1-Cre and Cx3cr1-Cre, which only labels cells double positive in these two markers, seem promising, but remain to be further tested.

In conclusion, despite the myriad of current models used to target and deplete microglia, there still lacks a definitive model that can target all of microglia specifically.

Role of Microglia in Blood Vessel Development

Since microglia appear before vascularization in the brain, and are tightly associated with blood vessels during development, they are hypothesized to play active

roles in angiogenesis. In mice, early postnatal microglia at P7-14 are recruited to blood vessel areas void of astrocytic endfeet and remain highly motile (Mondo et al., 2020). These LYVE1^{+} microglia preferentially contact PDGFRβ[+] SMA[-] capillaries.

In addition to making contact with the blood vessels, microglia have been implicated to regulate vasculature development. In PU.1 and CSF1R mutant mice with microglia and macrophage depletion, the complexity of vasculature is significantly reduced (Fantin et al., 2010). Specifically, microglia and macrophage enable endothelial tip cell anastomosis to form branch points downstream of VEGF in the embryonic mouse hindbrain. In another model with monocyte depletion, vascular complexity remains normal, suggesting the specific role of microglia and macrophages in endothelial branch point formation. Live imaging in the developing zebrafish showed Pu.1[+] macrophages migrate to tip cells to facilitate their fusion (Fantin et al., 2010).

Notwithstanding these results, there are several outstanding unanswered questions as to how microglia may communicate differently among arteries, veins, and capillaries, and the specific microglia subtypes involved in vasculature development.

Prenatal Brain Hemorrhage in the Germinal Matrix

Due to microglia's close association with the developing blood vessels and their active roles in angiogenesis, they are postulated to contribute to the pathogenesis of prematurity-associated brain hemorrhage. In particular, this type of hemorrhage frequently initiates in the germinal matrix in infants born between 23 and 32 GW, due to unclear reasons. It also remains unknown how microglia and other immune cells may contribute to this condition.

The germinal matrix (GM), corresponding to the ganglionic eminences (GE) in the embryonic mouse brain, is a region that produces the majority of inhibitory interneurons and is highly enriched in angiogenesis (Hansen et al., 2013; Ma et al., 2013; Paredes et al., 2022). Past studies have suggested several reasons why this region may be vulnerable to vascular leakage, leading to hemorrhage. To begin with, pericytes, a major vascular support cell type, have lower coverage and density in the GM than in cortical white matter regions (Ballabh, 2014). Notably, GM has a higher expression of S1P and the S1P1 pathway is involved in recruiting pericytes to endothelial cells, where they regulate endothelial cell proliferation, migration, and differentiation. Additionally, angiogenesis in the GM is relatively accelerated via higher expressions of VEGF and ANGPT2, which is coupled with low expression of fibronectin in the basal lamina. This combination leads to less mature blood vessels that are prone to rupture. Mice lacking fibronectin protein show cerebral hemorrhage, confirming the essential role of fibronectin in strengthening vascular barriers (Ballabh, 2010). Lastly, hypoxia has been suggested as a potential reason for hemorrhage in the GM, but has not been explored.

Nonetheless, the mechanism of hemorrhage in the GM and its consequences remain unknown. In particular, the exact cell composition of infiltrating peripheral immune cells remains unexplored. Other blood-related factors have been proposed as mediators of toxic aftereffects of this prenatal brain hemorrhage, including thrombin, hemoglobin, iron, and complement proteins (Ballabh and de Vries, 2021). Thrombin is a blood coagulation enzyme that can increase inflammation, leading to apoptosis in periventricular neurons and ventricular dilation via increased flow of cerebrospinal fluid

from the choroid plexus. Hemoglobin and iron released from lysed red blood cells are cytotoxic, resulting in oxidative damage of neurons and glia. Finally, complements such as C3a can induce neutrophil infiltration and expand infarct size.

Germinal matrix hemorrhage (GMH) and its more severe form, intraventricular hemorrhage (IVH) are huge medical burdens, affecting 12,000 premature infants every year in the United States (Ballabh et al., 2010). In premature infants weighing 500-750 grams, IVH occurs at a staggering rate of 45%. While more than 80% of infants with hemorrhage limited to the GM survive, the rate drastically drops to 50% in those with IVH (Ballabh and de Vries, 2021). Immediate consequences of GMH include cerebral edema, leukocyte infiltration, and calcification in the GM and the periventricular white matter. Long-term consequences include hydrocephalus, cerebral palsy, and epilepsy.

Despite its devastating sequelae, GMH lacks effective preventative and treatment strategies. Currently available therapies in this area include the invasive procedure of endoscopically removing blood clots from cerebral ventricles, by which a third of the treated patients experience re-bleeding (Ballabh and de Vries, 2021). More advanced strategies like stem cell transplant have been shown to decrease apoptosis and inflammation, while promoting angiogenesis and myelination. However, a multitude of adverse effects remain, including potential graft rejection and tumor formation.

Effects of Immune Activation on the Brain

Despite the unexplored roles of immune cells in causing GMH, there have been studies using maternal immune activation (MIA) models to study other effects on the brain. For instance, by injecting lipopolysaccharide (LPS) into the pregnant dam to

mimic bacterial infection, microglia in the prenatal brain show increased phagocytic activities with higher expressions of iNOS and IL-1β, leading to lower numbers of TBR2+ PAX6+ neural progenitor cells (Cunningham et al., 2013).

Past studies have also looked at how systemic peripheral inflammation affects blood brain barrier (BBB) permeability in the adult brain. In LPS-injected mice, an increased number of microglia expressing *Cldn5* migrate to blood vessels via CCR5 (Haruwaka et al., 2019). These mice also showed increased leakage of 10kDa molecules from blood vessels. Intriguingly, microglia seem to apply a two-stage effect on the integrity of BBB. Initially, vasculature-associated microglia maintain the BBB. However, during sustained inflammation, these microglia become phagocytic and consume astrocytic endfeet, impairing BBB function (Haruwaka et al., 2019).

Multi-tasking Microglia in Neural Development

Microglia are essential in maintaining the proliferation of cortical neural progenitor cells (NPCs) and survival of neurons. Microglia selectively colonize cortical proliferative zones in the prenatal brain and preferentially contact proliferating NPCs (Noctor et al., 2001; Anthony et al., 2011; Cunningham et al., 2013; Barger et al., 2018). NPCs isolated from PU.1 knockout mice with microglia ablation show decreased proliferation, which can be rescued by microglia addition (Anthony et al., 2011). This process seems to be mediated by a combination of cytokines derived from microglia, including IL-1β, IL-6, TNFα, and IFNγ (Shigemoto-Mogami et al., 2014). Neurotrophic factors such as IGF-1 secreted by microglia can support layer V neurons in postnatal brain development (Ueno et al., 2013). Specifically, IGF-1 from microglia interacts with IGF1Ra on CTIP2+

SATB2$^+$ layer V neurons to activate the downstream pathway of PI3K-AKT, increasing cell survival and preventing apoptosis.

In addition to their functions in maintaining the NPC population, microglia also facilitate the migration of neurons to the cortex. Using multiple models of microglia depletion and activation, past research has shown that perturbations in microglia activity result in premature entry and abnormal distribution of LHX6$^+$ interneurons in the embryonic cortical plate and a 10% decrease in some interneuron subtypes in the postnatal cortex (Squarzoni et al., 2014).

On the other hand, microglia also phagocytose neural progenitors to control the size of the neuronal pool, and can even promote neuronal death. Cortical NPCs increase in density and proliferation in rats and macaques when microglia are inactivated with broad-spectrum antibiotics or depleted (Cunningham et al., 2013). Using live organotypic slice cultures and *in utero* lentiviral labeling, microglia are shown to engulf and phagocytose proliferating NPCs and radial glia fibers (Cunningham et al., 2013; Barger et al., 2018). In postnatal cerebellar development, microglia promote apoptosis of Purkinje neurons by producing superoxide ions (Marin-Teva et al., 2004).

Due to the multiple roles of microglia in promoting neuronal cell proliferation, survival, migration, and death, it remains a mystery how microglia could orchestrate these myriad functions in a timely manner. How microglia heterogeneity and their communications with separate neuronal types in different regions of the brain remain to be investigated.

Chapter 2: Diverse immune cells and their interactions with the nascent vasculature in the prenatal brain

Introduction

In mice, it is well-established that Runx1$^+$ myeloid precursors travel via blood vessels to colonize the brain parenchyma between E8.5 and 9.5 (Ginhoux et al., 2010). Upon entering the brain, these precursors interact with local environmental cues to undergo further specification (Holtman et al., 2017; Butovsky et al., 2014; Buttgereit et al., 2016). Fate-mapping and transcriptomic analyses reveal a distinct population of CD206$^+$ primitive macrophages that give rise to border-associated macrophages (BAMs), which are located in non-parenchymal niches in the developing brain, including the choroid plexus and meninges (Utz et al., 2020). Additionally, a subset of BAMs is associated with vascular smooth muscle cells and likely become perivascular macrophages in the mature brain (Masuda et al., 2022). In the prenatal mouse hindbrain, macrophage-mediated anastomosis promote vascular network formation (Fantin et al., 2010), whereas in postnatal mouse somatosensory cortex, microglia continue to interact with the established vasculature in areas lacking astrocytic endfeet (Mondo et al., 2020). Similarly in the prenatal human brain, microglia actively colonize different regions during the first and second trimester (Monier et al., 2006; Rezaie et al., 2005). Despite these intriguing findings, how macrophages and microglia impact the formation and maintenance of blood vessels remain unclear.

Here, we show that microglia and macrophages exhibit region-specific and age-dependent association with nascent vasculatures in the ganglionic eminences (GE) of prenatal mouse and human brain. Interestingly, genetic or pharmacological ablation of

microglia and macrophages in mice affects angiogenesis in the ventricular zone (VZ) of

GE, but not in the cortical plate or in the VZ/subventricular zone (SVZ) of pallium. By

leveraging single-cell transcriptomics and high-dimensional flow cytometry, we show

distinct subsets of CD45$^+$ cells employ diverse signaling mechanisms to promote

vascular network formation in the GE. Our results reveal previously unappreciated roles

of the brain's innate immune cells in region-specific angiogenesis.

Results

Microglia-vasculature interactions in the prenatal brain

To characterize the interaction between microglia and blood vessels in the

prenatal human brain, we used light sheet microscopic imaging on optically cleared

coronal sections from the GE and frontal cortex at 20 and 35 gestational weeks (GW)

(**Fig. S2.1a**). Using IBA1 as a generic marker for macrophages, including microglia, and

CD31 for endothelial cells, we showed that blood vessels in the cortical plate were

oriented perpendicular to the pial surface, whereas blood vessels in the VZ/SVZ of the

pallium and GE formed plexus patterns with more branches that were parallel to the

ventricular surfaces (**Fig. 2.1**). Consistent with these observations, vector mapping

using confocal images confirmed the region-specific orientations of blood vessels in the

cortical plate and VZ/SVZ of GE (**Fig. S2.1b**). Notably, blood vessel density in both

regions increased with age and was significantly higher in the GE compared to the

cortical plate at 20-23 GW (**Fig. 2.2e**). In addition, vascular branch point density in the

GE was significantly higher than those in the cortical plate at 14-23 GW and showed

age-dependent decrease as the prenatal brain became more mature (**Fig. 2.2c**).

However, vascular diameter remained similar between the GE and cortical plate, and across developmental stages (**Fig. 2.2d**). Quantification of IBA1$^+$ cell density showed much higher density in the VZ/SVZ of GE than in the cortical plate (**Fig. 2.2a-b, Fig. 2.2f**). In addition, a higher percentage of IBA1$^+$ cells were identified inside the blood vessels in the VZ/SVZ of GE at 14-23 GW, and at 20-23 GW more IBA1$^+$ cells had cell bodies directly touching the blood vessels in the VZ/SVZ of GE than those in the cortical plate (**Fig. 2.2b, Fig. 2.2g-h**). Additional analyses using microglia-specific marker P2RY12 showed near identical results as IBA1, in regard to microglia density and their association with blood vessels in the GE and cortical plate (**Fig. S2.2a-b, Fig. S2.2e-f**). Interestingly, there was a higher density of P2RY12$^+$ cells in the VZ/SVZ of the pallium at GW 14-23, compared to the GE (**Fig. S2.2b**). Nonetheless, a similar percentage of P2RY12$^+$ cells remained attached to the vasculature in the VZ/SVZ of the pallium as in the GE (**Fig. S2.2f**). Another microglia-specific marker TMEM119 did not show any expression in the human prenatal GE at 14 and 22 GW (**Fig. S2.2g**). Finally, CD206$^+$ cells, recently identified as border-associated macrophages (BAM), were not observed in the VZ/SVZ of GE and pallium until 32-39 GW (**Fig. S2.2c-d**).

To elucidate the interactions between IBA1$^+$ cells and blood vessels, we performed immuno-gold electron microscopy (IEM) using IBA1 antibody in tissues from the second trimester human brain at 21 GW. These images captured different stages of IBA1$^+$ cells in the process of extravasation from blood vessels, including traveling near, through or embedded within endothelial cells (**Fig. 2.3a, panels i-viii**), and eventually crossing endothelial cells to reside in perivascular spaces in the GE (**Fig. 2.3a, panel ix**). Within the GE, IBA1$^+$ cells were noted to be adjacent to or surrounding neural

progenitors or neuroblasts (**Fig. 2.3a, panels x-xiii**). In addition, different populations of

IBA1$^+$ cells were identified inside blood vessels in the GE, including those with

morphology of macrophages/monocytes, neutrophils, and eosinophils/basophils (**Fig.

2.3b**). Together, these results suggested a continuous transition of IBA1$^+$ cells from

inside the vascular lumen to perivascular spaces that was more prominently detected in

the VZ/SVZ of GE during the prenatal human brain development.

Microglia/macrophages promote angiogenesis in the mouse GE

Next, we asked whether similar microglia/macrophage-vasculature interactions

could be identified in the embryonic mouse brain. Like the human GE at 20-23 GW,

blood vessel density in E13.5 and E17.5 mouse brain was higher in the GE than in the

cortical plate (**Fig. S2.3a-b**). Although vascular branch point density did not differ

between the two regions at E13.5, E17.5, or postnatal day 0 (P0), the density of IBA1$^+$

cells was higher in the GE than in the cortical plate at E17.5 and P0 (**Fig. S2.3c-d**).

These results suggest a potential species-specific role of IBA1$^+$ cells in vascular branch

point formation in the prenatal human GEs, and not in mice. Furthermore, significantly

more IBA1$^+$ cells were inside the vascular lumen or touching blood vessels with their cell

bodies in the GE at E13.5, than in the cortical plate or at older ages (**Fig. S2.3e-g**).

CD206$^+$ cells and LYVE1$^+$ cells, recently identified as BAM, were not observed in the GE

but were found frequently either in the lateral ventricle or in the meninges at E17.5 (**Fig.

S2.3h**). Thus, microglia/macrophage-vasculature interactions in the embryonic GE differ

significantly from the proposed model currently described in literature, which is based

on the postnatal and adult mouse brain. In particular, mature homeostatic microglia

17

marker TMEM119 has not started its expression in the embryonic GE, and BAM-associated markers CD206 and LYVE1 are also not found in the embryonic GE (**Fig. S2.3i**). Instead, IBA1$^+$ cells in the perivascular milieu retain microglia-specific markers such as P2RY12, indicating that microglia precursors could use blood vessels as a conduit to colonize the brain parenchyma (**Fig. S2.2e-f**).

To further demonstrate that microglia precursors can undergo transendothelial migration from the circulation into the brain, we conducted *in vivo* live imaging in lateral GE (LGE) of E12.5 *Cx3cr1$^{+/GFP}$* mice (**Fig. 2.4a, panel i**) (Cui et al., 2020). To distinguish the location of *Cx3cr1$^{+/GFP}$* cells, which targeted monocytes and macrophages, we visualized blood vessels in LGE via intraplacental injection of Texas Red dextran to fill the vessel lumen. A portion of the developing dorsal cerebral cortex was then removed to obtain an unobstructed partial view of the LGE (**Fig. 2.4a, panel i**). Consistent with its role in immune surveillance, many *Cx3cr1$^{+/GFP}$* cells were highly motile near the perivascular region in the LGE (**Fig. 2.4a, panels ii-iii**), with some extending processes into the vascular lumen to engulf dextran (**Fig. 2.4a, panel iii, cell #1**). Over half of the recorded *Cx3cr1$^{+/GFP}$* cells in the LGE (across 9 embryos) made contact with blood vessels (BV-contacting) (**Fig. 2.4b, panels ii**). Within a 20 minutes time frame, 8 out of 94 *Cx3cr1$^{+/GFP}$* cells were found in the vessel proper and at least one cell crossed the primitive blood-brain barrier in the LGE at E12.5 (**Fig. 2.4a, panel iv**). These results were validated by IEM where IBA1$^+$ cells directly contacted endothelial cells with primitive adherens junction and lacked a definitive basement membrane in medial GE (MGE) at E12.5 (**Fig. 2.4c**).

To study how microglia/macrophage interactions with blood vessels affect angiogenesis, we deleted the mouse *Csf1r* gene, which is essential for the survival of macrophages, including microglia (Li et al., 2006). As expected, homozygous *Csf1r* mutant (*Csf1r$^{-/-}$*) embryos showed a complete loss of IBA1$^+$ cells in the GE, pallium, and cortical plate at E13.5 and E17.5, while IBA1$^+$ cells were partially depleted in heterozygous *Csf1r* mutant (*Csf1r$^{+/-}$*) embryos. Intriguingly, the absence of IBA1$^+$ cells severely reduced vascular density in the VZ of GE in *Csf1r$^{-/-}$* embryos without affecting vascular density in the VZ/SVZ of pallium or in the cortical plate (**Fig. 2.5a-f**). In contrast, *Csf1r$^{+/-}$* embryos showed no changes in vascular density in these regions.

To further determine whether microglia/macrophages have stage-dependent effects on angiogenesis, we intraperitoneally injected wild-type pregnant dams with CSF1R inhibitor PLX5622 (50 mg/kg) for seven consecutive days starting at E6.5, E10.5, or E12.5 to deplete cells from the myeloid lineage. We then collected embryos one day after the last injection at E13.5, E17.5, or P0 (**Fig. S2.4a**). As expected, all three regimens significantly reduced IBA1$^+$ cell density in the GE, pallium, and cortical plate (**Fig. S2.4b-g**). Interestingly, PLX5622 injection from E6.5 to E12.5 did not alter vascular density in the VZ of GE, whereas PLX6522 injections from E10.5 to E16.5 or from E12.5 to E18.5 significantly reduced vascular density in the same region (**Fig. S2.4c**). In contrast, vascular density in the VZ/SVZ of pallium and cortical plate did not alter in PLX5622-injected embryos (**Fig. S2.4d-g**), similar to data from *Csf1r$^{-/-}$* embryos.

In addition to *Csf1r*-based mouse models of microglia and macrophage depletion, another model using CD11b-DTR mice and diphtheria toxin (DT) injections was used to confirm the role of microglia/macrophages in GE angiogenesis. In this

model, IBA1$^+$ cells were only significantly depleted at E17.5 in the GE (**Fig. S2.5a-c**). As a result of microglia depletion, vascular density was reduced at E17.5 in the GE (**Fig. S2.5d**). Further analyses using immunofluorescence staining suggested that VEGFA decreased its expression in IBA1$^+$ cells in PLX5622-injected mice at P0 and DT-injected CD11b-DTR mice at E17.5, suggesting that the VEGF pathway could be involved in microglia/macrophage-assisted angiogenesis in the GE (**Fig. S2.5e-f**). Collectively, the results from *Csf1r$^{-/-}$*, PLX5622-treated, and DT-induced mouse embryos support that microglia and macrophages have region- and stage-specific effects in promoting angiogenesis in the GE.

Age-dependent roles of CD45$^+$ cells in angiogenesis within the prenatal human brain

In light of the results from microglia-depleted mouse embryos, we asked whether microglia and their progenitors could also regulate vascular development in the prenatal human brain during the second trimester. To this end, we used fluorescence-activated cell sorting (FACS) to isolate CD45$^+$ cells from the GE and cortex of the prenatal human brain from 15-23 GW. Sorted cells were then used for bulk and single-cell RNA sequencing (scRNA-seq), high-dimensional flow cytometry, and *in vitro* co-culture with human umbilical vein endothelial cells (HUVEC) in 3D Matrigel (**Fig. 2.6a**). For bulk RNA-seq, we collected CD45$^+$ cells from 16 samples from the cortical plate and 4 from the GE, and CD45$^-$ cells from 3 samples (as negative controls). Our results showed that CD45$^+$ cells were highly enriched in canonical microglia genes, including *AIF1* (encoding IBA1), *TMEM119, SPI1, CX3CR1, CSF1R* and *IRF8* (**Fig. S2.6a-b**). In addition, these cells expressed markers in previously identified subtypes of microglia or

macrophages, including *SPP1* (in proliferative-region-associated microglia, PAM), *LYVE1* (in BAM), *TREM2* and *APOE* (both in disease-associated microglia, DAM) (Utz et al., 2020; Li et al., 2019; Keren-Shaul et al., 2017). In contrast, CD45$^-$ cells were enriched in genes related to proliferation (*CDK4, PCNA*) and neural progenitors (*OLIG2, SOX2, HOPX*), indicating a radial glia-like population (**Fig. S2.6a-b**). Gene Ontology (GO) terms from Gene Set Enrichment Analysis (GSEA) confirmed that CD45$^-$ cells consisted of radial glia, immature neurons, and oligodendrocytes, whereas CD45$^+$ cells were immune cells including microglia and macrophages (**Fig. S2.6c**). Interestingly, CD45$^+$ cells were also enriched in genes related to cell adhesion (*ITGB2*, *ITGAL, ITGAM, ADAM8*) and chemotaxis (*CCRL2, CCL5*), as well as endothelial cell-specific genes (*PLVAP, GATA2*), suggesting their close association with the blood vessels (**Fig. S2.6c**). Comparisons between our bulk RNA-seq dataset in CD45$^+$ cells with published transcriptomic datasets in embryonic and early postnatal microglia from mouse and human highlighted core microglia genes such as *P2ry12, Aif1, SPI1*, and *Tmem119* (**Fig. S2.6d-e**). Particularly, in human fetal and early postnatal microglia, overlapped genes with our bulk RNA-seq dataset in CD45$^+$ cells were related to microglia activation and transendothelial migration (**Fig. S2.6e**). High dimensional *in situ* hybridization validated markers in CD45$^+$ cells that were related to microglia subsets, transendothelial migration, proliferation (**Fig. 2.6f**).

Next, we asked whether CD45$^+$ cells from the prenatal human brain also exhibited age-dependent changes in gene expression related to angiogenesis. In support of this idea, differentially expressed genes (DEGs) and GO terms identified by GSEA in 14-19 GW CD45$^+$ cells showed higher expression of genes related to aerobic

respiration (*DLD, NDUFB6, MDH1*), whereas 20-23 GW CD45$^+$ cells showed enrichment of genes involved in blood vessel development (*SOX18, CCN1, CCN2, APLNR, FN1, TMEM204*) (**Fig. 2.6b-c**). Additional analyses focusing on genes that increase or decrease their expressions in correlation with age showed dynamic regulation of gene transcription, lipid metabolism, cellular growth (**Fig. 2.6d-e**).

To test whether CD45$^+$ cells could promote vascular development, we co-cultured CD45$^+$ cells with HUVEC in Matrigel-coated wells and used live-imaging to determine how CD45$^+$ cells affected branch formation in HUVEC. To visualize how CD45$^+$ cells interacted with endothelial cells, we transfected CD45$^+$ cells with AAV-CMV-GFP and showed that many GFP$^+$ CD45$^+$ cells were in direct contact with HUVEC (**Fig. S2.7a**). In the absence of CD45$^+$ cells, HUVEC showed modest branch morphogenesis at 20,000 cells/well. Interestingly, adding 10,000 or 20,000 CD45$^+$ cells from 20-23 GW prenatal human brain to 20,000 HUVEC promoted endothelial branch growth, increasing both average and total branch length (**Fig. 2.7a-b, Fig. S2.7d-e**). Notably, branch length remained higher in wells supplied with 20-23 GW CD45$^+$ cells even after 48 hours in culture, suggesting a role for these cells in stabilizing vascular branches. In contrast, the same number of CD45$^+$ cells from 14-19 GW human brain samples or CD45$^-$ cells from the same age range did not enhance branch morphogenesis in HUVEC (**Fig. 2.7a-b, Fig. S2.7d-f**). Additional analyses showed that AAV transfection did not affect the ability of CD45$^+$ cells in promoting vascular morphogenesis *in vitro* (**Fig. S2.7b-c**).

scRNA-seq reveals GE-enriched CD45⁺ cell subtypes

To investigate which CD45$^+$ subtypes are enriched in the GE, we performed scRNA-seq on FACS-isolated CD45$^+$ cells from microdissected GE and cortical plate from 15-23 GW. After excluding low quality cells and doublets, we obtained 60,595 cells with 1,654 genes per cell (**Fig. S2.8a-b**). Clustering identified 9 subtypes, including 3 subtypes of homeostatic microglia (c1a, c1b, c1c), white-matter-associated microglia (c2), cell cycle microglia (c3), vasculature-associated microglia (c4), monocytes (c5), HLA$^+$ myeloid cells (c6), neuron-associated microglia (c7), T cells (c8) and B cells (c9) (**Fig. 2.8a-b**). The homeostatic microglia clusters were enriched in canonical microglia genes such as *AIF1* and *CX3CR1* (**Fig. 2.8b, Fig. S2.9a**). White-matter associated microglia (c2) were transcriptomically similar to the previously defined proliferative region-associated microglia (PAM) (*SPP1, GPNMB, CLEC7A*) (Li et al., 2019; Hammond et al., 2019) and disease-associated microglia (DAM) (*TREM2*) (Keren-Shaul et al., 2017), and were abundant near developing white matter tracts in the internal capsule (**Fig. S2.9b**). Cell cycle microglia (c3) were enriched in proliferation genes (*MKI67, TOP2A, AURKA*), whereas T and B cells showed high-level expressions of *IL7R* and *MS4A1,* respectively. Neuron-associated microglia (c7) were enriched in neuronal genes (*STMN2, NRXN1, DCX, CAMK2N1*), which likely represent microglia that have phagocytosed neurons (Li et al., 2019; Hammond et al., 2019). Vasculature-associated microglia (VAM, c4) expressed endothelial genes (*CLDN5, MFSD2A, SLC2A1, ITM2A, IGFBP7)*, suggesting that these microglia may have phagocytosed parts of the endothelial cells as they migrated across and interacted with the primitive BBB. Finally, our scRNA-seq data also identified monocytes (c5) that

expressed *LYZ*, *JAML* and *S100A9*, and HLA^{+} myeloid cells (c6) that expressed *CD74*, *HLA-DP* and *HLA-DR* (**Fig. 2.8b, Fig. S2.9a**).

To further characterize CD45^{+} immune cells from the prenatal human brain, we projected published datasets on embryonic microglia onto our scRNA-seq UMAP. CD45^{int} CD11b^{+} DRAQ5^{+} cells from 9-18 GW human brain (Kracht et al., 2020) transcriptomically match all our clusters except for T cells and VAM. In addition, CD45^{lo} CD11b^{+} CX3CR1^{hi} CD64^{+} cells from 10-12 GW brainstem and cortex (Han et al., 2023) mostly overlap with homeostatic microglia and HLA^{+} myeloid cells. Finally, CD45^{+} CD11b^{+} Cx3cr1^{+} cells from E14.5 mouse brain (Hammond et al., 2019) overlap with all our subtypes, except for T cells and B cells (**Fig. S2.8d**). To identify CD45^{+} cell subtypes that showed regional preferences, we compared the relative abundance of subtypes in the GE or cortex. This comparison showed that c1a homeostatic microglia and c6 HLA^{+} myeloid cells were preferentially located in the GE, whereas c1b and c1c homeostatic microglia were preferentially located in the cortex (**Fig. 2.8c, Fig. S2.8c**). Other subtypes showed no regional preference. Interestingly, DEGs and GSEA in CD45^{+} cells from the cortex showed enrichment for GO terms including chemotaxis (*CH25H*, *CX3CR1, CCL3*), regulation of cell death (*CEBPB*, *TLR4, TNF*), and neuron projection guidance (GO 0097485), whereas CD45^{+} cells from the GE were enriched for GO terms including antigen processing and presentation (*HLA-DRA, HLA-DPA1, HLA-DRB1*; GO 0019884), plasma lipoprotein assembly (*APOC1, APOC2, ABCA1*), and sister chromatid segregation (GO 0000819) (**Fig. 2.8d-e**).

To validate these scRNA-seq data, we performed immunofluorescence microscopy by combining antibodies and *in situ* hybridization probes for specific

subtypes of immune cells. These results showed more abundant HLA$^+$ myeloid cells and *CLDN5$^+$ SLC2A1$^+$ IGFBP7$^+$ MFSD2A$^+$* IBA1$^+$ VAM inside the blood vessels in the GE than in the cortex (**Fig. 2.9b-c, Fig. 2.9g**), whereas the number of *JAML$^+$ LYZ$^+$* S100A9$^+$ or CD16$^+$ monocytes showed no regional differences (**Fig. 2.9d-g**). Additional sub-clustering analyses in VAM (c4), monocytes (c5), and HLA$^+$ myeloid cells (c6) indicated region-dependent transcriptomic signatures (**Fig. S2.12a-c**). Collectively, these results provide the first comprehensive analysis of CD45$^+$ immune cell subtypes and their interactions with blood vessels in the prenatal human brain. Drawing inferences from our IBA1 IEM data and live imaging data (**Fig. 2.3-4**), this scRNA-seq dataset most likely captures CD45$^+$ immune cells transitioning from their intravascular states to transendothelial migration, and finally becoming homeostatic microglia.

Flow cytometry validates immune cell subtypes in the prenatal human brain

To validate the clusters identified in scRNA-seq, we performed high dimensional flow cytometry by applying 13 cell surface markers on CD45$^+$ cells from the second trimester prenatal human brain. After gating for CD45$^+$ immune cells, which constituted ~1.5% of all single live cells, we identified 9 immune cell subtypes, which included two subgroups of microglia. The first group, microglia #1, was defined by CX3CR1^{hi} CD14^{lo} expression as previously described in human and mice (Friebel et al., 2020; Mrdjen et al., 2018) and the second group, microglia #2, was defined by CD64^{hi} CD14^{lo} that included BAM (Utz et al., 2020; Masuda et al., 2022) (**Fig. 2.10a-b**). After gating out microglia, we identified classical monocytes (cMono; CD64^{lo} CD14^{hi}), non-classical monocytes (ncMono; CD64$^-$ CD14$^-$ CD16$^+$), dendritic cells (CD64$^-$ CD14$^-$ CD16$^-$

HLA-DR$^+$ CD11c$^+$), T cells, B cells, eosinophils, and neutrophils (**Fig. 2.10a-b**). Like in

the adult mouse brain (Mrdjen et al., 2018), several cell surface proteins identified in

microglia and BAM, including CD64 (encoded by *FCGR1A*) and CD206 (encoded by

MRC1), were expressed in homeostatic microglia clusters 1a, 1b and 1c in our

scRNA-seq dataset (**Fig. 2.10c-e**). Based on flow cytometry data, microglia #1 and

microglia #2 each represented ~40% of the entire CD45$^+$ immune cell population in the

prenatal human brain, whereas T cells and B cells represented ~1-2%, with monocytes

and dendritic cells (DCs) represented less than 1% (**Fig. 2.10f**). To reconcile the VAM

cluster (c4) from our scRNA-seq with results from high dimensional cytometry, we

showed that 5-15% of CD45$^+$ cells co-expressed CD31, a canonical endothelial cell

marker (**Fig. 2.10g**). Among CD45$^+$ CD31$^+$ cells, ~50% belonged microglia #2 and only

~10% were classical monocytes or microglia #1 (**Fig. 2.10h**). Finally, we showed that,

among all immune cell types, classical monocytes expressed the highest levels of

HLA-DR. Microglia #2, which included BAM, expressed modest levels of HLA-DR (**Fig.

2.10i**). Thus, the majority of HLA$^+$ myeloid cells identified in our scRNA-seq dataset

most likely consisted of classical monocytes and a smaller population of BAM.

       To understand how immune cells regulate angiogenesis, we used CellPhoneDB

to predict cell-cell communication via ligand-receptor pairs between CD45$^+$ cells and

endothelial cells from the prenatal human brain at the same gestational ages (Crouch et

al., 2022; Efremova et al., 2020). This approach showed that at 14-19 GW, all

endothelial cell subtypes, including tip cells, mitotic, venous, arterial, and capillary

endothelial cells, had extensive cell-cell communications with one another. However,

only VAM (c5) among CD45$^+$ cells exhibited cell-cell communication with endothelial

cells (**Fig. S2.10a**). By 20-23 GW, most CD45^{+} subtypes showed cell-cell

communication with endothelial cells, consistent with the stage-dependent role of CD45^{+}

cell to promote endothelial branch formation in Matrigel assays (**Fig. 2.7**). Next, we

used NicheNet to predict ligand-target gene links between these two cell types

(Browaeys et al., 2020), focusing on HLA^{+} myeloid cells, monocytes, VAM, and

homeostatic microglia (c1a) in the GE. Our results showed that at 14-19 GW, both HLA[+]

myeloid cells and monocytes showed robust interactions with all endothelial cell

subtypes (**Fig. S2.10b**). By 20-23 GW, monocytes exhibited the most robust signaling

pathways in interacting with endothelial cells in the GE. The most prominent

ligand-target gene link was ITGB2 (CD18) from monocytes and ICAM2 receptor from

endothelial cells (Gerhardt and Ley, 2015). Immunofluorescence staining confirmed that

CD18^{+} cells were preferentially found within the vascular lumen in embryonic human

and mouse GE (**Fig. S2.10c-e**). Additional ligands employed by HLA^{+} myeloid cells and

monocytes to interact with endothelial cells at 14-19 GW included VEGFB, IGF1,

TGFB1, TNF, CXCL16, and IL1B. Among the identified ligands from CD45^{+} cells, both

VEGF (25 ng/ml) and IGF1 (5 ng/ml) increased branch lengths of HUVEC in Matrigel

assay (**Fig. S2.11a-b**), consistent with previous studies (Smith et al., 1999).

Discussion

Previous work has shown that macrophages promote cerebrovascular formation

through endothelial tip cell fusion (Fantin et al., 2010). In the postnatal mouse brain,

microglia continue to interact with the vasculature and regulate blood flow (Mondo et al.,

2020; Bisht et al., 2021). However, there is a fundamental gap as to whether

macrophages, microglia or other immune cells have region- and stage-dependent

differences in angiogenesis during brain development. Our results uncover several key mechanisms governing how the brain's immune cells regulate angiogenesis in the prenatal brain. First, in the prenatal mouse and human brain, nascent vasculatures in the GE exhibit complex branching morphogenesis and are associated with more IBA1^{+} microglia and macrophages (**Fig. 2.1-2**, **Fig. S2.1-3**). Interestingly, ablation of IBA1^{+} cells in the embryonic mouse brain shows that these immune cells have region-specific and age-dependent role in promoting the formation of a complex vascular network in the GE, but not in the cortical plate or in the VZ/SVZ of pallium (**Fig. 2.5**, **Fig. S2.4-5**). Consistent with these results, CD45^{+} cells from 20-23 GW human brains exhibit transcriptomic features that are pro-angiogenic and are more effective in promoting vascular morphogenesis in HUVEC than those from 14-19 GW (**Fig. 2.6-7, Fig. S2.7**).

Using scRNA-seq and high-dimensional flow cytometry analysis of CD45^{+} cells from 15-23 GW human brain, we further characterize specific CD45^{+} cell subtypes, including HLA^{+} myeloid cells, monocytes, and VAM, and show that these cells utilize diverse signaling pathways including IGF1 and VEGF to promote angiogenesis (**Figs. 2.8-10, Fig. S2.10-11**). Compared with previously published datasets from prenatal human and mouse brain (Keren-Shaul et al., 2017; Hammond et al., 2019; Han et al., 2023), our results not only capture the developmental trajectory of CD45^{+} cells transitioning from intravascular space to parenchymal microglia, but also provide critical insights into the molecular mechanisms employed by subsets of CD45^{+} cells to promote angiogenesis in the GE. These datasets provide important resources for future studies to investigate how these immune cells might impact other critical aspects of brain development, including myelination, neuronal migration, and differentiation.

Figures
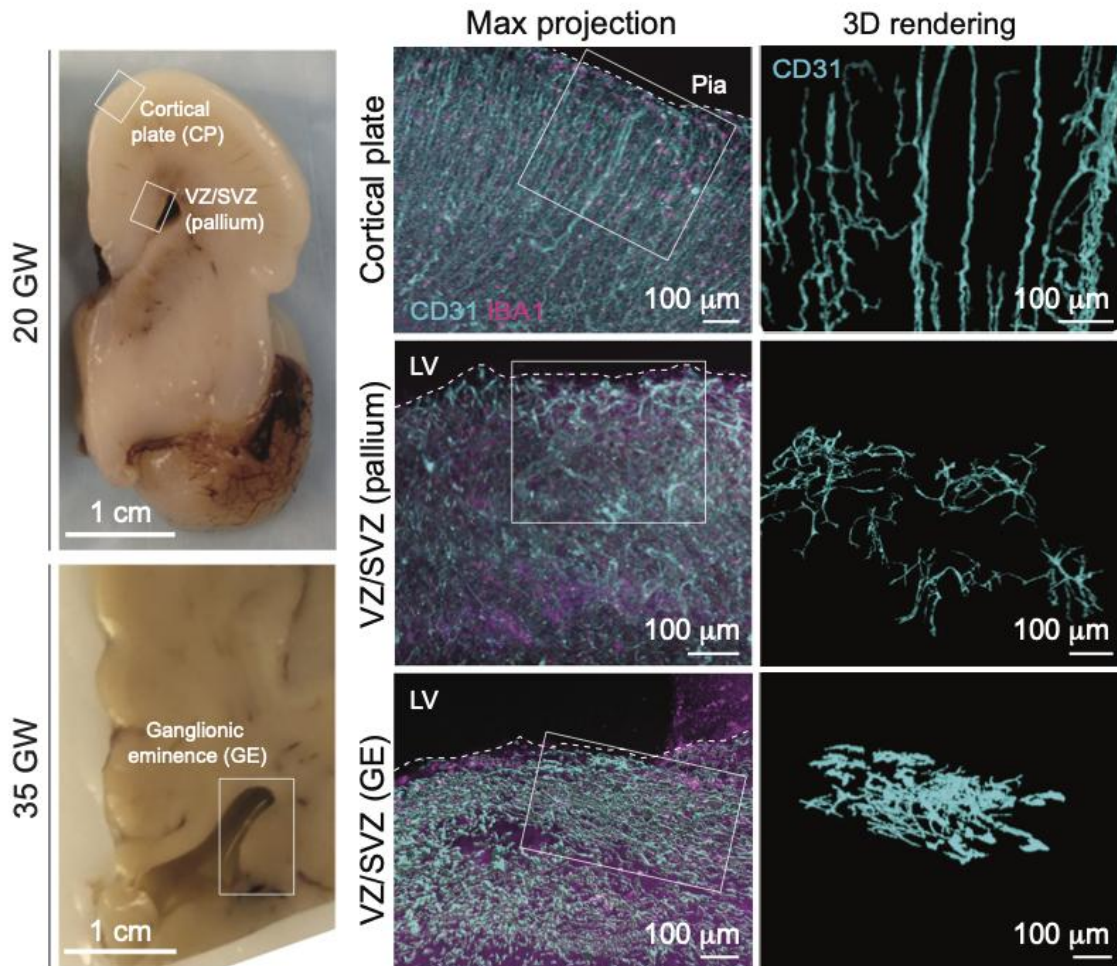
Figure 2.1: Vascular patterns vary across regions of the prenatal human brain.
Coronal sections of prenatal human brain at 20 and 35 GW, highlighting the ganglionic eminences (GEs), ventricular zone/subventricular zone (VZ/SVZ) of the pallium, and cortical plate (CP) (left column). Light sheet images in optically cleared coronal sections show intricate interactions between IBA1^{+} cells and CD31^{+} endothelial cells in CP, VZ/SVZ of pallium, and GE (middle column). IMARIS 3D images reveal the morphology of CD31^{+} endothelial cells in each brain region (right column).
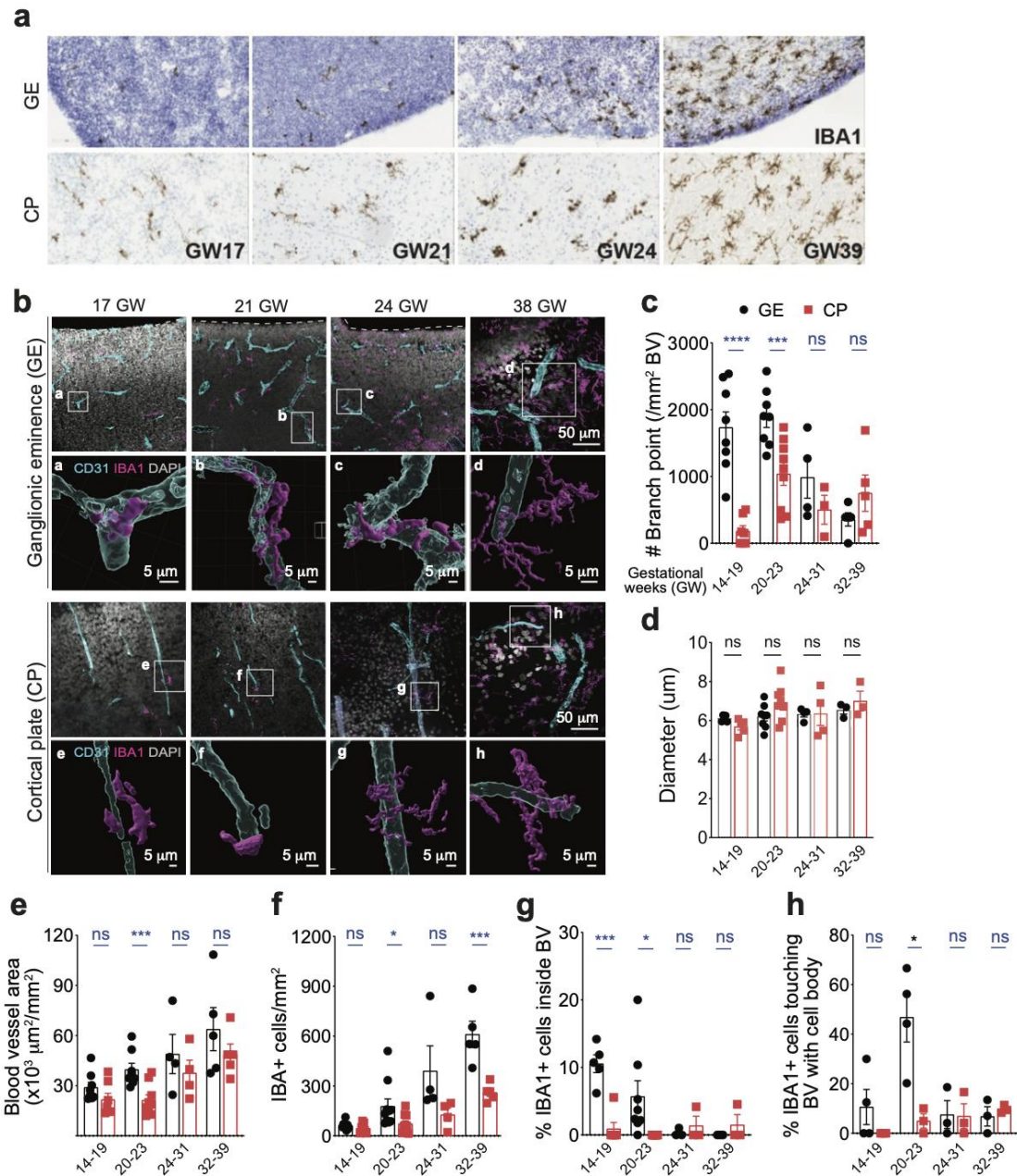
Figure 2.2: IBA1+ cells dynamically interact with the nascent vasculature.
(**a**) DAB staining of IBA1 in GE and CP at 17, 21, 24 and 39 gestational weeks (GW) .
(**b**) Confocal images and IMARIS 3D rendering of IBA1+ cells interacting with CD31+ endothelial cells in the GE and CP at 17, 21, 24 and 38 GW.
(**c-e**) Quantifications of vascular branch point, diameter, and density in GE and CP of the prenatal human brain.
(**f-h**) Quantifications of the density of IBA1+ cells, the percentage of IBA1+ cells inside blood vessels, and the percentage of IBA1+ cells touching blood vessels with the cell body in GE and CP of the prenatal human brain.
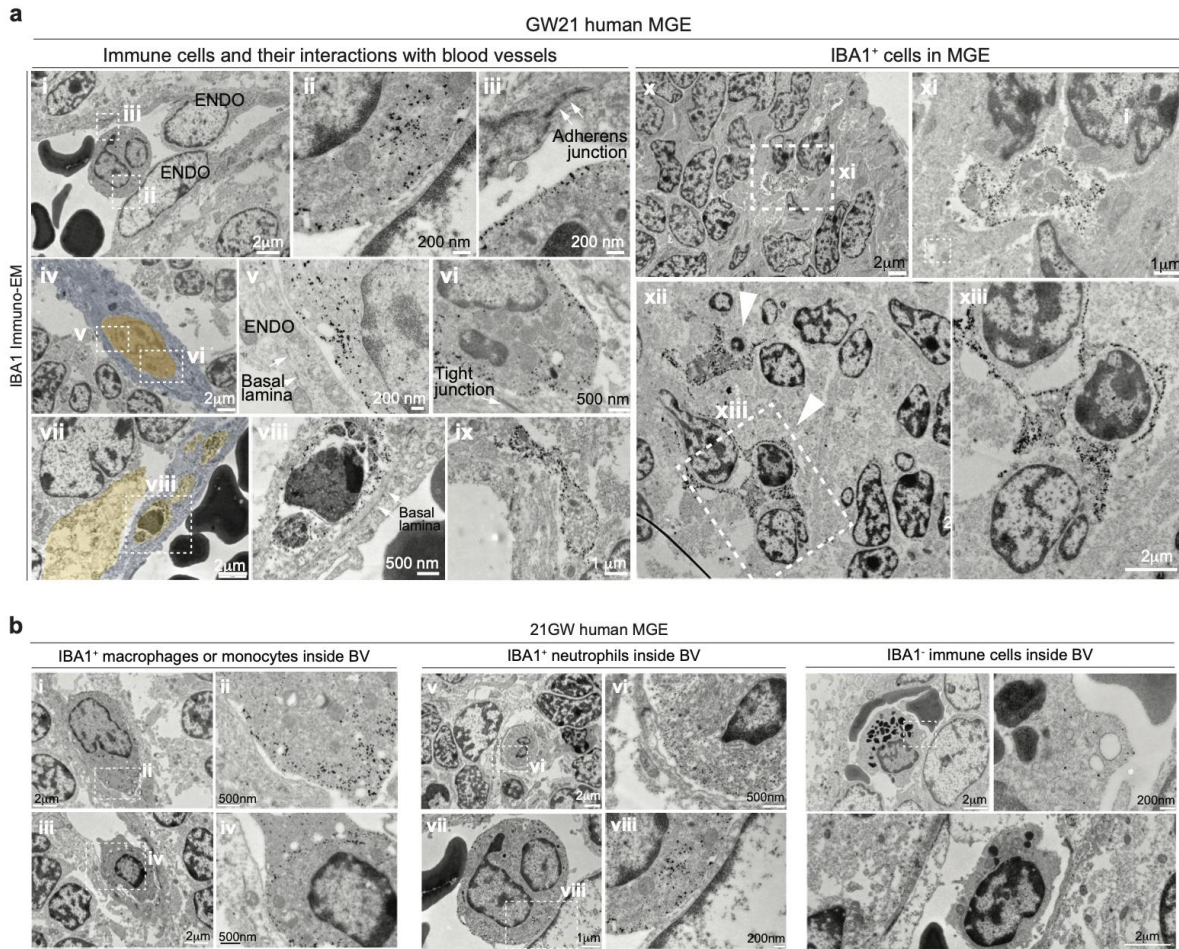
Figure 2.3: Ultrastructures of IBA1$^+$ cells in the perivascular milieu of human GE.
(**a**) Immuno-gold electron microscopy (Immuno-EM) using IBA1 antibody shows macrophages and microglia inside blood vessels with primitive basal lamina and in the perivascular milieu in the human medial ganglionic eminence (MGE) at 21 GW.
(**b**) Additional immuno-EM images using IBA1 antibody show immune cells inside the blood vessels (BV) of human MGE at 21 GW.
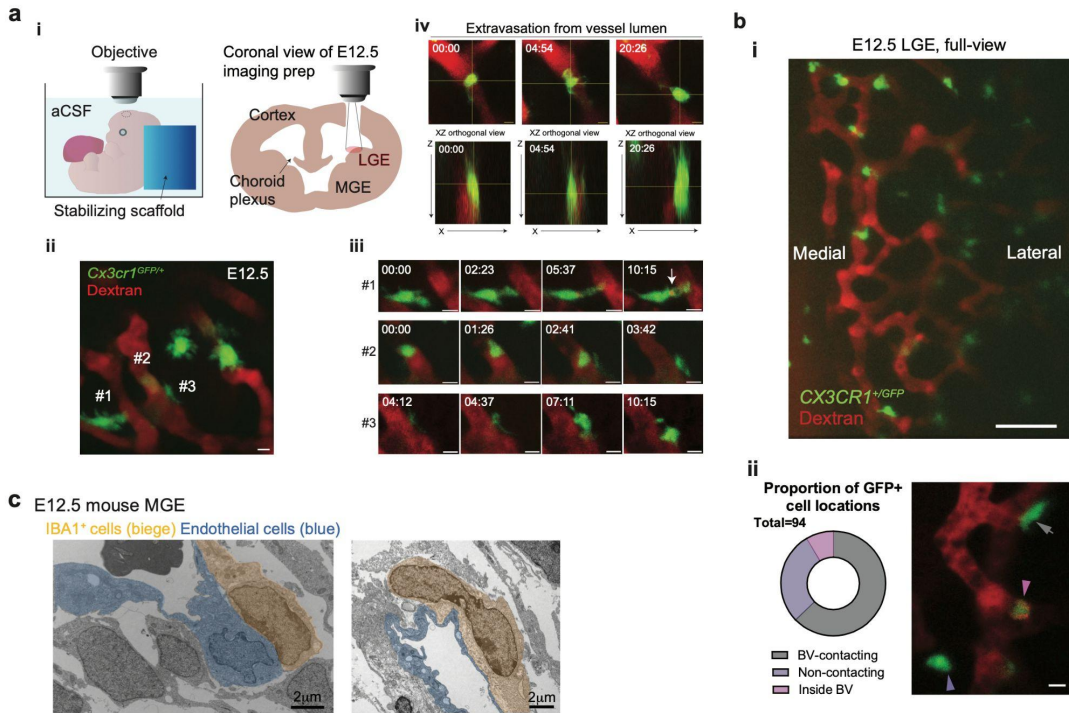
Figure 2.4: Dynamic and close interactions between microglia/macrophages and blood vessels in the embryonic mouse GE.

(**a**) Live imaging of the migration and interaction of *Cx3cr1*[GFP/+] microglia/macrophages with nascent vasculature in the GE. (**i**) Schematic diagrams of imaging set-up for E12.5 lateral ganglionic eminence (LGE) in *Cx3cr1*[GFP/+] mice. Embryo remains attached to placenta while bathed in artificial CSF (aCSF). Coronal cross-section illustrates LGE exposure and live imaging location. (**ii**) Max projection of an *in vivo* two-photon image with three *Cx3cr1*[GFP/+] cells in the LGE associated with blood vessels illuminated with Texas Red dextran. Scale bar, 10 µm. (**iii**) Still-frames of time-lapse images of each of the three *Cx3cr1*[GFP/+] cells, with #1 extending process into the blood vessel and taking up dextran, #2 rolling within the blood vessel before releasing into the circulation, and #3 moving along the surface of a blood vessel. Scale bar, 10 µm. (**iv**) Extravasation of a *Cx3cr1*[GFP/+] cell between the lumen and abluminal side. Orthogonal views show the *Cx3cr1*[GFP/+] cell against one vessel wall on the luminal side at time 0 and against the vessel wall on the abluminal side at 20:26 min. Scale bar, 10 µm.
(**b**) (**i**) Still image highlighting the full view of LGE in an E12.5 embryo undergoing *in vivo* live imaging. (**ii**) A representative image showing three different behaviors of *Cx3cr1*[+/GFP] cells and quantification of these three different cell behaviors from a total of 97 cells from 9 mouse embryos captured in live imaging.
(**c**) Immuno-EM using IBA1 antibody shows IBA1^{+} cells directly attached to the endothelial cells in the MGE of E12.5 mouse brain.
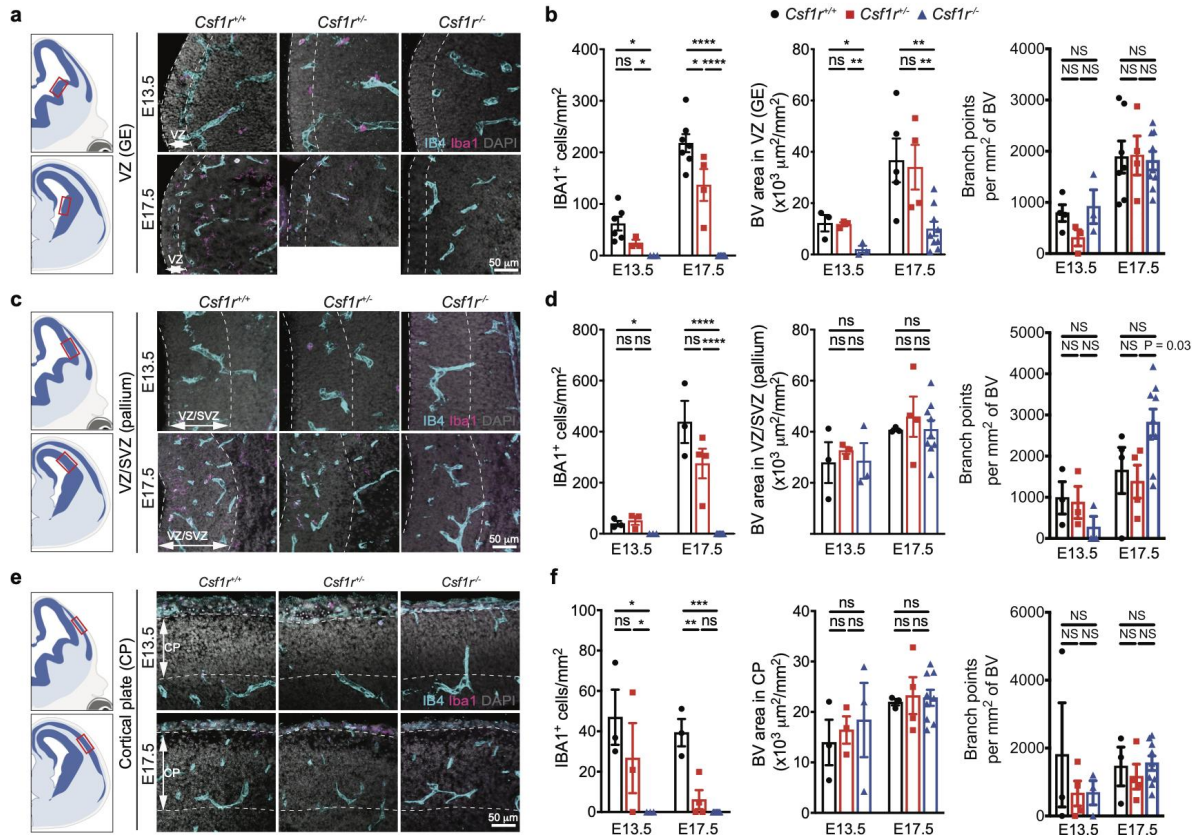
Figure 2.5: Microglia and macrophages are required for angiogenesis in the ventricular zone (VZ) of GE.

(**a**, **c**, **e**) Loss of CSF1R leads to ablation of IBA1$^+$ cells in (**a**) GE, (**c**) VZ/SVZ of pallium, and (**e**) CP. Red boxes in schematic diagrams indicate the regions captured in confocal images.

(**b**, **d**, **f**) Quantification of densities of IBA$^+$ cells, IB4$^+$ blood vessels, and vascular branch points in (**b**) VZ of GE, (**d**) VZ/SVZ of pallium, and (**f**) CP. Dashed lines indicate the regions in which blood vessel quantifications are performed.
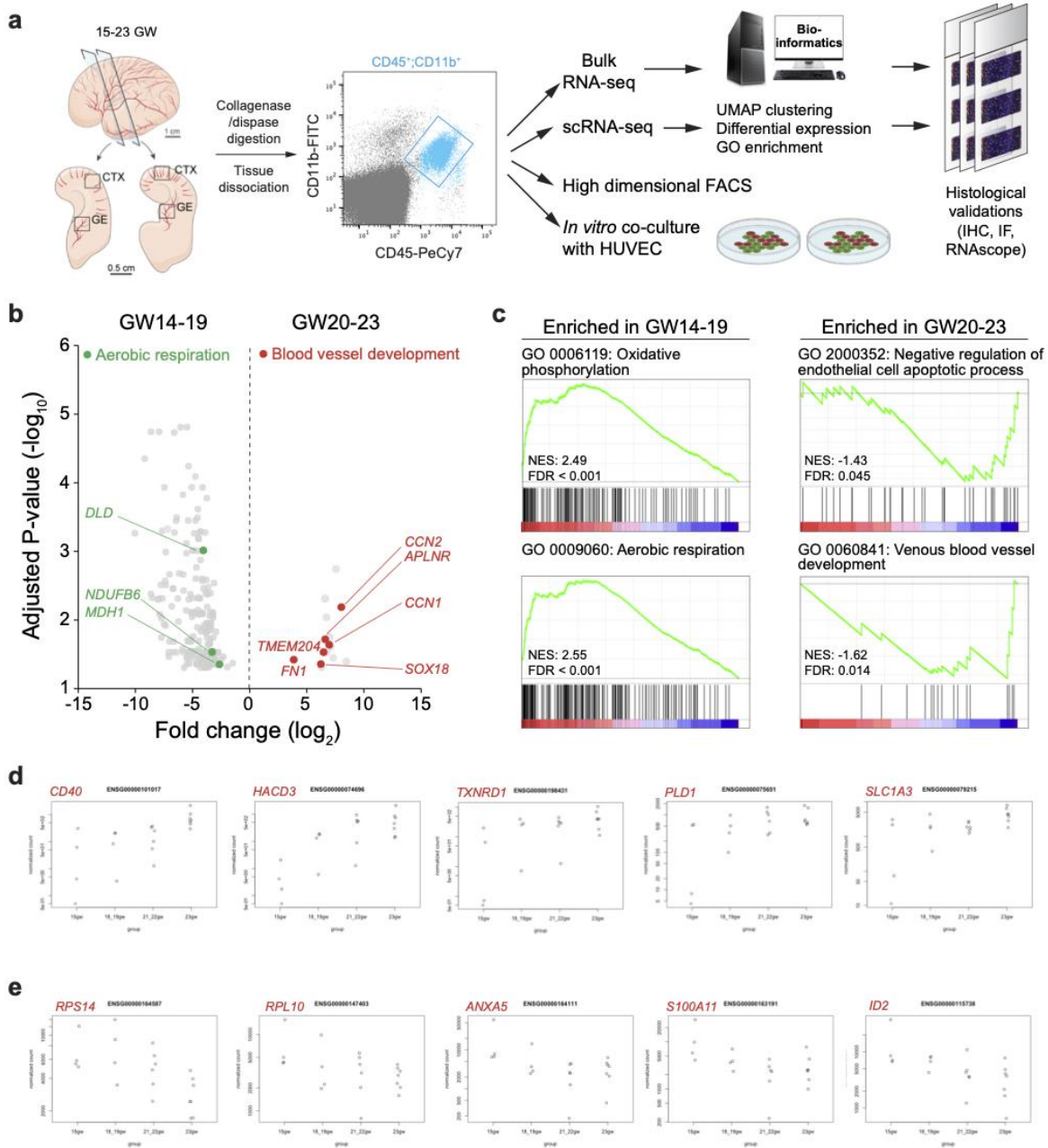
Figure 2.6: Stage-dependent enrichment of genes related to blood vessel development in CD45+ cells.
(**a**) Schematic diagrams showing the strategy to isolate CD45+ CD11b+ immune cells from the cortex (CTX) and GE of the prenatal human brain from 15-23 GW. These CD45+ CD11b+ cells are subjected to bulk RNA-seq and scRNA-seq, followed by bioinformatics analyses.
(Figure caption continued on the next page.)

34

(Figure caption continued from the previous page.)
The transcriptomic data are validated using immunohistochemistry (IHC), immunofluorescence microscopy (IF), and RNAscope-based *in situ* hybridization. Finally, CD45^{+} CD11b^{+} cells are further characterized using high dimensional flow cytometry and in 3D Matrigel HUVEC assays.
(**b**) Volcano plot shows the genes enriched in CD45^{+} cells from 20-23 GW (right) and those enriched in cells from 14-19 GW (left).
(**c**) GSEA reveals GO terms enriched in CD45^{+} cells from 14-19 GW and 20-23 GW. Data in (**b**) and (**c**) are from 21 independent biological samples.
(**d, e**) Genes that (**d**) increase or (**e**) decrease their expressions with age in this bulk RNA-seq dataset.
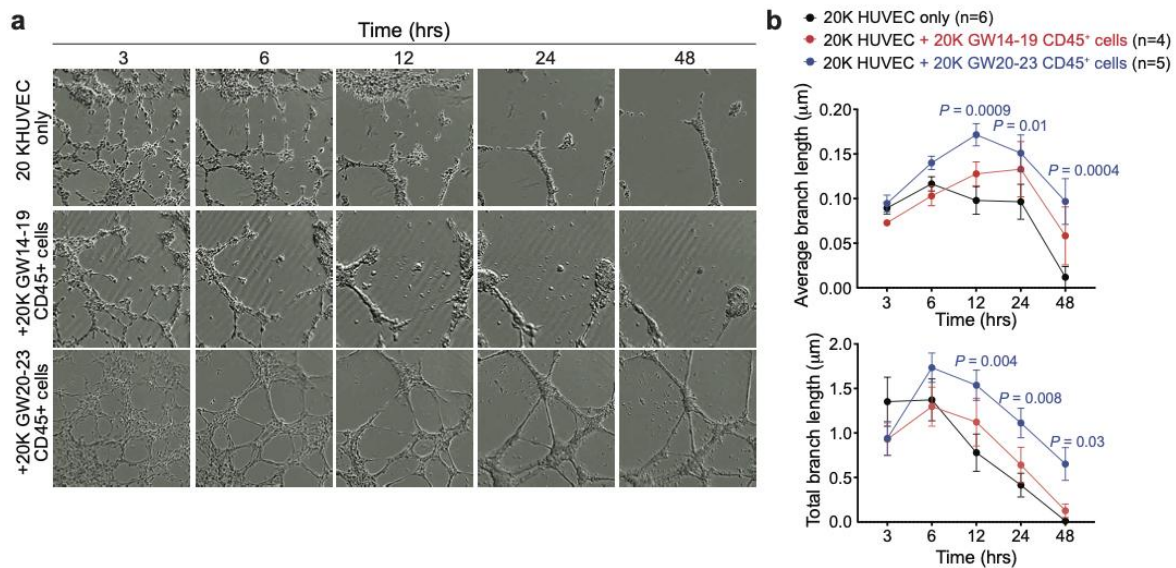
Figure 2.7: Stage-dependent role of CD45^{+} cells in promoting vascular morphogenesis.
(**a**) Images taken from InCucyte S3 Live Imaging Device of HUVEC in Matrigel-based branching morphogenesis at 3, 6, 12, 24 and 48 hours (hrs) after plating. The conditions include 20,000 HUVEC alone, and 20,000 HUVEC co-cultured with 20,000 14-19 GW or 20-23 GW CD45^{+} cells from the prenatal human brain.
(**b**) Quantification of average and total endothelial branch lengths formed by HUVEC. The P values represent comparisons between HUVECs co-incubated with CD45^{+} cells *vs* HUVECs only. Not significant comparisons are not shown. *n* indicates the number of independent biological samples used for quantification. For each biological sample, at least 3 technical replicates are used.
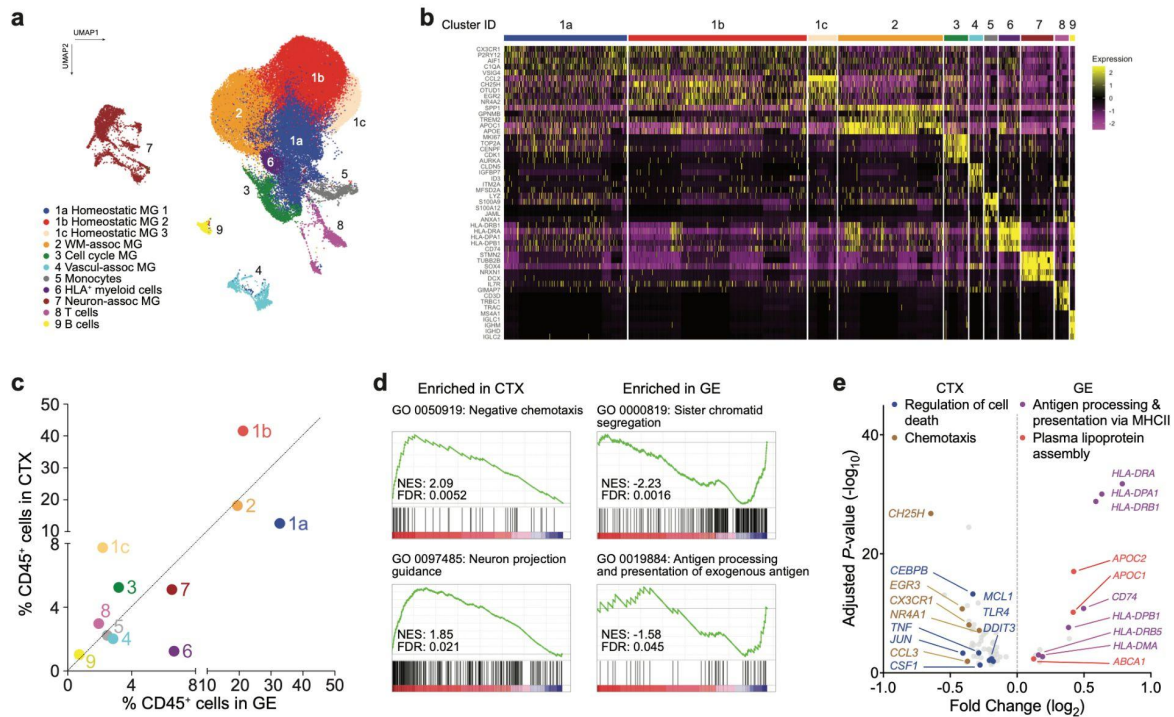
Figure 2.8: Single-cell transcriptomics reveal subtypes of CD45+ cells and their interactions with endothelial cells in the prenatal human brain.
(**a**) UMAP plot highlighting 9 distinct CD45+ cell subtypes.
(**b**) Heatmap of marker gene expressions that define each subtype of CD45+ cells.
(**c**) A distribution plot comparing the relative abundance of each CD45+ subtype in GE *vs* CTX.
(**d**) GSEA analysis of the bulk RNA-seq data reveal GO terms defined by genes enriched in GE *vs* CTX.
(**e**) Volcano plot shows differentially expressed genes (DEGs) identified by pseudo-bulked scRNA-seq data in GE *vs* CTX and the GO terms they define. Data in panels (**a**), (**b**), (**c**), and (**e**) are from 5 independent biological samples at 15-23 GW. Data in (**d**) are from 21 independent biological samples at 15-23 GW.
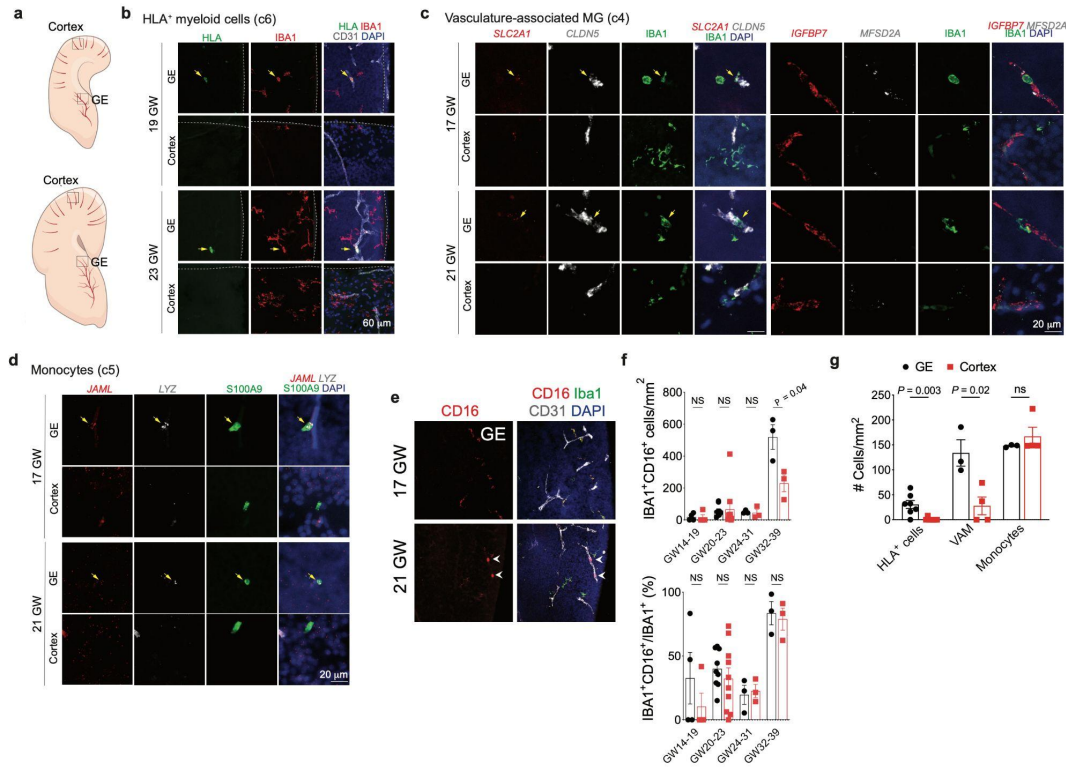
Figure 2.9: Validation of CD45+ cell subtypes from scRNA-seq.
(**a**) Schematic diagram showing the regions of GE and cortex in 14-19 GW (top) and 20-23 GW brains (bottom).
(**b**) Confocal images from GE and cortex of 19 and 23 GW human brain validating the presence of HLA+ cells in the GE (yellow arrowheads) but not in the cortex.
(**c**) Confocal images of vasculature-associated microglia (VAM) markers *SLC2A1, CLDN5, IGFBP7,* and *MFSD2A* (RNAscope probes) in IBA1+ cells in the GE (yellow arrowheads) but not in the cortex of 17 and 21 GW human brains.
(**d**) Confocal images of monocyte markers *JAML* and *LYZ* (RNAscope probes) in S100A9+ cells in the GE (yellow arrowheads) but not in the cortex of 17 and 21 GW human brains.
(**e**) Confocal images of monocyte marker CD16 in IBA1+ cells in the GE (white arrowheads) of 17 and 21 GW human brains.
(**f**) Quantification of the density of IBA1+ CD16+ cells, and the percentage of IBA1+ CD16+ cells in IBA1+ cells in the GE and cortex of the prenatal human brain.
(**g**) Quantification of the density of HLA+ cells, VAM, and monocytes in the GE and cortex of the prenatal human brain.
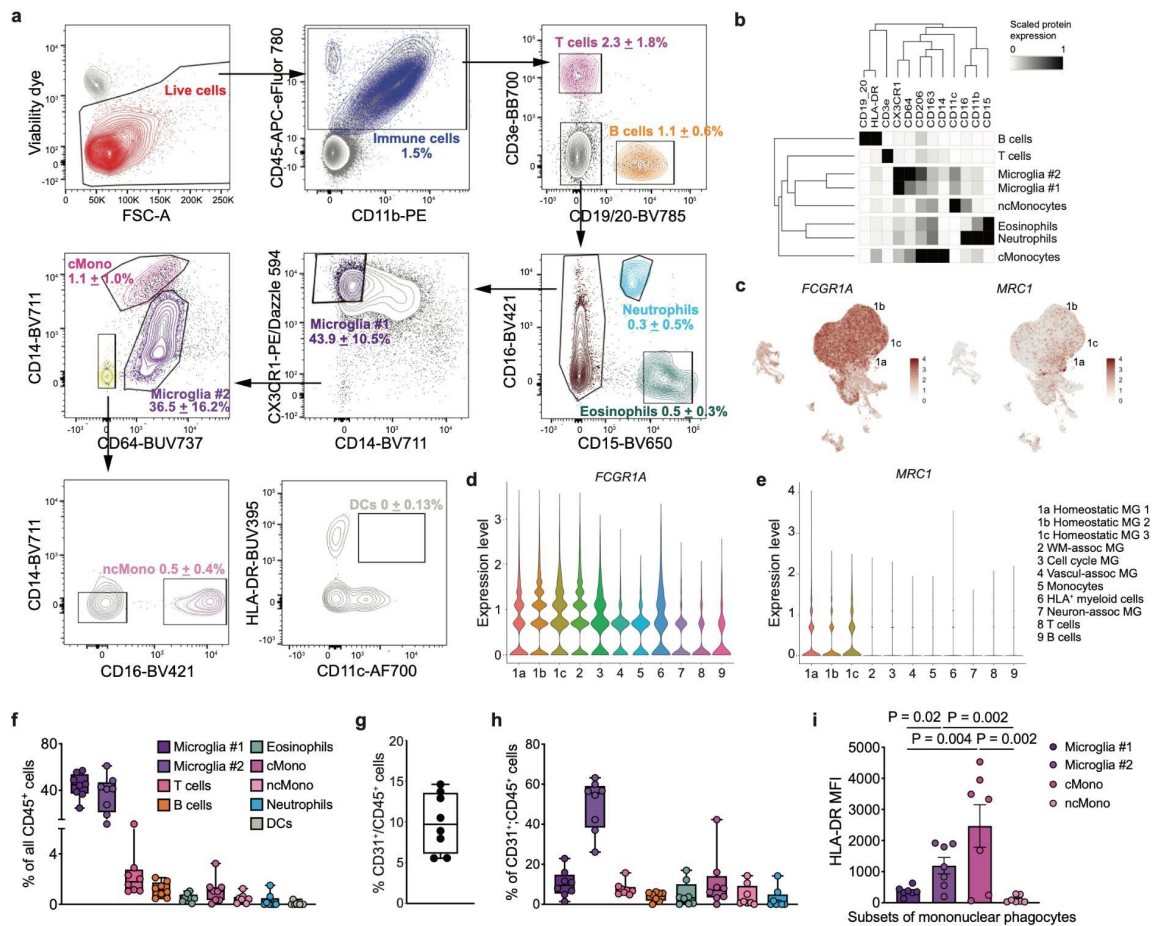
Figure 2.10: High dimensional flow cytometry confirms subtypes of CD45+ cells.
(**a**) Gating strategy used in high dimensional flow cytometry to distinguish 9 different immune cell types, including T cells, B cells, neutrophils, eosinophils, microglia (#1 and #2), classical monocytes (cMono), non-classical monocytes (ncMono), and dendritic cells (DCs). Briefly, within single live CD45+ cells, CD3e and CD19/20 positively gate T cells and B cells, respectively. From CD3e- CD19/20- cells, CD15+ CD16+ cells are gated as neutrophils and CD15+ CD16- cells are gated as eosinophils. Among CD15- cells, microglia #1 are gated as CD14- CX3CR1high. All the remaining cells that not designated as microglia #1 then proceed to the next gating, in which CD14high cells are gated as cMono and CD64+ cells are gated as microglia #2. Within CD14- CD64- cells, CD16+ cells are gated as ncMono. CD11c and HLA-DR markers confirm that HLA-DR+ cells are not likely to be DCs.
(**b**) Heatmap showing expression levels of cell surface markers in each immune cell subtype from high dimensional flow cytometry.
(**c-e**) Feature plots and violin plots showing the expression levels of *FCGR1A* (CD64) and *MRC1* (CD206) transcripts based on scRNA-seq data in **Figure 2.8a**.
(Figure caption continued on the next page.)

(Figure caption continued from the previous page.)
(**f**) Relative abundance of different immune cell subtypes among all CD45$^+$ cells.
(**g**) Relative abundance of CD31$^+$ cells among all CD45$^+$ cells.
(**h**) Relative abundance of different immune cell subtypes in CD45$^+$ CD31$^+$ cells.
(**i**) Mean fluorescence intensity (MFI) of HLA-DR in microglia #1, microglia #2, cMono, and ncMono.
Data in panels (**b**), (**f**), (**g**), (**h**), and (**i**) are from 8 independent biological samples.
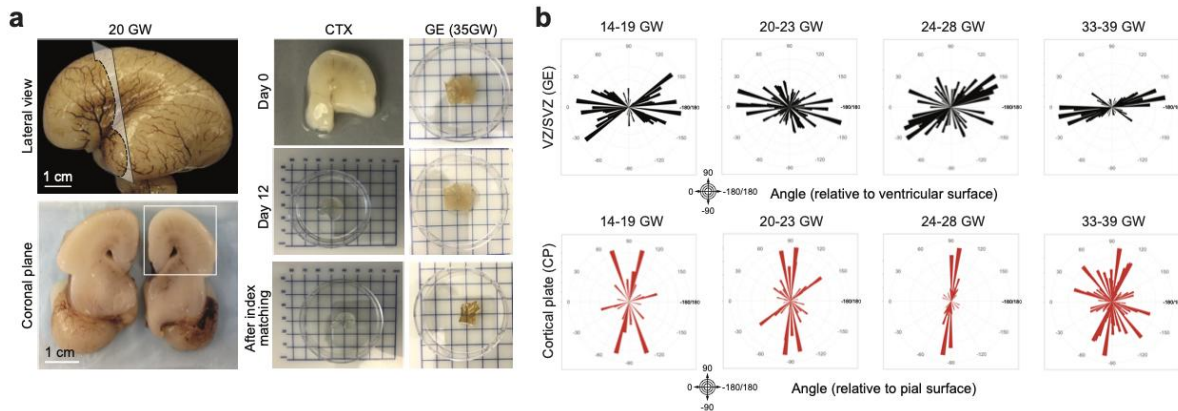
Figure S2.1: Orientations of nascent vasculature in distinct regions of prenatal human brain.
(**a**) Lateral view and coronal plane of the prenatal human brain at 20 GW, highlighting the CP section that is used for tissue clearing (left column). Tissue clearing process and index matching using SHIELD and iDISCO methods to render thick tissue sections optically transparent (right column).
(**b**) Vector mapping of the orientations of the nascent vasculature in the GE and CP. 3 independent biological samples are quantified.
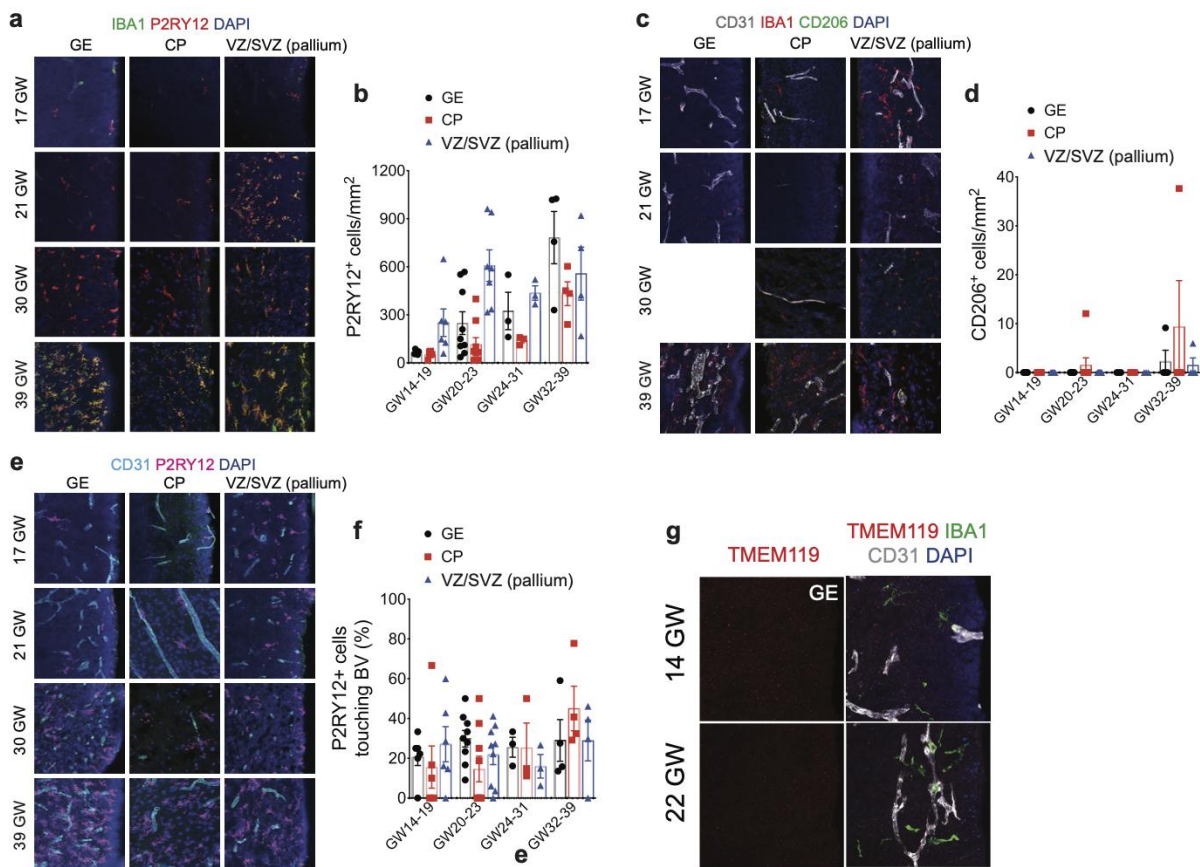
Figure S2.2: Additional markers for microglia and border-associated macrophages (BAM) in the prenatal human brain.
(**a**) Confocal images of canonical microglia marker P2RY12, along with IBA1, in the GE, CP, and VZ/SVZ of the pallium at 17, 21, 30, and 39 GW.
(**b**) Quantification of density of P2RY12$^+$ cells in the GE, CP, and VZ/SVZ of the pallium.
(**c**) Confocal images of canonical BAM marker CD206, along with IBA1 and endothelial marker CD31, in the GE, CP, and VZ/SVZ of the pallium at 17, 21, 30, and 39 GW.
(**d**) Quantification of density of CD206$^+$ cells in the GE, CP, and VZ/SVZ of the pallium.
(**e**) Confocal images of canonical microglia marker P2RY12, along with CD31, in the GE, CP, and VZ/SVZ of the pallium at 17, 21, 30, and 39 GW.
(**f**) Quantification of density of P2RY12$^+$ cells touching the blood vessels (BV) in the GE, CP, and VZ/SVZ of the pallium.
(**g**) Confocal images of canonical microglia marker TMEM119, along with IBA1 and CD31, in the GE at 14 and 22 GW.
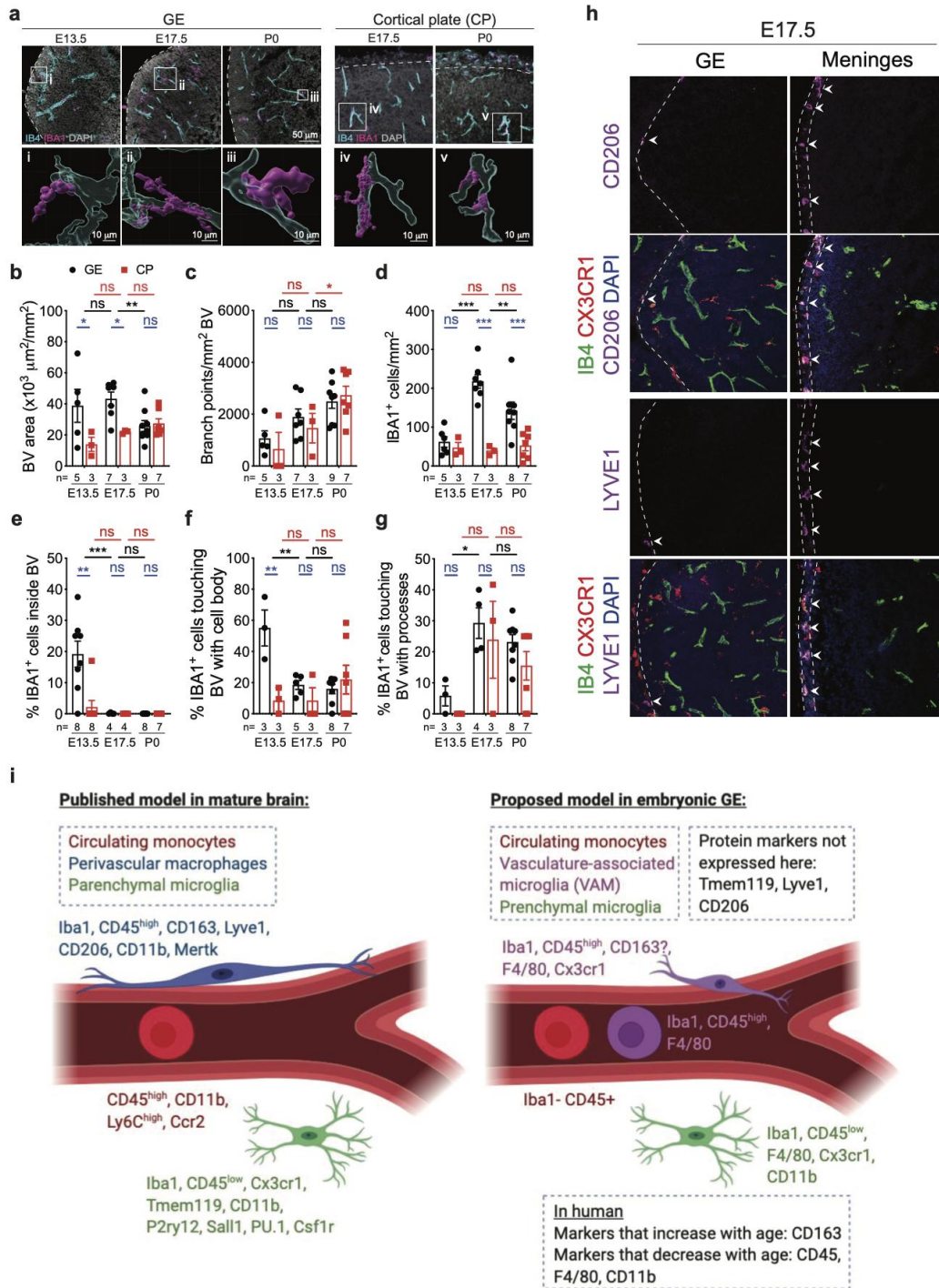
Figure S2.3: Microglia/macrophages dynamically interact with vasculature in the embryonic mouse brain.

(**a**) Confocal images and IMARIS 3D rendering of IBA1+ cells interacting with IB4+ vasculature in the GE and CP of mouse brains at E13.5, E17.5, and P0.

(Figure caption continued on the next page.)

(Figure caption continued from the previous page.)
(**b-c**) Quantification of blood vessel and vascular branch point densities in the GE and CP of mouse brains.
(**d-g**) Quantification of the density of IBA1$^+$ cells, the percentage of IBA1$^+$ cells inside blood vessels, and the percentage of IBA1$^+$ cells touching blood vessels with the cell body or processes in the GE and CP of mouse brains.
(**h**) Confocal images of canonical BAM markers CD206 and LYVE1 (white arrowheads), along with CX3CR1 and vasculature marker IB4, in the GE and meninges of mouse brains at E17.5.
(**i**) Schematic diagram summarizing the diversity of immune cells in the perivascular milieu in the mature mouse brain *vs* in the embryonic GE.
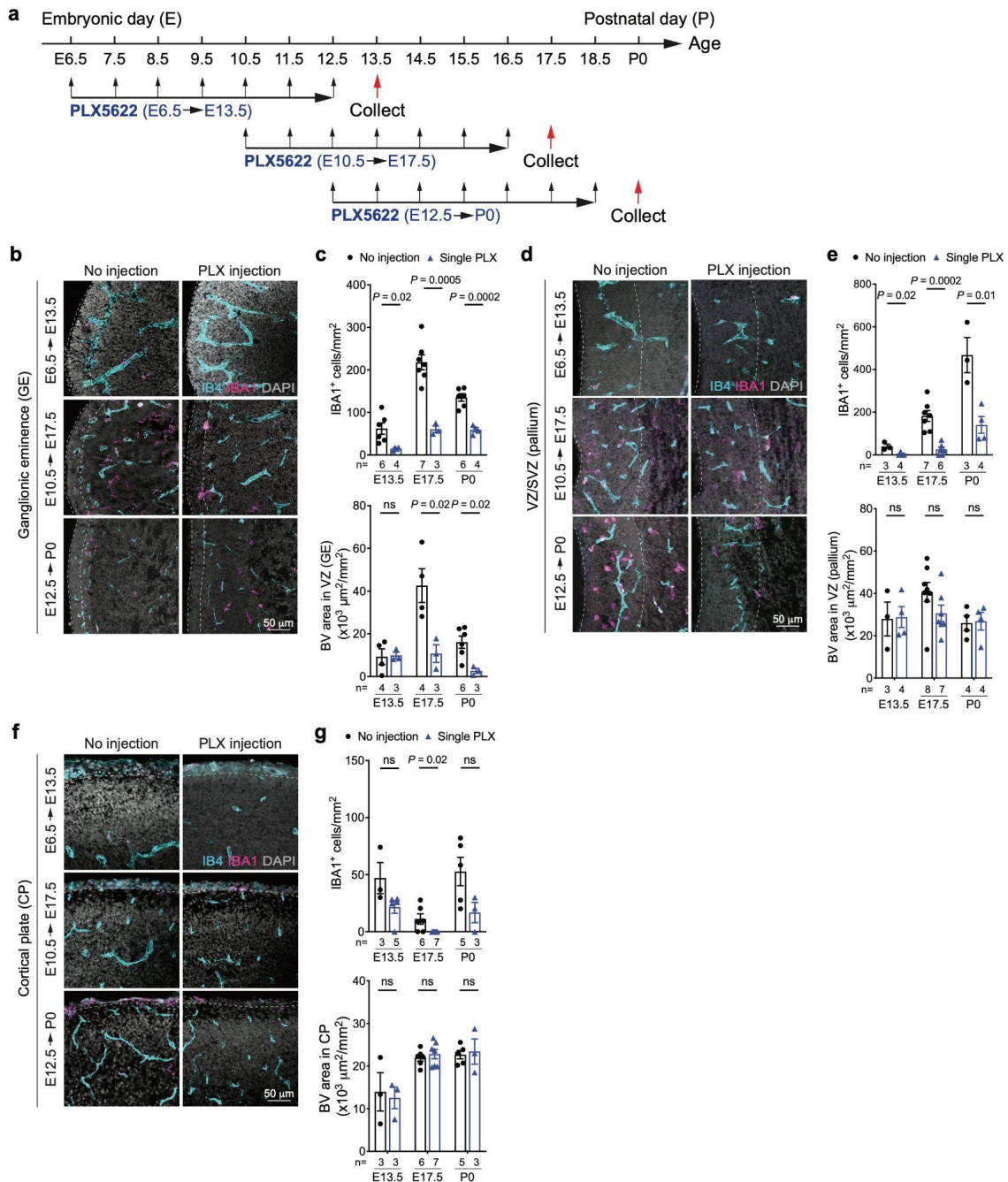
Figure S2.4: Stage-dependent and region-specific effects of microglia/macrophages in angiogenesis within the developing brain.
(**a**) Schematic diagram showing 3 schedules of PLX5622 injection in pregnant mouse dams.
(**b**, **d**, **f**) Transient inhibition of CSF1R by PLX5622 leads to significant depletion of IBA1^{+} cells in (**b**) GE, (**d**) VZ/SVZ of pallium, and (**f**) CP.
(**c**, **e**, **g**) Quantification of densities of IBA^{+} cells and IB4^{+} blood vessels in (**c**) VZ of GE , (**e**) VZ/SVZ of pallium, and (**g**) CP. Dashed lines indicate the regions in which blood vessel quantifications are performed.
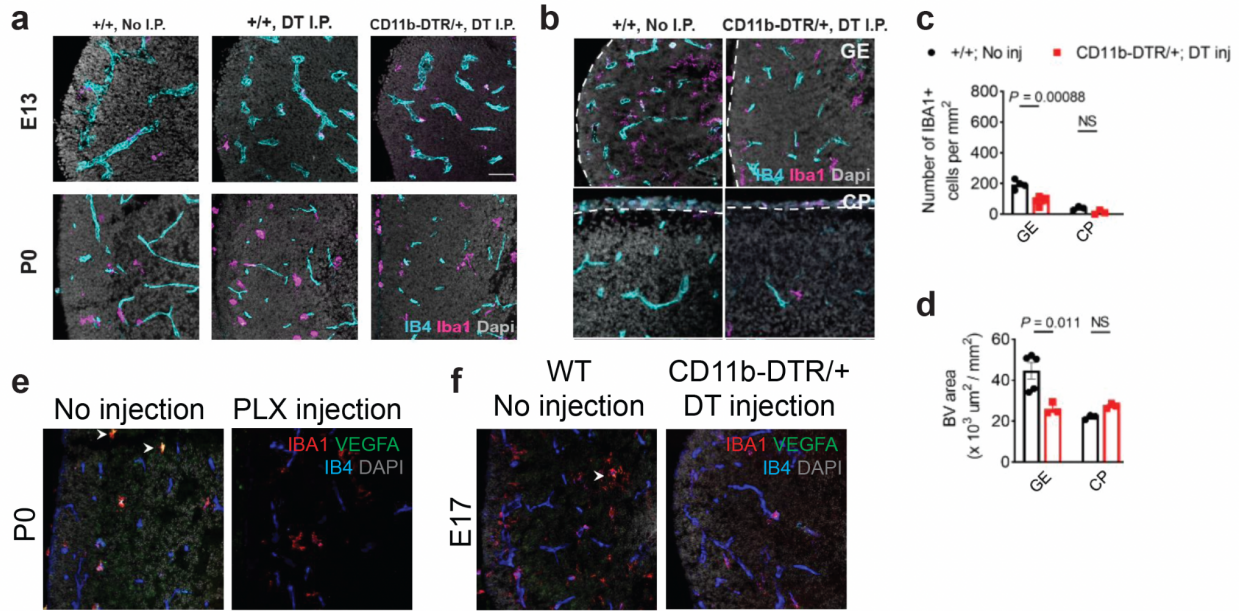
Figure S2.5: Additional mouse model confirms the role of microglia/macrophages in angiogenesis in the embryonic GE.

(**a**) Confocal images show no depletion of IBA1+ cells at E13.5 and P0 by DT injections in CD11b-DTR/+ pregnant dams.

(**b, c**) Confocal images and quantification show significant depletion of IBA1+ cells in the GE, but not in the CP, at E17.5 by DT injections in CD11b-DTR/+ pregnant dams.

(**d**) Quantification of blood vessel area in the GE and CP at E17.5 of wild-type mice with no injection, and CD11b-DTR/+ mice with DT injections.

(**e, f**) Confocal images of angiogenic factor VEGFA, along with IBA1 and IB4, in two different microglia depletion mouse models and their controls in the GE.
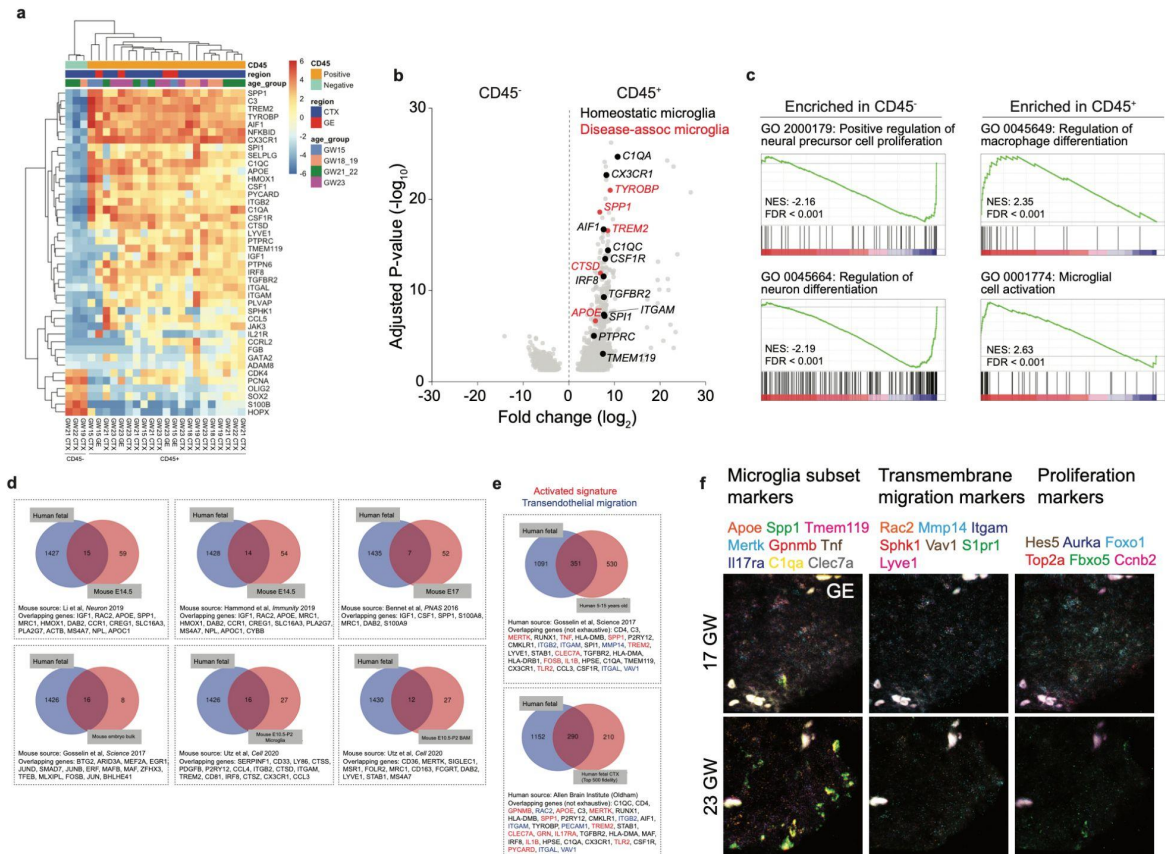
Figure S2.6: Comparison of enriched genes in CD45$^+$ cells from the bulk RNA-seq dataset in this study to those identified in other published resources.

(**a**) Heatmap of differentially expressed genes in CD45$^-$ and CD45$^+$ cells.

(**b**) Volcano plot shows the genes enriched in CD45$^+$ cells (right) and those enriched in CD45$^-$ cells (left).

(**c**) Gene set enrichment analysis (GSEA) reveals gene ontology (GO) terms enriched in CD45$^-$ and CD45$^+$ cells.

(**d**) Venn diagrams of genes enriched in CD45$^+$ cells from the human prenatal brain in this study compared with other published resources in embryonic and early postnatal mouse brains, including Li et al., 2019, Hammond et al., 2019, Bennet et al., 2016, Gosselin et al., 2017, and Utz et al., 2020.

(**e**) Venn diagrams of genes enriched in CD45$^+$ cells from the human prenatal brain in this study compared with other published resources in embryonic and early postnatal human brains, including Gosselin et al., 2017 and the Allen Brain Institute.

(**f**) Validation of marker genes in CD45$^+$ cells using RNAscope in the human GE at 17 and 23 GW.

Data from (**a-c**) are from 3 independent biological samples of CD45$^-$ cells, and 21 independent biological samples of CD45$^+$ cells.
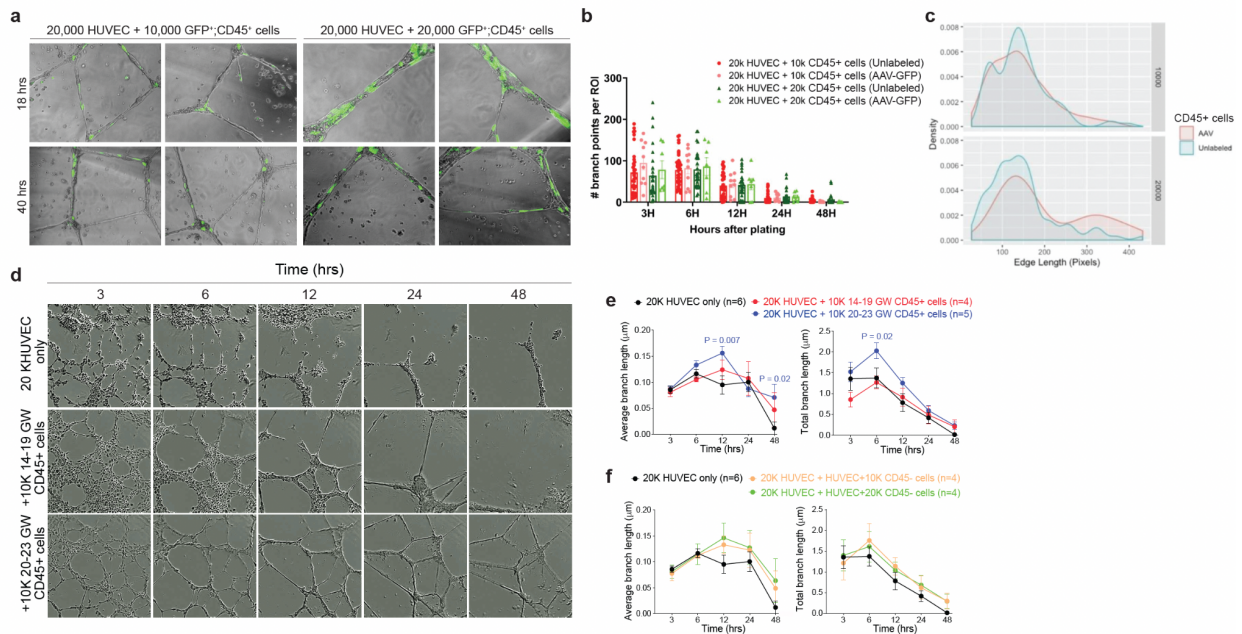
Figure S2.7: Additional analyses on HUVEC and CD45+ cell co-culture assays.
(**a**) Images taken with InCucyte S3 Live Imaging Device of HUVEC and AAV-CMV-GFP transfected CD45+ cells from the prenatal human brain at 18 and 40 hrs after plating.
(**b, c**) Quantification of the number and density of branch points formed by CD45+ cells with no transfection (No AAV) or transfected with AAV-CMV-GFP (AAV-GFP).
(**d**) Images taken with InCucyte S3 Live Imaging Device of HUVEC at 3, 6, 12, 24 and 48 hrs after plating. The conditions include 20,000 HUVEC alone, and 20,000 HUVEC co-cultured with 10,000 14-19 GW or 20-23 GW CD45+ cells.
(**e, f**) Quantification of average and total endothelial branch lengths formed by HUVEC that are co-cultured with (**e**) CD45+ cells or (**f**) CD45- cells.
The P values represent comparisons between HUVECs co-incubated with CD45+ cells *vs* HUVECs only. Not significant comparisons are not shown. n indicates the number of independent biological samples used for quantification. For each biological sample, at least 3 technical replicates are used.
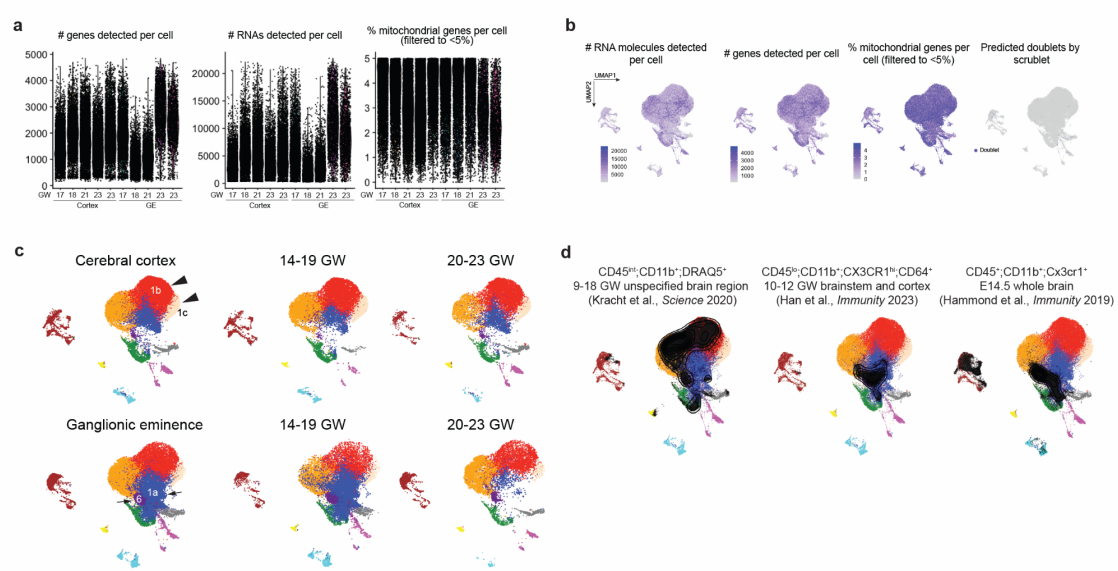
Figure S2.8: Additional scRNA-seq analyses on CD45+ cells from GE and cortex.
(**a-b**) Quantifications of the number of RNA molecules, genes, and percentage of mitochondrial genes per cell, as well as predicted doublets.
(**c**) UMAP plots show differences in the clustering of CD45+ cell subtypes from the cortex (arrowheads), and the clustering of CD45+ cell subtypes from the GE (arrows).
(**d**) Projection of published scRNA-seq datasets of microglia in the prenatal human and mouse brain onto the UMAP plot of our scRNA-seq dataset.
Data from panels (**a-d**) are from 5 independent biological samples.
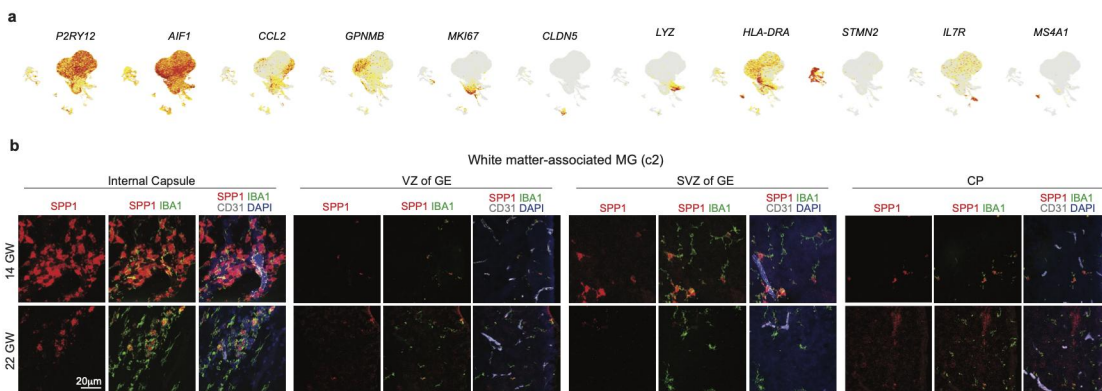
Figure S2.9: Marker genes and validation of CD45+ cell subtypes.
(**a**) UMAP plots of marker gene expressions that define each subtype of CD45+ cells.
(**b**) Confocal images of white matter-associated microglia (MG) marker *SPP1* (RNAscope probe) in IBA1+ cells in the internal capsule, VZ and SVZ of GE, and CP of 14 and 22 GW human brains.
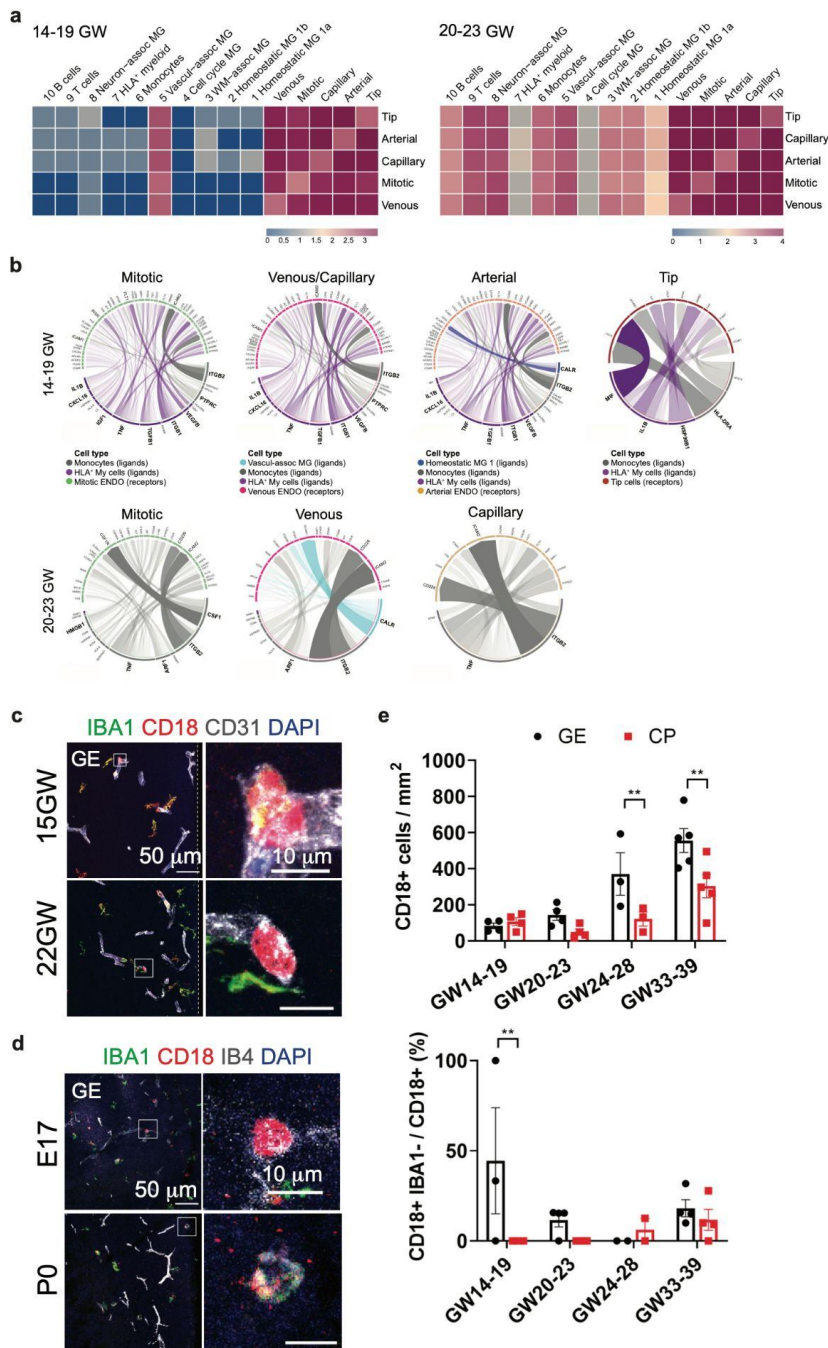
Figure S2.10: Bioinformatic analyses reveal potential signaling mechanisms that regulate interactions between CD45⁺ cell and endothelial cell subtypes.
(**a**) CellphoneDB analyses reveal stage-dependent communications via ligand-receptor pairs between CD45⁺ cell subtypes and CD31⁺ endothelial cell subtypes at 14-19 and 20-23 GW in the human brain.
(Figure caption continued on the next page.)

(Figure caption continued from the previous page.)
(**b**) NicheNet analyses predict signaling pathways used by homeostatic microglia (c1a), HLA^{+} myeloid cells, monocytes, and VAM to interact with endothelial cell subtypes at 14-19 and 20-23 GW.
(**c**) Images of CD18^{+} cells within CD31^{+} endothelium in the human GE at 15 and 22 GW.
(**d**) Images of CD18^{+} cells within IB4^{+} vascular lumen in the mouse GE at E17.5 and P0.
(**e**) Quantification of the density of CD18^{+} cells and the percentage of CD18^{+} IBA1^{-} cells in all CD18^{+} cells in the prenatal human brain.
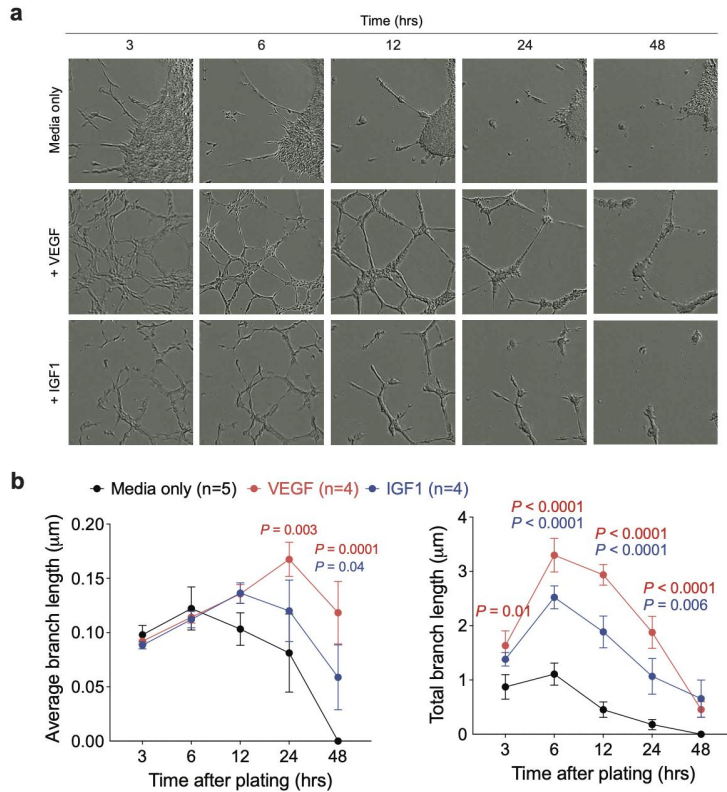
Figure S2.11: VEGF and IGF1 promote vascular morphogenesis *in vitro*.
(**a**) Images taken with InCucyte S3 Live Imaging Device of HUVEC at 3, 6, 12, 24 and 48 hrs after plating. The conditions include EGM-2 media alone or addition of VEGF or IGF1, which are ligands from CD45^{+} cells identified by NicheNet.
(**b**) Quantification of average and total endothelial branch lengths formed by HUVEC in Matrigel-based assays under conditions listed in (**a**). The P values represent comparisons between HUVECs treated with VEGF or IGF1 *vs* no treatment. Not significant comparisons are not shown. *n* indicates the number of independent biological samples used for quantification. For each biological sample, at least 3 technical replicates are used.
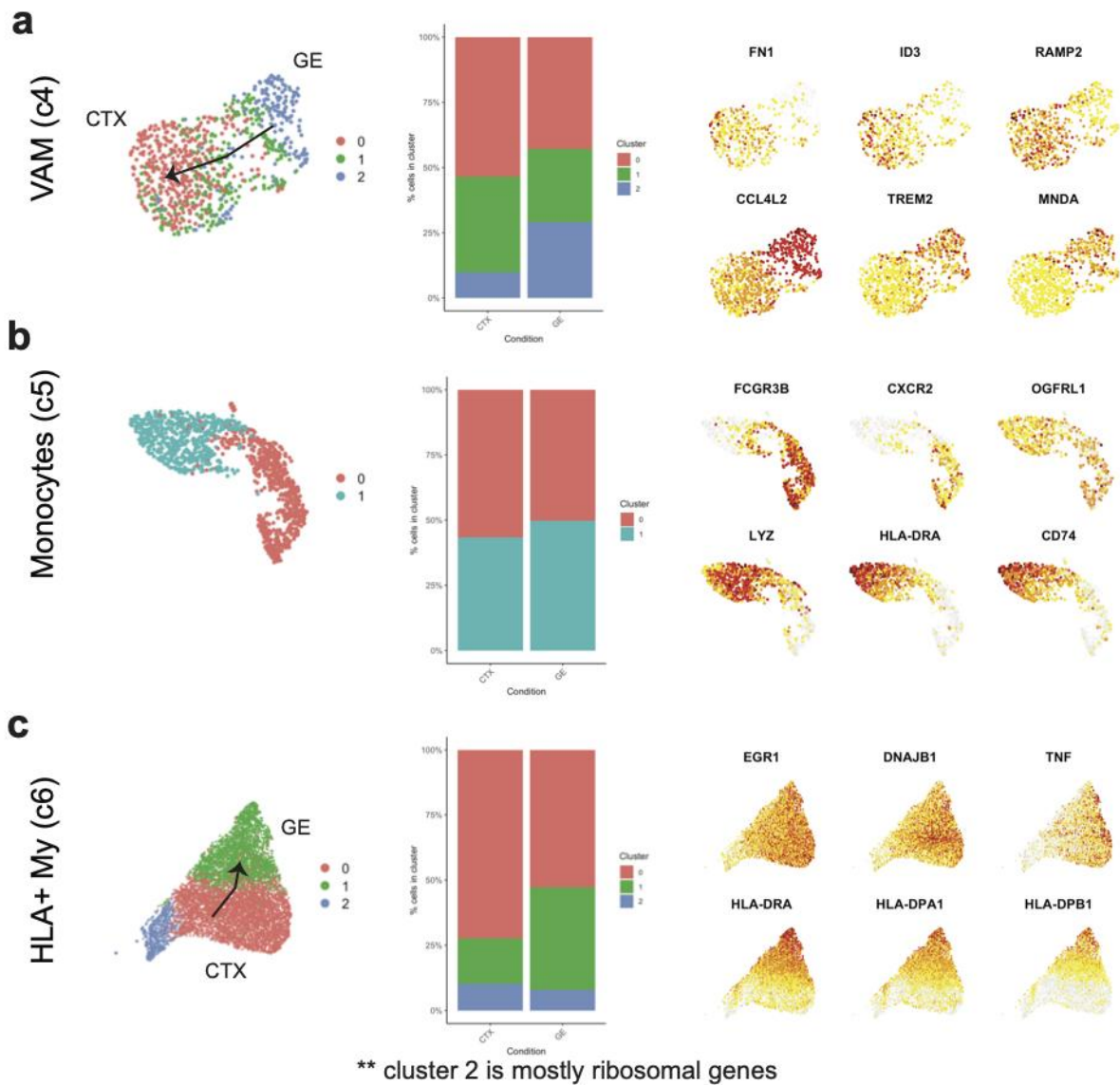
Figure S2.12: Sub-clustering of VAM, monocytes, and HLA+ myeloid cells in scRNA-seq.
(**a-c**) UMAPs of sub-clustering in (**a**) VAM, (**b**) monocytes, and (**c**) HLA+ myeloid cells (left column), in addition to their relative distributions in the cortex (CTX) and GE (middle column), and marker genes for each main sub-cluster (right column).

Chapter 3: Proinflammatory milieu disrupts angiogenesis to promote germinal matrix hemorrhage in the prenatal brain

Introduction

Globally, an estimated 15 million babies are born prematurely before 37 GW every year (Howson et al., 2012). For preterm infants born before 30 GW, 20~40% develop germinal matrix hemorrhage (GMH), which leads to devastating neurodevelopmental sequelae (Bassan et al., 2007; Volpe, 2015; Ballabh and de Vries, 2021). Germinal matrix, also known as the ganglionic eminences (GE), is enriched with neural stem and progenitor cells that give rise to GABAergic interneurons in the prenatal human brain (Hansen et al., 2013; Ma et al., 2013; Paredes et al., 2022). In addition, the GE exhibits active angiogenesis driven by diverse endothelial and mural cells that utilize a repertoire of signaling mechanisms to facilitate cell-cell communication and maturation of the nascent vasculature (Crouch et al., 2022). Interestingly, a large retrospective study based on more than 3 million mother-infant dyads shows that maternal immune activation (MIA) significantly increases the risk of brain hemorrhage and neurological comorbidities (Jain et al., 2021), raising the possibility that aberrant activation of immune cells can adversely affect angiogenesis and blood-brain barrier integrity in preterm infants.

Here, we show that CD45^{+} cells from preterm infants with GMH harbor activated neutrophils and monocytes. These cells produce bactericidal factors AZU1 and ELANE and chemokine CXCL16, which are capable of disrupting vascular integrity and causing hemorrhage in the GE. Together, our results reveal how aberrant activation of these immune cells could contribute to GMH in preterm infants.

Results

CD45$^+$ cells in GMH harbor activated neutrophils and monocytes

Having established the interactions between CD45$^+$ cell subtypes and vasculature in the homeostatic GE, we asked whether perturbations to this process could contribute to the pathogenesis of GMH. Using immunostaining, we first showed that, compared to age-matched controls, GMH cases had reduced vascular area and branch points in the GE, but not in the cortical plate (**Fig. 3.1b, Fig. 3.1d**). Although GMH cases showed similar IBA1$^+$ cell density as age-matched controls, they had significantly lower percentage of IBA1$^+$ cells inside the vascular lumen in the GE, but not in the cortical plate (**Fig. 3.1c, Fig. 3.1e**). To investigate the composition of immune cells in GMH cases, we performed scRNA-seq using FACS-isolated CD45$^+$ cells from the GE and cortex from two 24-25 GW GMH cases and two age-matched controls (**Fig. 3.2a**). After filtering out doublets and low-quality cells, we obtained 35,275 cells with 2,098 genes per cell (**Fig. S3.1a-b**). Clustering yielded 9 subtypes with similar marker genes as those found in the scRNA-seq dataset from control CD45$^+$ cells (**Fig. 2.8a, Fig. 3.2a, Fig. S3.1c**). Compared to control CD45$^+$ clusters, GMH cases showed reduced percentages of homeostatic microglia (c1a, c1b), but modest increases in cell cycle microglia (c3), monocytes (c5), and T cells (c8) (**Fig. 3.2b**).

Furthermore, CD45$^+$ cells in GMH cases contained a markedly expanded population of neutrophils (c9) that expressed high abundance of *ELANE, AZU1, and DEFA4*, which encode for antimicrobial factors Elastase, Azurocidin 1, and Defensin Alpha 4, respectively (**Fig. 3.2c, Fig. S3.1d**). To further characterize the contribution of neutrophils to GMH, we performed immunostaining and showed an enriched population

of ELANE⁺ cells in the GE and cortical plate of GMH cases compared to age-matched controls **(Fig. 3.3a-b).** Many ELANE⁺ cells packed the vascular lumen, and a significant number migrated into the GE parenchyma close to the hemorrhagic site (**Fig. 3.3a**). Finally, immunostaining confirmed co-expression of ELANE and CD16 (non-classical monocyte marker) in GMH cases, where ELANE⁺ CD16⁺ cells had higher abundance in the GE (**Fig. S3.1e**). These results suggest that the neutrophil cluster may contain additional non-classical monocytes.

In addition to activated neutrophils, DEG analysis in CD45⁺ cells from GMH cases showed downregulation of homeostatic microglia genes (*CX3CR1, P2RY12, IGF1, SALL1*) and integrins (*ITGAV, ITGAX*), and upregulation of genes in the complement pathway (*C1QA, C1QB, C1QC*), monocytes (*CD14, S100A9, S100A8*), neutrophils (*AZU1, ELANE, MPO, DEFA4*), and chemokine *CXCL16* (**Fig. 3.2c**). Similar transcriptomic changes were captured in several CD45⁺ cell subtypes closely associated with the GE vasculature, including VAM, monocytes, HLA⁺ myeloid cells, and neutrophils (**Fig. S3.2a**). GO analysis of DEGs in these CD45⁺ cell subtypes from GMH cases collectively revealed upregulation of cellular stress, neutrophil degranulation, and phagosomes, as well as downregulation of leukocyte migration and cellular response to cytokine stimulus (**Fig. S3.2b-c**).

ELANE, AZU1, and CXCL16-S1PR1 pathway disrupt vascular integrity and morphogenesis

The expressions of *ELANE* and *AZU1* in the neutrophil cluster broached the hypothesis that these antimicrobial factors may negatively impact angiogenesis in GMH.

Indeed, Azurocidin 1 (AZU1) has been shown to increase vascular endothelial permeability and recruit monocytes during inflammation (Edens and Parkos, 2003). To test this, we generated 3D microvessels by seeding human microvascular endothelial cells (HMVECs) into a microfluidic channel lumen surrounded by collagen extracellular matrix (**Fig. 3.4a**) (Polacheck et al., 2019). We then flowed AZU1 (100 mg/ml) intraluminally for 18 hours. This treatment significantly disrupted VE-cadherin junctional complexes between endothelial cells and increased microvessel permeability, allowing fluorescently labeled 70-kDa dextran to diffuse from the lumen into the interstitial matrix (**Fig. 3.4b-c**). To determine whether CD45^{+} cell-mediated endothelial branch formation could be impacted by these factors, we tested AZU1 along with 10,000 CD45^{+} cells in the HUVEC assay and showed that total branch length decreased in AZU1-treated cultures with HUVEC and CD45^{+} cells (**Fig. 3.5a-b**). Finally, we added AZU1 or ELANE to HUVEC that have been pretreated with VEGF in the Matrigel assay. These results showed that AZU1 or ELANE suppressed VEGF-mediated branch morphogenesis in HUVEC (**Fig. 3.5c-d**). Together, these results showed that AZU1 and ELANE, secreted by activated neutrophils in GMH cases, could disrupt the nascent vasculature.

Given the broad transcriptomic changes in CD45^{+} cells from GMH cases, we asked what signaling pathways between immune and endothelial cells might contribute to hemorrhage in the GE particularly. To this end, we performed NicheNet analysis on scRNA-seq datasets to identify cell-cell communication pathways between CD45^{+} cells and endothelial cells that were enriched in GMH cases compared to age-matched controls (**Fig. 3.6a**). This approach revealed several ligands enriched in CD45^{+} cells from GMH cases, including CXCL16, TNFSF13B, TNFSF13, SERPINA1 and calreticulin

(CALR), that could promote vascular dysfunction (**Fig. 3.6b-c**). Among these,

CXCL16-mediated signaling pathways were particularly intriguing because of its broad

implications in inflammation under diverse disease conditions (Darash-Yahana et al.,

2009). Indeed, NicheNet analysis revealed a diverse repertoire of candidate receptors

and target genes that could be activated by CXCL16, and violin plots showed increased

expression of CXCL16 in several CD45^{+} cell subtypes, especially in monocytes (**Fig.

3.6c-d**). In support of these results, *in situ* hybridization showed significant upregulation

of *CXCL16* transcripts in IBA1^{+} S100A9[+] monocytes in the GE of GMH cases, but not in

control cases (**Fig. 3.6e**). Similar to the effects of AZU1, treating 3D microvessels with

CXCL16 and ELANE (both at 20 mg/ml) disrupted VE-cadherin junctional complexes

and increased vascular permeability (**Fig. 3.7a-b**). Furthermore, 3D Matrigel-based

HUVEC assays showed that CXCL16 (10 mg/ml) suppressed VEGF-mediated vascular

morphogenesis (**Fig. 3.7c-d**). Together, these results demonstrated that CXCL16 from

monocytes, when combined with neutrophil-secreted ELANE, could cause vascular

dysfunction in the GE of GMH cases.

Next, we examined the expression of CXCL16 signaling partners in endothelial

cells as predicted by NicheNet. Among these, CXCL16 receptor *CXCR6* was expressed

at very low or near undetectable level in endothelial cells from control and GMH cases,

but *S1PR1* was upregulated in endothelial cells from GMH cases (**Fig. 3.8a**). Since S1P

gradient provides a spatial cue for the trafficking of immune cells and the localization of

S1PR1 is dynamically regulated in vascular cells (Cyster and Schwab, 2012; Mendelson

et al., 2014), dysregulated *S1PR1* signaling in endothelial cells from GMH cases is likely

to disrupt homeostatic interactions between immune cells and the nascent vasculature.

To test this, we asked whether deleting S1PR1 in endothelial cells could affect angiogenesis and leukocyte egression during brain development. To this end, we deleted *S1PR1* in endothelial cells using *Cdh5-Cre* (*Cdh5-Cre;S1pr1^{fl/fl}*) (Di Marco et al., 2020). At E12.5, *Cdh5-Cre;S1pr1^{fl/fl}* mice expressed tight junction protein ZO-1 (also known as tight junction protein 1 or TJP1) in their nascent vasculature and had comparable proliferation rates in IBA1⁺ cells as controls (**Fig. S3.3a-b**). However, E12.5 *Cdh5-Cre;S1pr1^{fl/fl}* mice showed a significant increase in the density of IBA1⁺ cells and decrease in the percentage of IBA1⁺ cells attached to blood vessels in the GE, but not in the cortical plate (**Fig. 3.8b-c**). Similarly, TEM showed that in E12.5 control embryos blood cells were confined within the GE vasculature (**Fig. 3.8d, panels i-ii**). In contrast, myeloid cells in the GE of E12.5 *Cdh5-Cre;S1pr1^{fl/fl}* mice appeared to have migrated across endothelial cells into the brain parenchyma (**Fig. 3.8d, panels iii-iv**). IBA1⁺ cells from *Cdh5-Cre;S1pr1^{fl/fl}* mice contained significantly more abundant CD68⁺ vesicles in the GE, but not in the cortical plate (**Fig. 3.8e-f**), suggesting that deleting S1PR1 in endothelial cells selectively activated microglia in the GE. In addition, IBA1⁺ cells in the GE of *Cdh5-Cre;S1pr1^{fl/fl}* mice showed increased expression of CXCL16 and CD16 (**Fig. 3.8g-h, Fig. S3.3c**), similar to findings in human cases with GMH (**Fig. S3.4a-b**). However, no difference in CD68⁺ vesicle volume in IBA1⁺ cells was identified between control and GMH cases. Consistent with these results, our scRNA-seq dataset showed that many CD45⁺ cell subtypes in GMH upregulated inflammation-related genes *ITGB2* and *FCGR3A* (encodes CD16), downregulated angiogenic factors *IGF1* and *TNF*, and showed no change in complement *C3* and *CD68* (**Fig. S3.4c-e**). Intriguingly, deleting another component of the Notch pathway in an endothelial cell-specific manner

(*Cdh5-CreER;Rbpj^{fl/fl}*) did not result in microglia-related phenotypes as seen in *Cdh5-Cre;S1pr1^{fl/fl}* mice at E12.5 (**Fig. S3.3d-h**). This suggested that S1PR1 specifically led to disrupted immune-vascular interactions and perhaps vascular permeability, and not the Notch pathway in general. Together, these results indicate that loss of S1PR1 in endothelial cells can have reciprocal effects in activating IBA1$^+$ cells and thereby upregulating their CD16 and CXCL16 expression, mirroring the immune cells in GMH.

Maternal exposure to ELANE and CXCL16 promotes hemorrhage in GE

To examine the role of neutrophil- and monocyte-derived factors *in vivo*, we intraperitoneally (IP) injected wild-type timed pregnant dams with a combination of ELANE and CXCL16 (each at 3 mg/g of body weight or ~40mg/ml) at E12.5 and collected embryos at E13.5 or injected at E13.5 and E15.5 and collected embryos at E17.5 (**Fig. 3.9a**). To ensure that ELANE and CXCL16 reached circulation, we performed ELISA assays using plasma from control and ELANE/CXCL16-injected pregnant dams. These results showed significantly higher concentration of ELANE in ELANE-treated E13.5 pregnant dams and modest increase in ELANE-treated E17.5 pregnant dams (**Fig. 3.9b**). Similarly, increased concentration of CXCL16 was observed in the plasma of E13.5 pregnant dams injected with CXCL16 at E12.5, but no detectable increase in CXCL16 was found in the plasma of E17.5 pregnant dams injected with CXCL16 at E13.5 and E15.5 (**Fig. 3.9b**). Histopathological examinations revealed that injection of ELANE/CXCL16 at E12.5 significantly reduced vascular area and disrupted vascular barrier integrity, resulting in an accumulation of Ter119$^+$ red blood cells (RBCs) in the VZ of GE at E13.5, but not in the VZ/SVZ of pallium or in the cortical plate (**Fig.**

3.10a-b). Three out of seven ELANE/CXCL16-treated E13.5 embryos showed more severe phenotypes with intraventricular hemorrhage (**Fig. S3.5a-b**). ELANE/CXCL16-treated embryos also showed slightly higher density of leaked RBCs and IBA1$^+$ cells in the meninges compared to control embryos, though the comparison was not statistically significant (**Fig. S3.5a-b**). Interestingly, reduced vascular area in the GE of ELANE/CXCL16- treated embryos at E13.5 did not result from apoptosis in endothelial cells, as shown in the lack of cleaved caspase 3 staining in ELANE/CXCL16 treated embryos (**Fig. S3.5c**). On the other hand, E17.5 embryos from pregnant dams injected with the same dosage of ELANE/CXCL16 did not show obvious hemorrhage. Regardless, these E17.5 embryos showed reduced vascular areas in the VZ of GE and higher density of IBA1$^+$ cells in the GE and lateral ventricle, but not in the VZ/SVZ of pallium or in the cortical plate (**Fig. 3.10c-d**), suggesting that this injection scheme has led to region-specific immune activation.

Our MIA model with ELANE/CXCL16 injections showed a more drastic phenotype than that of a more established MIA model with lipopolysaccharide (LPS) injections. Specifically, mouse embryos injected with LPS at E12.5 and collected at E17.5 showed no difference in microglia density, but a decrease in blood vessel area in the GE (**Fig. S3.6a-c**). Together, these results support that neutrophil- and monocyte-derived proinflammatory factors, including AZU1, ELANE, CXCL16, can disrupt vascular integrity and promote the pathogenesis of GMH.

Discussion

GMH is a life-threatening condition in preterm infants, but why nascent vasculatures in the germinal matrix are vulnerable to rupture remain unclear. This study shows that CD45^{+} cells from GMH contain activated neutrophils that produce bactericidal factors to disrupt vascular barrier and angiogenesis in the GE. Furthermore, maternal exposure to CXCL16/ELANE and disrupting S1PR1 signaling in endothelial cells promote the formation of GMH, supporting that a proinflammatory milieu can indeed damage the nascent vasculature and facilitate the egress of activated immune cells into the GE (**Fig. 3.8-10**). Collectively, these results provide important insights into how perturbations to the homeostatic immune-vascular interaction in the GE promote GMH, a leading cause of mortality and neurodevelopmental disorders (Howson et al., 2012; Bassan et al., 2007; Volpe, 2015; Jain et al., 2021).

Building on our data that elucidate how the brain's innate immune cells regulate angiogenesis in the prenatal human brain under physiological conditions, our results uncover at least two mechanisms by which perturbations to immune-vascular interactions contribute to GMH. First, our results identify a significant expansion of neutrophils that produce bactericidal factors, including ELANE and AZU1, to disrupt the integrity of nascent vasculature in the GE of GMH cases (**Fig. 3.2-5**). Indeed, histopathological examinations reveal many ELANE[+] neutrophils traveling across capillaries into the brain parenchyma (**Fig. 3.3**). Furthermore, engineered microvessels and 3D Matrigel assays show that AZU1 can disrupt vascular barrier permeability as well as VEGF- and CD45^{+} cell-mediated vascular morphogenesis in HMVECs and HUVECs, respectively (**Fig. 3.4-5**). Second, aside from the bactericidal factors

produced by activated neutrophils, we show that CD45^{+} cell subtypes critical for

vascular development in the GE exhibit prominent transcriptomic changes that suggest

their immune activation. Among signaling pathways identified in activated CD45^{+} cell

subtypes, upregulation of CXCL16 in monocytes most likely creates a proinflammatory

milieu to disrupt vascular integrity (**Fig. 3.6**). Indeed, CXCL16, combined with ELANE,

disrupts VE-cadherin junctional complexes of endothelial cells in 3D engineered

microvessels (**Fig. 3.7a-b**). In Matrigel assays, CXCL16 alone is sufficient to inhibit

VEGF-mediated branch morphogenesis of HUVEC (**Fig. 3.7c-d**). In support of these

results, intraperitoneal (IP) injection of ELANE/CXCL16 in pregnant dams at E12.5

disrupts vascular integrity and leads to hemorrhage in the VZ of GE and lateral

ventricle, but not in the VZ/SVZ of pallium or in the cortical plate at E13.5 (**Fig. 3.10a-b,

Fig. S3.5**). In contrast, ELANE/CXCL16 injection in dams at E13.5 and E15.5 reduces

vascular density and increases IBA1^{+} cell density in the GE at E17.5 without causing

apparent hemorrhage (**Fig. 3.10c-d**).

How does CXCL16 disrupt angiogenesis in the embryonic mouse brain?

Although the expression of CXCR6, the cognate receptor for CXCL16, is almost

undetectable in endothelial cells from control and GMH cases, NicheNet analysis shows

that the expression of S1PR1 is upregulated in endothelial cells from GMH cases (**Fig.

3.8a**), which most likely disrupts the S1P gradient required for the migration of immune

cells across vascular barriers (Cyster and Schwab, 2012; Mendelson et al., 2014). In

support of this idea, endothelial cell-specific knockout of S1PR1 in embryonic mice

leads to prominent infiltration of peripheral immune cells, including many that express

CD16 and CXCL16 (**Fig. 3.8g-h, Fig. S3.3c**). These results suggest that CXCL16 and

S1PR1 may constitute reciprocal interactions between immune cells and endothelial cells. As such, upregulation of CXCL16 in subsets of CD45$^+$ cells and disruption of S1PR1 in endothelial cells could propagate a vicious cycle that exacerbates the egress of activated peripheral immune cells across the primitive BBB in GMH.

Taken together, our results provide key mechanistic insights in how maternal immune activation, mediated via activation of neutrophils and monocytes in preterm infants, promotes the pathogenesis of GMH (**Fig. 3.11**). Given the high prevalence of maternal infection in preterm infants with high neurodevelopmental comorbidities (Jain et al., 2021; Egesa et al., 2021; McCrea and Ment, 2008), our study also provides important therapeutic targets to prevent and mitigate these devastating conditions.

Figures
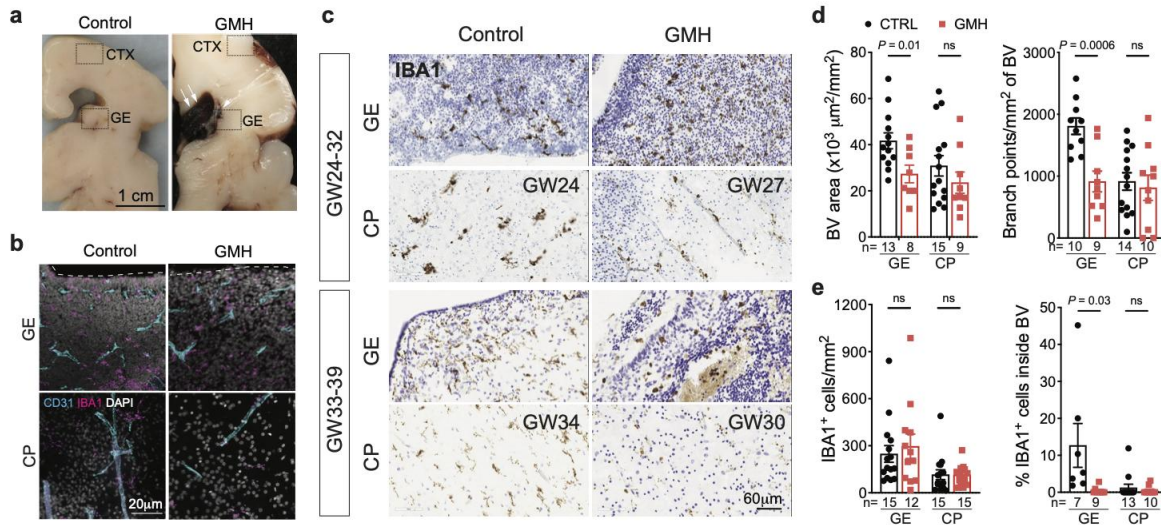
Figure 3.1: GMH cases show decreased vascular density and complexity in GE.
(**a**) Gross images of coronal sections of a control prenatal brain (23 GW) and a brain with GMH (24 GW) (arrows). Boxed areas highlight cortex (CTX) and GE.
(**b**) Confocal images show IBA1$^+$ cells and their relationship with CD31$^+$ endothelial cells in the GE and CP of age-matched prenatal control and GMH human brains.
(**c**) Immunohistochemistry staining of IBA1 in prenatal control and GMH human brains.
(**d**) Quantification of densities of blood vessels and vascular branch points in the GE and CP of control (CTRL) and GMH cases.
(**e**) Quantification of density of IBA1$^+$ cells and percentage of IBA1$^+$ cells inside blood vessels in the GE and CP of CTRL and GMH cases.
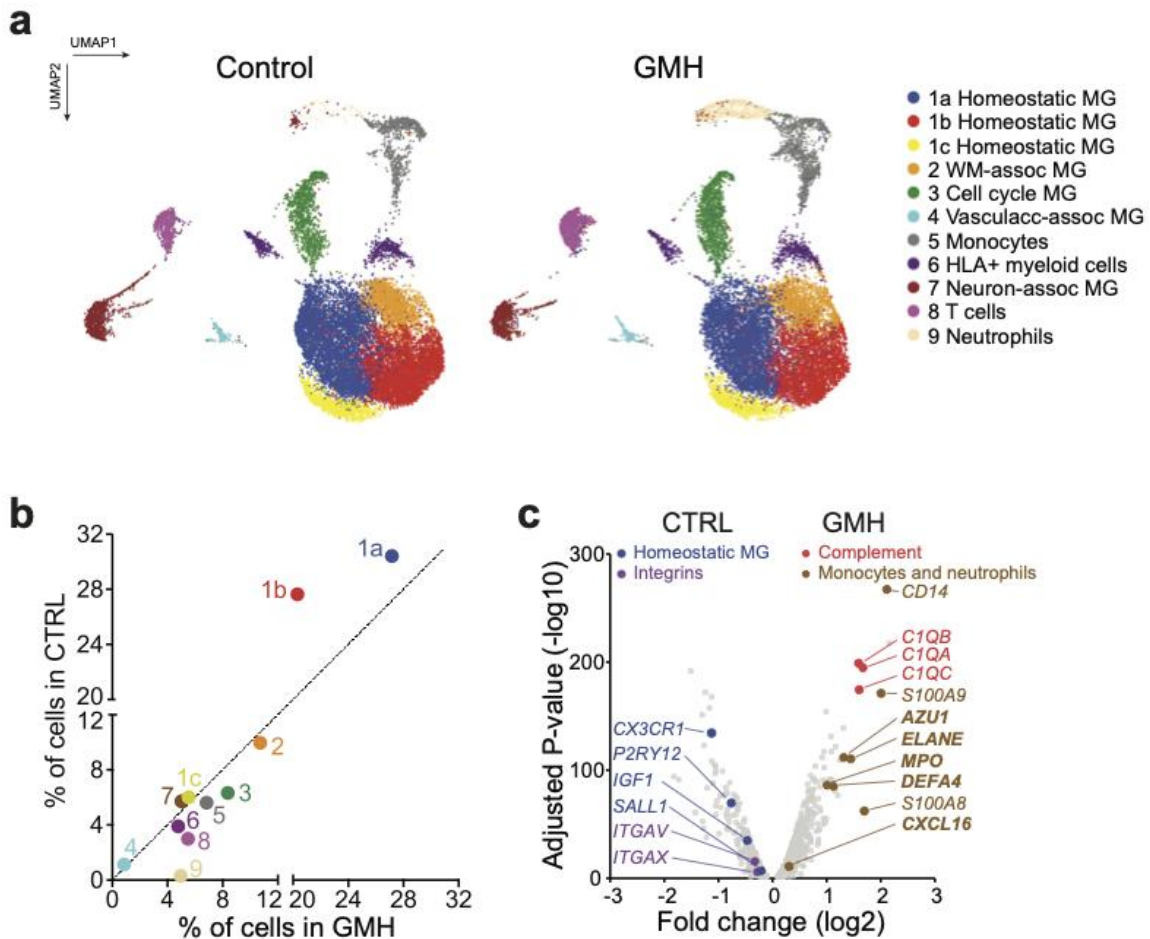
Figure 3.2: Single-cell transcriptomics in CD45⁺ cells from GMH cases reveal activated neutrophils.

(**a**) UMAP plots comparing CD45⁺ cell subtypes from age-matched control and GMH cases. Data are from 2 biological samples in each condition (Control, GMH).

(**b**) A distribution plot comparing the relative abundance of each CD45⁺ cell subtype in control *vs* GMH cases.

(**c**) Volcano plot shows DEGs identified by pseudo-bulked scRNA-seq data in CD45⁺ cells from GMH *vs* CTRL cases and the GO terms they define.
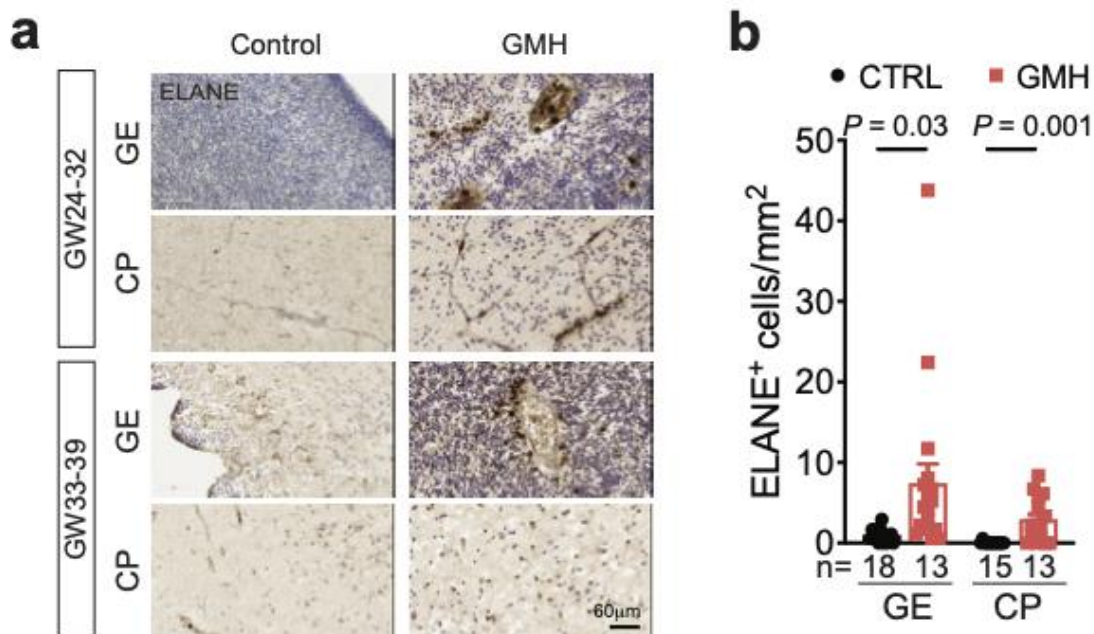
Figure 3.3: Neutrophil infiltration in GMH cases.
(**a-b**) Immunohistochemical stain for ELANE and quantification show increased number of neutrophils in GE and CP of GMH cases.
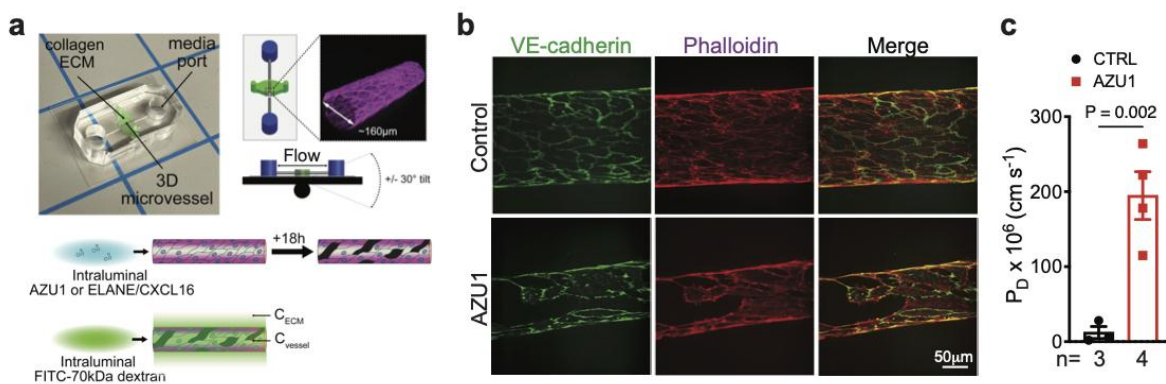
Figure 3.4: Neutrophil-secreted AZU1 increases vascular permeability.
(**a**) Experimental set-up of *in vitro* vascular permeability assay using 3D microfluidic microvessels within collagen extracellular matrix (ECM). Rocker at 30-degree tilt creates oscillatory shear stress to facilitate endothelial junction formation.
(**b**) Fluorescence micrographs of VE-cadherin and actin in control and AZU1-treated microvessels.
(**c**) Quantification of vascular permeability in control and AZU1-treated microvessels.

Figure 3.5: Neutrophil-secreted AZU1 and ELANE suppress VEGF- and CD45+ cell-assisted vascular morphogenesis.
(**a**) Images taken with InCucyte S3 Live Imaging Device of HUVEC in Matrigel-based branching morphogenesis at 3, 6, 12, 24 and 48 hrs after plating. The conditions include HUVEC alone, and HUVEC co-cultured with CD45+ cells from the prenatal human brain with or without the addition of AZU1.
(**b**) Quantification of total branch lengths formed by HUVEC under conditions in (**a**).
(**c**) Images taken with InCucyte S3 Live Imaging Device of HUVEC in Matrigel-based branching morphogenesis at 3, 6, 12, and 24 hrs after plating. The conditions include VEGF-primed HUVEC with or without the addition of ELANE or AZU1.
(**d**) Quantification of total branch lengths formed by HUVEC under conditions in (**c**).
In panel (**b**), P values represent comparisons between HUVECs co-cultured with CD45+ cells *vs* HUVECs only. In panel (**d**), P values represent comparisons between VEGF-primed HUVECs treated with AZU1 or ELANE *vs* VEGF-primed HUVECs only. Not significant comparisons are not shown. *n* indicates the number of independent biological samples used for quantification. For each biological sample, at least 3 technical replicates are used.
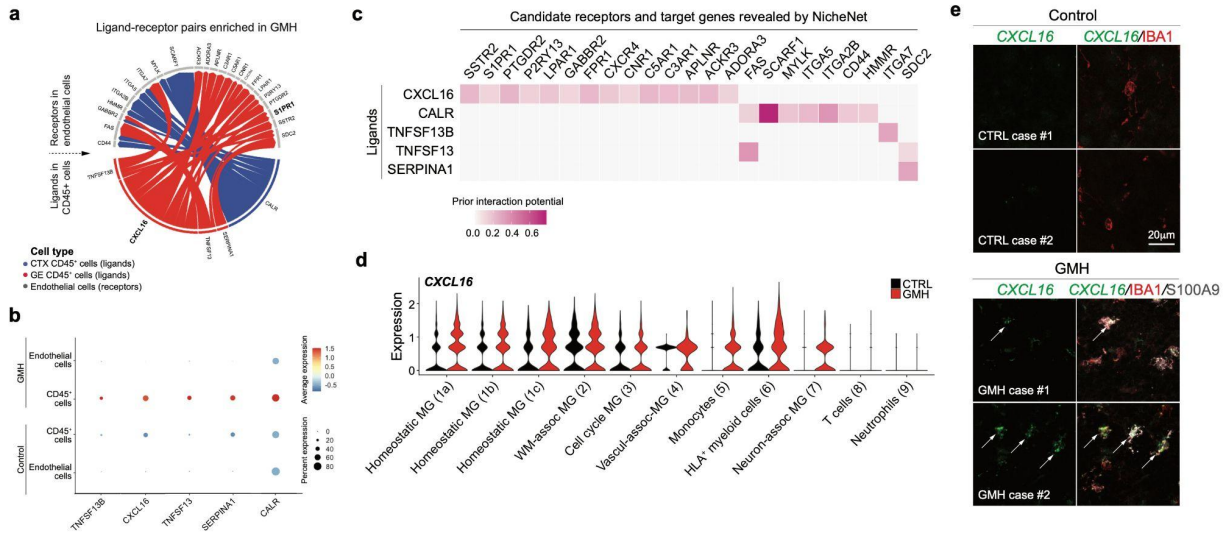
Figure 3.6: Upregulation of CXCL16 in monocytes from GMH cases.
(**a, c**) (**a**) Wheel plot and (**c**) heatmap from NicheNet analysis show predictions of ligand-receptor pairs between CD45$^+$ cells and CD31$^+$ endothelial cells that are differentially regulated in GMH. Ligands in CD45$^+$ cells are separated by their regional preferences (GE or CTX) in (**a**). Color intensity in (**c**) correlates to interaction potential.
(**b**) Dot plot shows higher expressions of ligands TNFSF13B, CXCL16, TNFSF13, SERPINA1, CALR in CD45$^+$ cells from GMH cases, compared to those from age-matched controls.
(**d**) Violin plots show upregulated expression of CXCL16 in most CD45$^+$ cell subtypes in GMH cases.
(**e**) *Cxcl16* RNAscope signals (arrows) in IBA1$^+$ S100A9$^+$ cells in control and GMH cases.
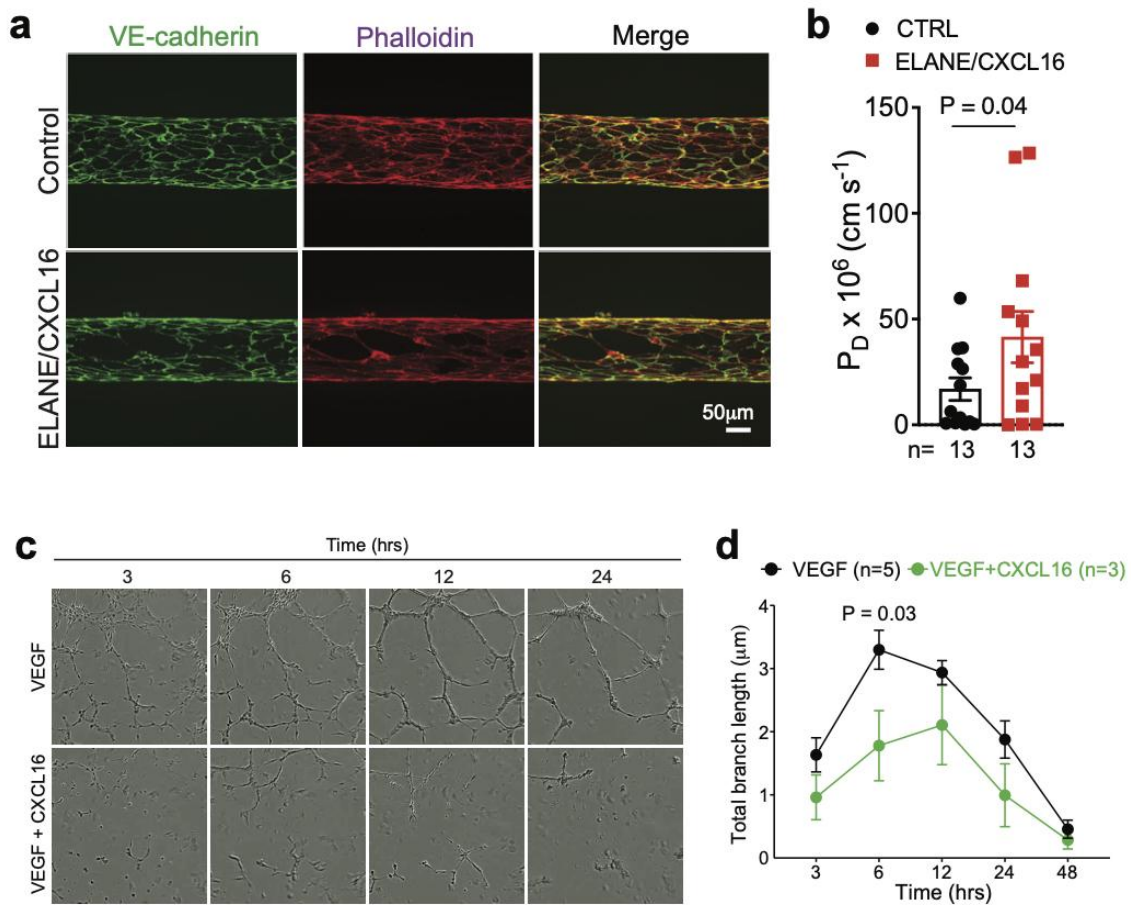
Figure 3.7: CXCL16 and ELANE disrupt vascular barrier and development.
(**a**) Fluorescence micrographs of VE-cadherin and actin in control and
ELANE/CXCL16-treated microvessels.
(**b**) Quantification of vascular permeability in control and ELANE/CXCL16-treated
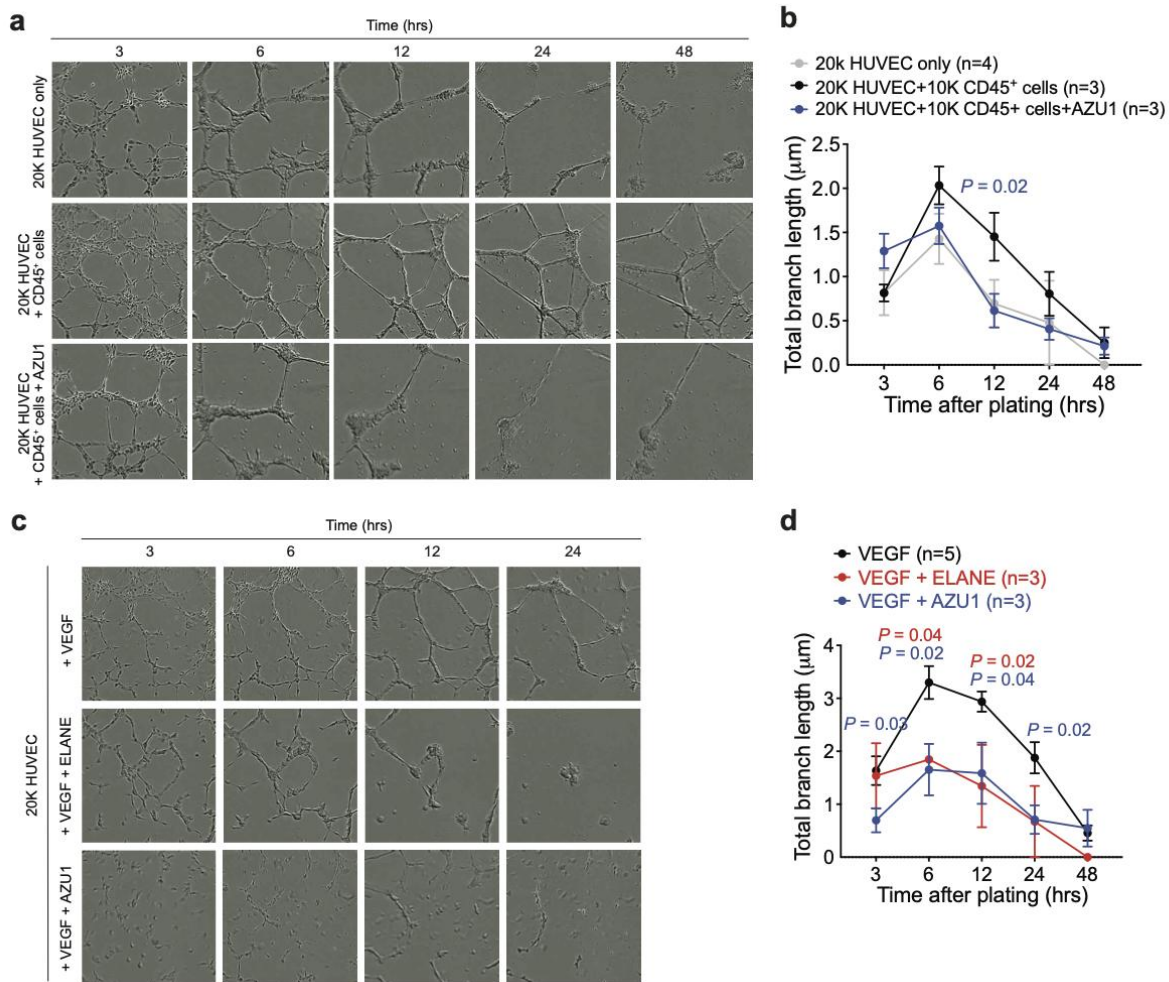microvessels.
(**c**) Images taken with InCucyte S3 Live Imaging Device of HUVEC in Matrigel-based
branching morphogenesis at 3, 6, 12 and 24 hrs after plating. The conditions include
VEGF-primed HUVEC with or without the addition of CXCL16.
(**d**) Quantification of total branch lengths formed by HUVEC under conditions in (**c**).
Not significant comparisons are not shown. *n* indicates the number of independent
biological samples used for quantification. For each biological sample, at least 3
technical replicates are used.
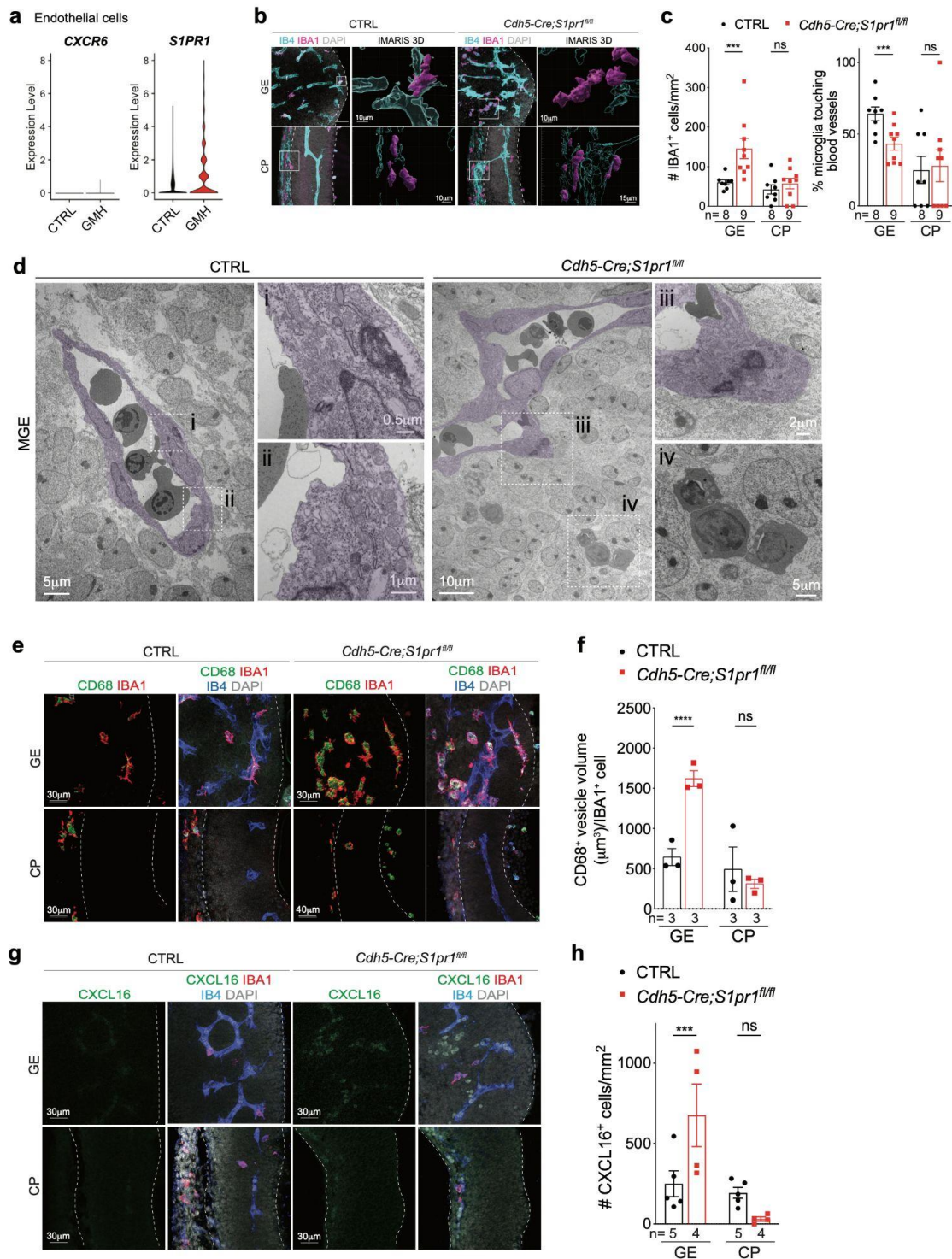
Figure 3.8: CXCL16 putative receptor S1PR1 is required in homeostatic immune-vascular interactions in the GE.
(**a**) Violin plots show the expression of *CXCR6* and *S1PR1* in endothelial cells. (Figure caption continued on the next page.)

(Figure caption continued from the previous page.)

(**b**) Confocal images and IMARIS 3D rendering of IBA1$^+$ cells interacting with IB4$^+$ vasculature in the GE and CP of E12.5 control (CTRL) and *Cdh5-Cre;S1pr1$^{fl/fl}$* mice.

(**c**) Quantification of the density of IBA1$^+$ cells and the percentage of IBA1$^+$ cells touching blood vessels in the GE and CP of E12.5 CTRL and *Cdh5-Cre;S1pr1$^{fl/fl}$* mice.

(**d**) Transmission electron microscopy (TEM) shows myeloid cells inside the vascular lumen and in the brain parenchyma in the medial GE (MGE) of E12.5 CTRL and *Cdh5-Cre;S1pr1$^{fl/fl}$* mice. Insets i-iv show further magnification of TEM images.

(**e-f**) Confocal images and quantification show increased volume of CD68$^+$ vesicles in IBA1$^+$ cells in the GE of *Cdh5-Cre;S1pr1$^{fl/fl}$* mice, compared to age-matched CTRL. Dotted white lines define boundaries of the GE and cortical plate. Only IBA1$^+$ cells within the defined boundaries are quantified.

(**g-h**) Confocal images and quantification show increased density of CXCL16$^+$ cells in the GE of *Cdh5-Cre;S1pr1$^{fl/fl}$* mice, compared to age-matched CTRL.
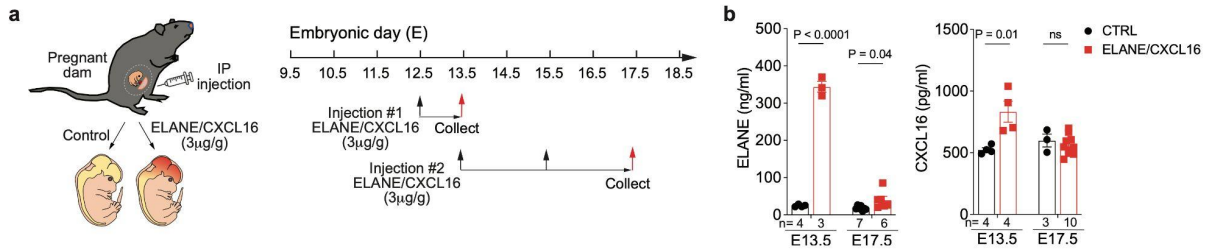
Figure 3.9: Experimental set-up to test the role of ELANE/CXCL16 in GE hemorrhage.
(**a**) Schematic diagram showing two schedules of ELANE and CXCL16 injection in pregnant mouse dams for embryonic brain tissue collection at E13.5 and E17.5.
(**b**) ELANE and CXCL16 protein concentrations in the plasma of control (CTRL) and ELANE/CXCL16-injected pregnant dams.
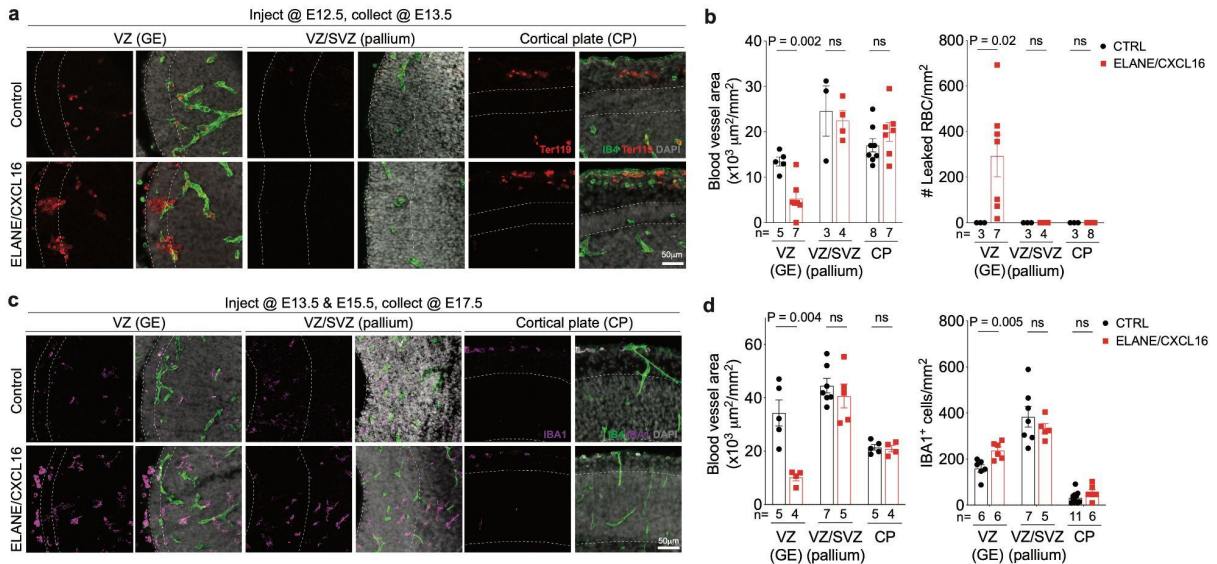
Figure 3.10: Proinflammatory factors ELANE and CXCL16 disrupt nascent vasculature to promote hemorrhage in the embryonic GE.
(**a**) Immunostaining with IB4 and Ter119 show leaked red blood cells in the VZ of GE, but not in the VZ/SVZ of pallium or CP of ELANE/CXCL16-injected embryos at E13.5.
(**b**) Quantification of densities of blood vessels and leaked red blood cells (RBC) in the VZ of GE, VZ/SVZ of pallium, and CP at E13.5.
(**c**) Immunostaining with IB4 and IBA1 show increased density of IBA1+ cells in the VZ of GE, but not in the VZ/SVZ of pallium or CP of ELANE/CXCL16-injected embryos at E17.5.
(**d**) Quantification of densities of blood vessels and IBA1+ cells in the VZ of GE, VZ/SVZ of pallium, and CP at E17.5.
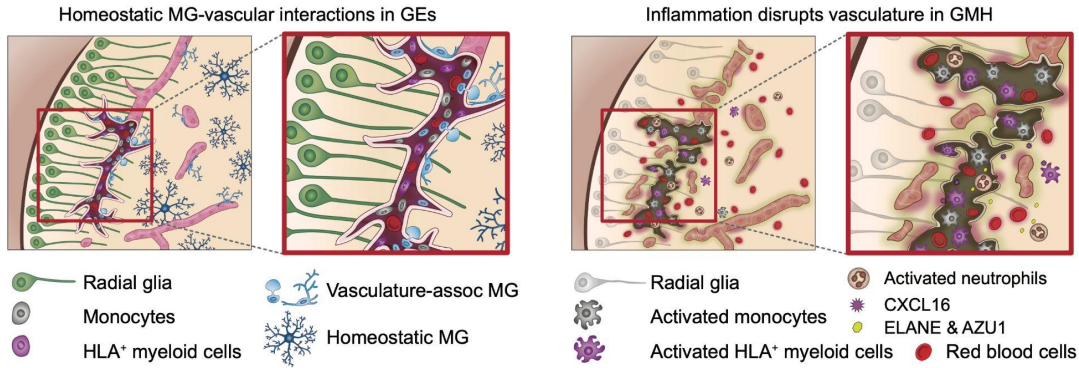
Figure 3.11: Graphic summary for Chapters 2 and 3.
Left: Schematic diagram depicting how subsets of CD45$^+$ immune cells, including monocytes (gray), HLA$^+$ myeloid cells (purple), and vasculature-associated microglia (light blue), interact with the nascent vasculature to promote angiogenesis in the GE. Right: Activated neutrophils produce bactericidal factors, such as ELANE and AZU1, and monocytes produce CXCL16 to create a proinflammatory milieu that disrupts the nascent vasculature and promotes germinal matrix hemorrhage (GMH).
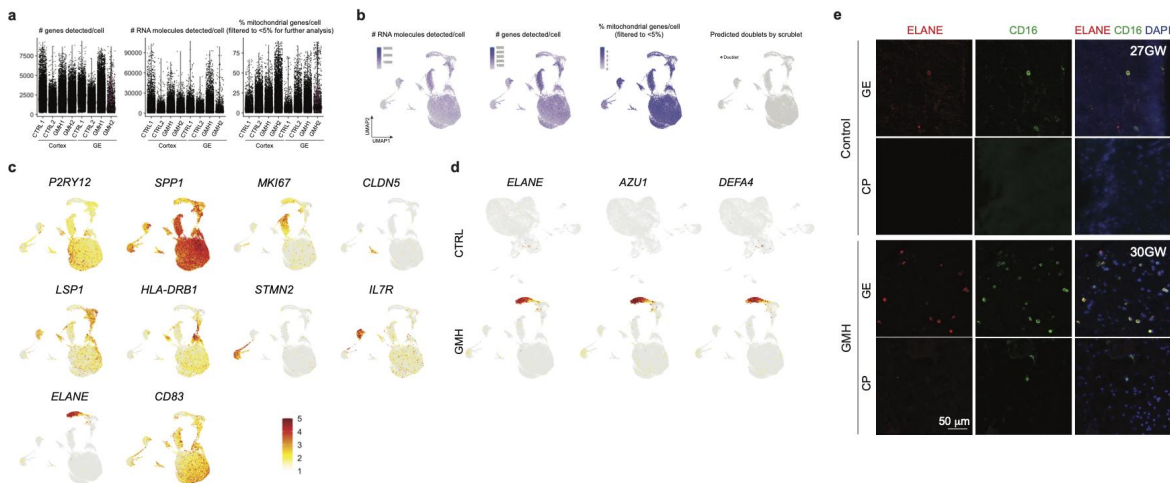
Figure S3.1: Additional scRNA-seq analyses in CD45$^+$ immune cells from control and GMH cases.
(**a-b**) Quantifications of the number of RNA molecules, genes, and percentage of mitochondrial genes per cell, as well as predicted doublets from scRNA-seq in age-matched control (CTRL) and GMH cases.
(**c**) UMAP plots of marker gene expressions that define each subtype of CD45$^+$ cells.
(**d**) UMAP plots of neutrophil transcripts *ELANE*, *AZU1*, and *DEFA4* in CD45$^+$ cells from CTRL and GMH cases.
(**e**) Confocal images show higher abundance of ELANE$^+$ CD16$^+$ cells in the GE of GMH cases compared to age-matched controls.
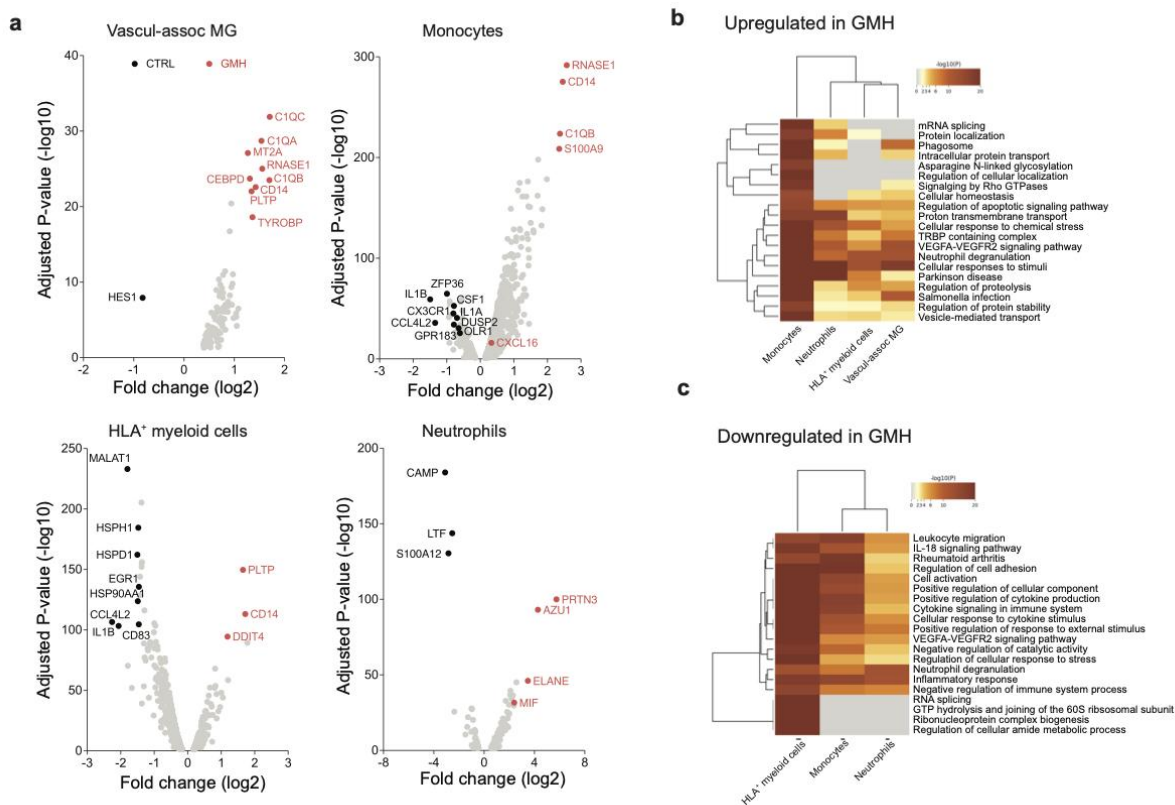
Figure S3.2: Single-cell transcriptomics in CD45⁺ cells from GMH cases reveal widespread inflammation in VAM, monocytes, HLA⁺ myeloid cells, and neutrophils.
(**a**) Volcano plots show differentially expressed genes from GMH *vs* CTRL cases identified by pseudo-bulked scRNA-seq data in CD45⁺ cell subtypes, including vasculature-associated microglia (MG), monocytes, HLA⁺ myeloid cells, and neutrophils. (**b-c**) Heatmap of GO terms in CD45⁺ cell subtypes critical in GE vascular development that are (**b**) upregulated or (**c**) downregulated in GMH cases compared to age-matched controls.
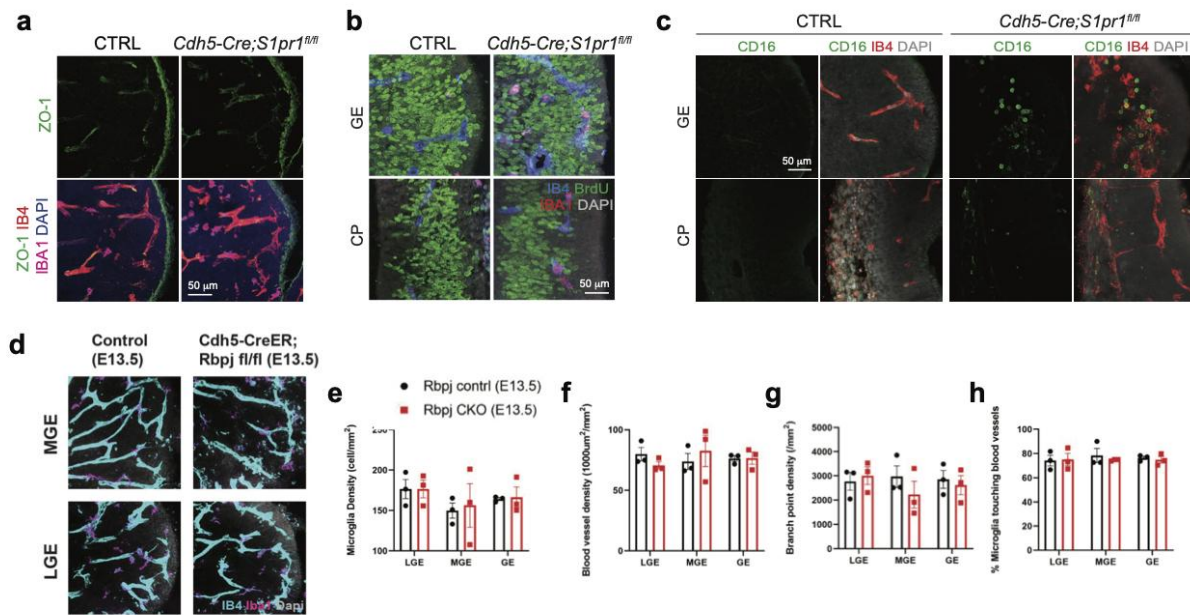
Figure S3.3: Additional analyses on mouse models with endothelial cell-specific knockout of the Notch pathway.

(**a**) Confocal images show expression of adherens junction ZO-1 in the GE of E12.5 control (CTRL) and *Cdh5-Cre;S1pr1$^{fl/fl}$* mice.

(**b**) Confocal images show similar numbers of proliferating BrdU$^+$ cells in the GE and CP of CTRL and *Cdh5-Cre;S1pr1$^{fl/fl}$* mice.

(**c**) Confocal images show higher abundance of CD16$^+$ cells in the GE of E12.5 *Cdh5-Cre;S1pr1$^{fl/fl}$* mice than in age-matched CTRL.

(**d**) Confocal images show minimal changes in IBA1$^+$ cells and IB4$^+$ vasculature in the medial GE (MGE) and lateral GE (LGE) of E12.5 CTRL and *Cdh5-Cre;Rbpj$^{fl/fl}$* mice.

(**e-h**) Quantification of the density of IBA1$^+$ cells, blood vessels, vascular branch points, and percentage of IBA1$^+$ cells touching blood vessels in the LGE, MGE, and combined GEs of E12.5 control and *Cdh5-Cre;Rbpj$^{fl/fl}$* (Rbpj CKO) mice.
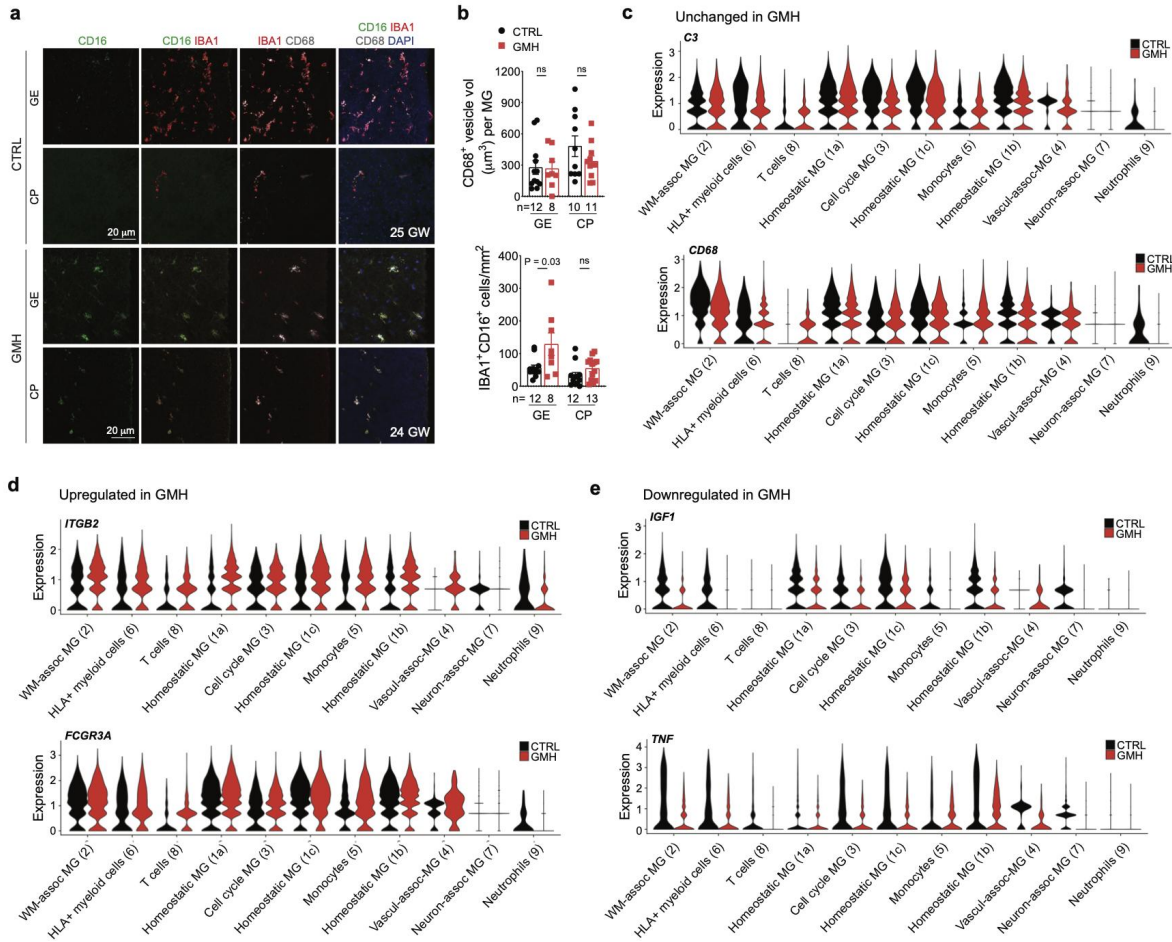
Figure S3.4: Additional analyses on DEGs between control and GMH cases.
(**a-b**) Confocal images and quantification show higher abundance of CD16+ IBA1+ cells in the GE of GMH cases, when compared to age-matched control cases (CTRL). CD68+ vesicle volume in IBA1+ cells remains unchanged between age-matched CTRL and GMH cases.
(**c-e**) Violin plots show (**c**) unchanged, (**d**) upregulated, and (**e**) downregulated expressions of key genes in most CD45+ cell subtypes from GMH cases, when compared to age-matched CTRL.
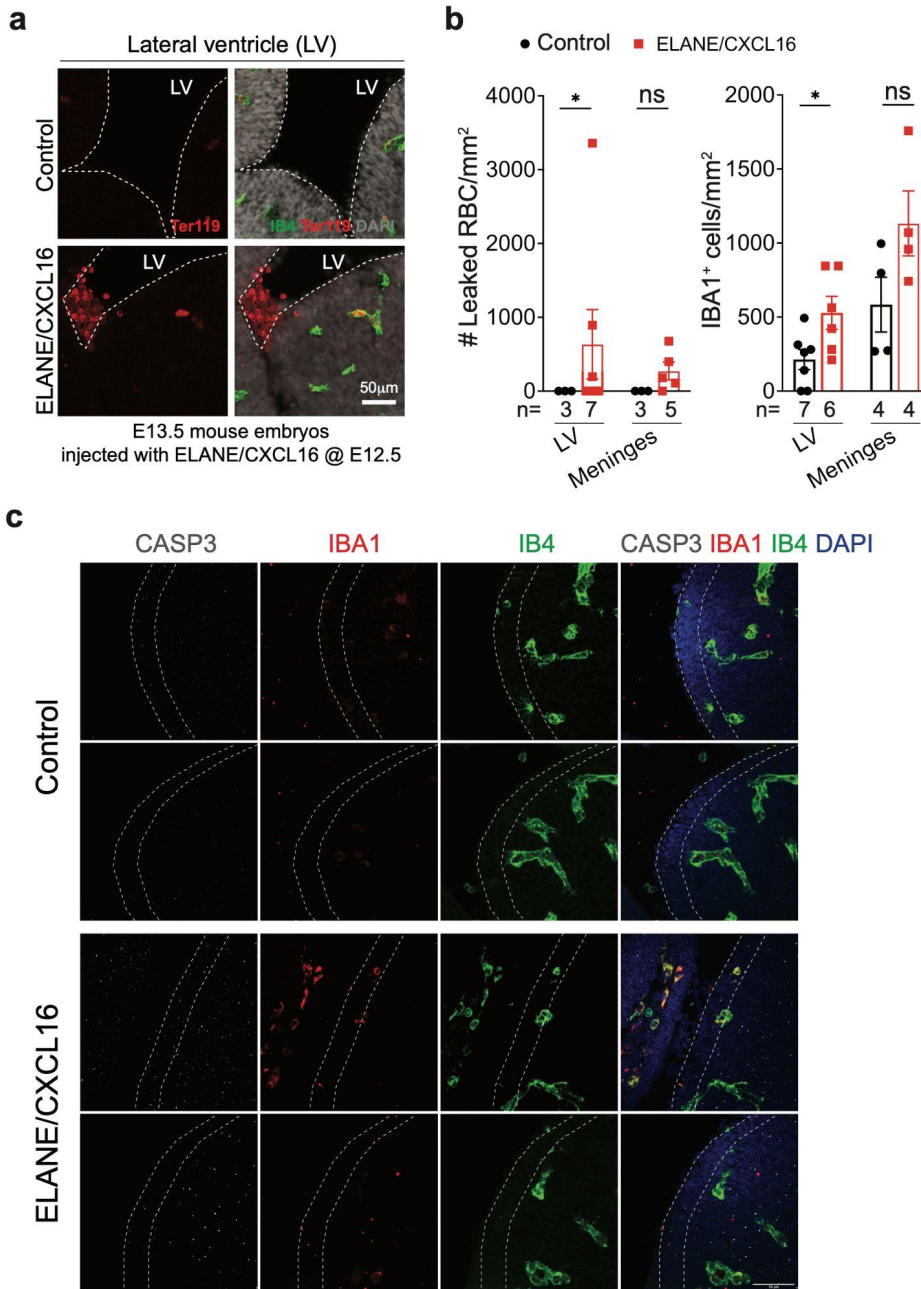
Figure S3.5: Exposure to ELANE/CXCL16 promotes intraventricular hemorrhage in the embryonic mouse brain.

(**a**) Confocal images show intraventricular hemorrhage, characterized by the presence of Ter119^{+} red blood cells (RBC) in the lateral ventricle (LV) adjacent to the MGE.

(**b**) Quantification shows increased numbers of RBC and IBA1^{+} cells in the LV of E13.5 mice injected with ELANE and CXCL16.

(**c**) Confocal images showing cleaved Caspase 3 (CASP3), IBA1, and IB4 in control mice and mice injected with ELANE and CXCL16.
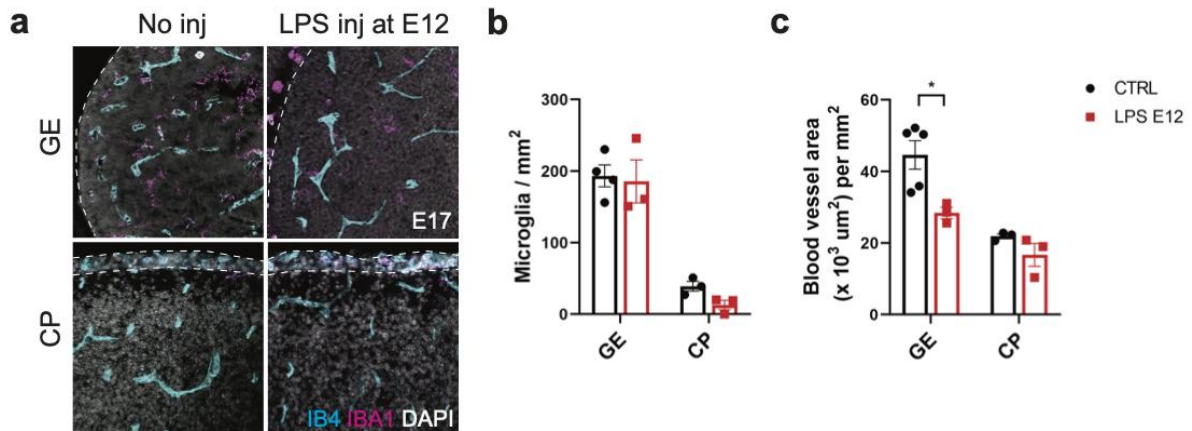
Figure S3.6: Additional maternal immune activation mouse model shows suppressed angiogenesis in the GE.
(**a**) Confocal images of IB4 and IBA1 in E17.5 mouse embryos with no injections or injected with lipopolysaccharide (LPS) at E12.5.
(**b**) Quantification of the density of IBA1+ cells in the GE and CP of E17.5 mouse embryos with no injections (CTRL) or injected with LPS (LPS E12).
(**c**) Quantification of the blood vessel density in the GE and CP of E17.5 mouse embryos with no injections (CTRL) or injected with LPS (LPS E12).

Methods and Materials

Human tissue collection

De-identified age-matched control cases (n=29) and cases with germinal matrix hemorrhage (n=16) of both sexes were collected from the Autopsy Service in the Department of Pathology at the University of California San Francisco (UCSF) and La Fe Biobank with previous patient consent in strict observance of the legal and institutional ethical regulations. The autopsy consent and all protocols for human prenatal brain tissue procurement were approved by the Human Gamete, Embryo and Stem Cell Research Committee (Institutional Review Board GESCR# 10-02693) at the University of California, San Francisco (UCSF) and by the UC San Diego Institutional Review Board (IRB 171379). All cases received diagnostic evaluations by a board-certified neuropathologist to be control or germinal matrix hemorrhage. For immunohistochemistry and RNAscope, tissues were fixed with 4% paraformaldehyde (PFA) for two days, cryoprotected in a 30% sucrose gradient, embedded in OCT, and cut at 30 mm with a Leica cryostat and mounted onto glass slides.

Animals

Mice: All experiments were conducted in accordance with the University of California San Francisco Institutional Animal Care and Use Committee guidelines (IACUC Protocol #AN169548). Mice carrying deletion of exon 5 of the mouse colony stimulating factor 1 receptor gene (Csf1r$^{+/-}$) were obtained from the Jackson Laboratories (B6.Cg-Csf1r$^{tm1.1Jwp}$/J, JAX #028064). Mice containing a fusion product involving simian diphtheria toxin receptor and GFP under the control of the human

ITGAM (integrin alpha M) promoter (CD11b) (CD11b-DTR) were obtained from the

Jackson Laboratories (B6.FVB-Tg(ITGAM-HBEGF/EGFP)34Lan/J). Timed-pregnant

mice (E12.5) were bred using female CD1 animals (Charles River Laboratories) and

male Cx3cr1^{GFP} (B6.129P2(Cg)-Cx3cr1^{tm1Litt}/J, JAX #005582) to visualize macrophages

with GFP in two-photon live imaging. Cdh5-Cre/+;S1pr1$^{fl/fl}$ mice were provided by Dr.

Julieta Alfonso (DKFZ, Germany). For histology, mice were perfused with 4% PFA prior

to extraction of their brains, fixed in 4% PFA for 24 hours, cryoprotected with 30%

sucrose, embedded in OCT, and sectioned at 20 µm coronally with a cryostat and

mounted onto slides.

PLX5622 injections: Colony stimulating factor 1 receptor (CSF1R)-antagonist,

PLX5622 (Plexxikon Inc.) was dissolved in DMSO:PEG400:KolliphorRH40:PBS.

Wild-type pregnant dams were intraperitoneal injected with 250 µl PLX5622 solution (50

mg/kg) daily for seven consecutive days starting at embryonic day (E) 6.5, E10.5 or

E12.5. Mouse embryos were collected one day after the final injection at E13.5, E17.5

or P0 for histological analyses.

Diphtheria toxin (DT) injections: DT was dissolved in PBS and intraperitoneally

injected into CD11b-DTR/+ pregnant mice at 25ng/g (body weight) for two consecutive

days starting at E11.5, E15.5 or E17.5. Mouse embryos were collected one day after the

final injection at E13.5, E17.5 or P0 for histological analyses.

Lipopolysaccharide (LPS) injections: LPS was dissolved in PBS and

intraperitoneally injected into wild-type pregnant mice at E12.5. Mouse embryos were

collected at E17.5 for histological analyses.

Antibodies

Primary antibodies: Mouse anti-CD31 (DAKO, M082329-2, 1:200), Sheep anti-CD31 (R&D Systems, AF806, 1:250), Rabbit anti-IBA1 (FUJIFILM Wako Shibayagi, 019-19741, 1:3000), Goat anti-IBA1 (Novus Biological, NB100-1028, 1:250), Fluorescein labeled isolectin B4 (Vector Laboratories, FL-1201, 1:50), Rabbit anti-ZO-1 (Thermo Fisher Scientific, 40-2200, 1:100), Rat anti-BrdU (Abcam, ab6326, 1:500), Rabbit anti-S100A9 (Abcam, ab63818, 1:500), Mouse anti-HLA DR + DP + DQ (Abcam, ab7856, 1:200), Rabbit anti-ELANE (Abcam, ab131260, 1:1000), Mouse anti-CD16 (Santa Cruz Biotechnology, sc-20052, 1:100), Rat anti-CD68 (Bio-Rad, MCA1957, 1:3000), Goat anti-CXCL16 (Thermo Fisher Scientific, PA5-47977, 1:50), Mouse anti-VE cadherin (Santa Cruz Biotechnology, sc-9989, 1:300), Rabbit anti-Cleaved Caspase-3 (Cell Signaling, 9664, 1:300), Rabbit anti-P2RY12 (Sigma Millipore, HPA014518, 1:200), Rat anti-CD206 (Bio-Rad, MCA2235, 1:200), Mouse anti-CD206 (Abnova, H00004360, 1:200), Rabbit anti-TMEM119 (Abcam, ab209064, 1:300), Mouse anti-VEGFA (Abcam, ab1316, 1:200), Rabbit anti-CD18 (Proteintech, 10554, 1:300), Rat anti-Ter119 (BD Biosciences, 550565, 1:200).

Secondary Antibodies: Donkey anti-mouse Alexa fluor 488 (Thermo Fisher Scientific, A-21202, 1:300), Donkey anti-sheep Alexa fluor 488 (Thermo Fisher Scientific, A-11015, 1:300), Donkey anti-mouse Alexa fluor 568 (Thermo Fisher Scientific, A-10037, 1:300), Donkey anti-rat Alexa fluor 594 (Thermo Fisher Scientific, A-21209, 1:300), Donkey anti-mouse Alexa fluor 647 (Thermo Fisher Scientific, A-31571, 1:300), Donkey anti-rabbit Alexa fluor 647 (Thermo Fisher Scientific, A-31573,

1:300), Donkey anti-goat Alexa fluor 647 (Thermo Fisher Scientific, A-21447, 1:300),

Goat anti-Mouse Alexa fluor 647 (Thermo Fisher Scientific, A-21236, 1:300).

Conjugated Antibodies: Rat anti-LYVE1-eFluor 660 (Thermo Fisher, 50-0443-82,

1:200), Mouse anti-CD45-PECy7 (BD Biosciences, 557748, 1:200), Mouse

anti-CD11b-FITC (Thermo Fisher Scientific, 11-0112-41, 1:200), Mouse

anti-CD16-PerCP Cy5.5 (BD Biosciences, 560717, 1:200), Mouse anti-CD14-APC (BD

Biosciences, 561708, 1:200), Mouse anti-CD141(BDCA-3)-FITC (Miltenyi Biotec,

130-113-321, 1:40), Mouse anti-CD3-BB700 (BD Biosciences, 566575, 1:40), Mouse

anti-CD11b(M1/70)-PE (Invitrogen, 12-0112-82, 1:40), Rat anti-CX3CR1-PE/Dazzle 594

(Biolegend, 341624, 1:20), Mouse anti-CD1c-PE/Cyanine7 (Biolegend, 331516, 1:40),

Mouse anti-CD163-Alexa Fluor 647 (Biolegend, 333620, 1:40), Mouse

anti-CD11c(3.9)-Alexa Fluor 700 (Invitrogen, 56-0116-42, 1:10), Mouse

anti-CD45(HI30)-APC-eFluor 780 (Invitrogen, 47-0459-42, 1:40), Mouse

anti-CD16-Brilliant Violet 421 (Biolegend, 302037, 1:40), Mouse anti-CD31-Brilliant

Violet 605 (Biolegend, 303122, 1:40), Mouse anti-CD15(SSEA-1)-Brilliant Violet 650

(Biolegend, 323034, 1:40), Mouse anti-CD14-Brilliant Violet 711 (Biolegend, 301838,

1:40), Mouse anti-CD19-Brilliant Violet 785 (Biolegend, 302240, 1:40), Mouse

anti-CD20-Brilliant Violet 785 (Biolegend, 302356, 1:40), Mouse anti-HLA-DR-BUV395

(BD Biosciences, 564040, 1:40), Mouse anti-CD64-BUV737 (BD Biosciences, 564425,

1:40), PECy7 Mouse IgG1, κ Isotype Control (BD Biosciences, 557872, 1:200), Alexa

Fluor 488 Mouse IgG2a, κ Isotype Control (BD Biosciences, 557703, 1:200), PECy7

Mouse IgG1, κ Isotype Control (BD Biosciences, 347202, 1:200), APC Mouse IgG1, κ

Isotype Control (BD Biosciences, 555751, 1:200).

Immunohistochemical staining

Chromogenic immunohistochemistry method using 3,3' diaminobenzidine (DAB) was performed on our samples. Slides were equilibrated at room temperature for 2 hours and baked at 60 °C for 30 minutes. Sections were rinsed in TBS and quenched with 10% methanol and 3% H_2O_2 in TBS for 10 minutes. Antigen retrieval was performed using 0.01M sodium citrate buffer (pH 6.0) for 10 minutes at 95 °C. Sections were rinsed three times with TBS and incubated with TBS+ (10% goat serum and 0.2% Triton X-100) blocking buffer for 1 hour, followed by overnight incubation of primary antibodies at RT. Biotinylated secondaries were incubated for 2 hours at RT and rinsed three times with TBS. The VECTASTAIN Elite ABC HRP system with A (Avidin) and B (Biotinylated HRP) complexes in TBS++++ (10% goat serum, 3% BSA, 1% glycine, and 0.4% Triton X-100) was used to amplify staining specificity. Signals were developed in DAB reaction solution (0.05% DAB and 0.05% H_2O_2 in 0.1 M Tris, pH 8.0) and stopped with three washes in 0.1 M Tris (pH 8.0), ending with dehydration in 100% ethanol and counterstaining using Nissl.

Immunofluorescent staining

Tissue-mounted slides were defrosted overnight at 4 °C and then equilibrated to RT for 3 hours. Antigen retrieval was performed on selected antigens with 10 mM sodium citrate buffer (pH 6.0) at 95 °C for 10 minutes. Samples were then washed with TBS for 5 minutes for 3 times, before blocking with TBS++++ for 1 hour. Slides were incubated with primary antibodies with denoted dilutions overnight at RT. Alexa

fluorophore conjugated secondary antibodies diluted in TBS++++ (1:300) were added

on the following day for 2 hours. Slides were then stained with DAPI and coverslipped.

RNAscope

Human-specific probes (*JAML*, *LYZ*, *SLC2A1*, *CLDN5*, *SPP1*, *IGFBP7*, *MFSD2A,*

CXCL16) were obtained from Advanced Cell Diagnostics (ACD). Slides were taken from

-80°C, dried at 60°C for 1 hour, and fixed in 4% PFA for 2 hours. Sections were then

washed with PBS and treated with H_20_2 (ACD) for 10 minutes at RT. All sections were

treated with target retrieval buffer (ACD) for 5 minutes at 98-100°C, before dehydration

with 100% ethanol and baking at 60°C for 30 minutes. Sections were left to dry

overnight at RT. The following day, sections were treated with Protease III (ACD) for 15

minutes at 40°C in the RNAscope Hybridization oven (HybEZ) before probe

hybridization and amplification. All the following steps at 40°C were conducted in the

HybEZ oven. For hybridization, sections were incubated with the desired probes for 2

hours at 40°C, and then rinsed in 1X wash buffer (ACD) twice for 2 minutes each. For

amplification, sections were incubated with Amp 1 (ACD) for 30 minutes at 40°C and

then rinsed twice in the wash buffer for 2 minutes each. This was repeated with Amp 2

(ACD) for 30 minutes and Amp 3 (ACD) for 15 minutes at 40°C, with wash buffer rinsing

between the incubations. HRP-C1 (ACD) was then added for 15 minutes, followed by

Opal Dye (1:100) for 30 minutes, and finally a 15-minute incubation with HRP blocker

(ACD), all performed at 40°C. In between all these steps, sections were rinsed twice for

2 minutes with 1X wash buffer. HRP signal, Opal Dye, and HRP blocker steps were

repeated for C2 and C3 probes. This was followed by the immunofluorescent staining protocol outlined above without the antigen retrieval step.

Tissue clearing and immunofluorescent staining

Samples were optically cleared and immunostained following previously published SHIELD and iDISCO protocols (Park et al., 2018; Renier et al., 2014). 1-2 mm-thick coronal sections were cut from 0.5% PFA-fixed samples and incubated in 25% SHIELD-Buffer Solution and 50% SHIELD-Epoxy Solution (both from Lifecanvas Technologies) at 4°C with gentle shaking for 2 days. This was followed by an incubation with a 1:1 ratio of SHIELD-ON Buffer (Lifecanvas Technologies) and SHIELD-Epoxy Solution at 20 °C with gentle shaking for 1 day. Sections were then passively cleared with an SDS-based solution (300 mM sodium dodecyl sulfate, 10 mM boric acid, 100 mM sodium sulfite titrated to pH 9) at 55-60 °C with gentle shaking until tissue was transparent. After clearing, samples were immunostained following iDISCO-based steps. Briefly, sections were incubated in permeabilization solution (20% DMSO, 0.16% Triton X-100, and 23 mg/ml glycine in PBS) and then blocking solution (10% DMSO, 5% donkey serum, and 0.168% Triton X-100 in PBS) at 37 °C for 2 days in each solution. Sections were then incubated with primary antibodies in PTwH (0.2% Tween-20 and 0.01 mg/ml heparin in PBS) with 5% DMSO and 3% donkey serum, and secondary antibodies in PTwH with 3% donkey serum at 37 °C for 7 days in each antibody step with gentle shaking. Sections were washed in PTwH at RT for a day between the two antibody incubation steps. Finally, sections were refractive index (RI)-matched in EasyIndex (Lifecanvas Technologies) overnight at RT before imaging.

Agarose embedding and light-sheet Imaging

Refractive index-matched sections were embedded in 1.8% low melting-point agarose (Thermo Fisher) and emerged in EasyIndex (Lifecanvas Technologies) on custom made sample holders. Samples were imaged using an axially swept light-sheet microscope (SmartSPIM, Lifecanvas Technologies) equipped with a 3.6X, NA 0.2 objective (uniform axial resolution 3.2-4.0 mm) and a 2048 x 2048 sCMOS camera.

Confocal imaging, processing and quantifications

Confocal images were acquired on a Leica TCS SP8 confocal microscope using a 63x (NA 1.4) objective. Images used for quantifications were taken within 300 µm of the lateral ventricle or the meninges, and with a thickness of 1 µm for each z step. Images were processed and quantified using ImageJ (v2.0.0-rc-69/1.52i). 3D rendering of vascular surfaces and microglia were generated using IMARIS (v9.8).

Two-Photon Live Imaging of Embryonic Lateral Ganglionic Eminence

Timed-pregnant mice (E12.5) were bred using female CD1 animals (CRL) and male $Cx3cr1^{GFP}$ (B6.129P2(Cg)-$Cx3cr1^{tm1Litt}$/J, Jax Stock #005582) to visualize macrophages using GFP and to maximize litter size. Dams were anesthetized with ketamine/xylazine (60-120 mg/kg and 5-10 mg/kg, respectively, intraperitoneal) and placed on a heating pad. A laparotomy was performed, and embryos were gently exposed. Vasculature labeling was achieved by placental injection of ~7.5 µl of 25 mg/ml Texas Red-Dextran (70 kD, ThermoFisher Scientific). Following a 10 minute wait to allow the dextran to circulate, the samples with the placenta attached were

transferred to an imaging chamber filled with artificial CSF (aCSF) at 37°C (CSHL

formulation: https://cshprotocols.cshlp.org/content/2011/9/pdb.rec065730.full, 119 mM

NaCl, 2.5 mM KCL, 1 mM NaH_2PO_4, 26.2 mM $NaHCO_3$, 1.3 mM $MgCl_2$, 2.5 mM $CaCl_2$,

modified glucose amount to 35 mM glucose). The developing skull and cerebral cortex

were removed, exposing the lateral ventricle and LGE. Oxygenated (95/5 O_2/CO_2) and

warmed aCSF was continuously circulated in the imaging chamber.

Two-photon imaging of immune cells was performed using either

resonant-scanning (512 × 512 pixels/frame, 8.1 frames/s) or Galvo-scanning

(1024x1024 pixels/frame, 1.3 frames/s) with a two-photon microscope (Olympus

MPE-RS Multiphoton Microscope) and a 25X objective (Olympus XLSLPLN25XSVMP2,

0.95 NA, 8 mm W.D.), varying from 1x to 3x zoom. Recordings were between 15-30

minutes in duration. Volume scanning was achieved using a piezoelectric scanner

(nPFocus250). Laser power at 920 nm (Mai Tai DeepSee laser, Spectra Physics)

measured below the objective was 30-70mW. Resonant-scanning acquisitions were

processed and registered using previously published code (Shipley et al., 2020).

Galvo-scanning acquisitions were processed using previously published Fiji registration

plugins (Preibisch et al., 2010).

Transmission and immuno-gold electron microscopy

For transmission electron microscopy (TEM), mouse embryos were fixed in 3%

glutaraldehyde and 1% paraformaldehyde in 0.1 M sodium cacodylate buffer (pH 7.4)

overnight. Following fixation, the tissues were processed through 2% osmium tetroxide

and 4% uranyl acetate, then dehydrated and embedded in Eponate 12 resin (Ted Pella

Inc.). Ultrathin sections were sectioned at 70 nm thick, collected on copper grids, and imaged in a Phillips Tecnai10 transmission electron microscope using FEI software. For IBA1^{+} immuno-gold electron microscopy, human prenatal brains at 21 GW were fixed in 4% paraformaldehyde for 7 days and then were cut into 0.5 cm coronal blocks. After selecting the region of interest, 100 mm sections were obtained with a vibratome (Leica VT-1000 S). Pre-embedding immunogold staining was performed by incubating sections in 1:150 primary antibody rabbit anti-Iba1 (WAKO) and in goat anti-rabbit colloidal gold-conjugated secondary antibody (1:50; UltraSmall; Aurion, Wageningen, The Netherlands) as described previously (Sirerol-Piquer et al., 2012). Then the slices with the immunogold staining were post-fixed with 1% osmium tetroxide with 7% glucose for 30 min, rinsed, dehydrated and embedded in araldite (Durcupan; Fluka, Buchs, Switzerland). Semithin sections (1.5 mm) were cut with an Ultracut UC-6 (Leica, Heidelberg, Germany), mounted on gelatin-coated slides and stained with 1% toluidine blue. These sections were examined under a light microscope (Eclipse E200, Nikon). To identify cell types, ultrathin sections (70nm) were cut, stained with lead citrate (Reynolds solution) and examined under a transmission electron microscope (Tecnai Spirit G2; FEI, Eindhoven, The Netherlands). Images were acquired using Radius software (Version 2.1) with a XAROSA digital camera (EMSIS GmbH, Münster, Germany).

In vitro cultures, angiogenesis assays, and live imaging

Human umbilical vein endothelial cells (HUVEC; ATCC) were cultured at 37°C and 5% CO_2 in EGM™-2 Endothelial Cell Growth Medium-2 BulletKit™ (EGM-2; Lonza) with the following supplements: fetal bovine serum, human recombinant epidermal

growth factor (EGF), hFGF-B, R3-IGF-1 (5 ng/ml), VEGF (2 ng/ml), hydrocortisone, ascorbic acid, GA-1000, and heparin. Only HUVECs between passages 2 and 6 were used in experiments. For *in vitro* angiogenesis assays, 96-well plates were coated with undiluted Matrigel (Growth Factor Reduced Basement Membrane Matrix, Corning) and seeded with HUVECs in EGM-2. At the same time, 10,000 or 20,000 CD45$^+$ cells were added to each well for evaluating the role of immune cells in angiogenesis. Same densities of CD45$^-$ cells were used as controls. In experiments where CD45$^+$ cells were labeled, cells were transfected with AAV-CMV-GFP (Vector Biolabs) at 200 MOI and incubated at 37 °C for 30 minutes, before washing with PBS. In assays with recombinant proteins, the following concentrations were added: 25 ng/ml VEGF (R&D Systems), 5 ng/ml IGF-1 (PeproTech), 5 µg/ml ELANE (R&D Systems), 20 µg/ml AZU1 (R&D Systems), and 10 µg/ml CXCL16 (R&D Systems). From 0 to 48 hours, vascular tube formations were imaged every 5-10 minutes using a 4x objective on Incucyte S3 Live-Cell Analysis Systems (Essen BioScience, Inc.).

Microvessel fabrication, vascular permeability measurement, and IF staining

Human dermal microvascular endothelial cells (hMVEC-Ds, Lonza) were maintained in EGM2-MV growth medium (Lonza) and used at passages 2-7. Cells were maintained at 37 °C in 5% CO_2 in a humidified incubator. Cell-line authentication (performance, differentiation, and STR profiling) was provided by Lonza. Mycoplasma testing was performed on cells using Mycoplasma PCR Detection Kit (Applied Biological Materials Inc.). Microvessels were fabricated as previously described (Polacheck et al., 2019). Briefly, microfluidic devices were made using soft lithography. Polydimethyl-

siloxane (PDMS, Sylgard 184, Dow-Corning) was mixed at a ratio of 10:1 (base:curing agent) and cured overnight at 60 °C on a silicon master. PDMS was then cut from the silicon master, trimmed, and surface-activated by plasma treatment for 30 seconds. Devices were then bonded to glass and treated with 0.01% poly-L-lysine for 2 hours, washed 3 times with water, treated with 1% glutaraldehyde for 15 minutes, washed 3 times with water, and sterilized with 70% ethanol for 1 hour. Steel acupuncture needles (160 µm diameter, Tai Chi) were sonicated in 70% ethanol for 3 minutes and introduced into each sterile device. Assembled devices were dried in a vacuum desiccant chamber for at least 30 minutes. Collagen type I (Corning) solution in 10x DMEM and 10x reconstitution buffer (0.26 M NaHCO3 and 0.2 M HEPES) was titrated to pH 8.0 with 1M NaOH to make a final concentration of 2.8 mg/ml collagen I. The collagen solution was then injected into the microfluidic devices and polymerized for 15 minutes at 37°C. Sterile PBS was added to the devices overnight, then the needles were removed to create 160 µm-diameter channels in the collagen gel. Growth medium was then added to the devices for at least 30 minutes prior to cell seeding. hMVECs were harvested with 0.05% Trypsin-EDTA and centrifuged at 200 x g for 3 minutes. Cells were resuspended at 1×10^6 cells/ml in EGM2-MV, 50 µl of cell suspension was introduced into the devices and cells were allowed to adhere to collagen for 15 minutes before washing with growth medium. Devices were cultured on a lab rocker (Variable Speed Rocker, VWR) to induce oscillatory shear stress (2 rpm, 30° tilt angle). Media was changed every 24 hours. Two days after seeding, devices were given EGM2-MV media which contained either 20 µg/ml CXCL16 (R&D Systems) and 20 µg/ml activated ELANE (R&D Systems), or 100 µg/ml AZU1 (R&D Systems).

Vascular permeability was quantified as previously described (Polachek et al., 2019). Briefly, 25 µg/ml fluorescent dextran (Fluorescein isothiocyanate dextran 70 kDa, Sigma Aldrich) was introduced into the perfusion medium, and dextran diffusion was imaged in real time with a Yokogawa CSU-X1 inverted spinning-disk Nikon Ti-E confocal microscope with a 10x air objective, 488 nm solid-state laser, and a high-resolution interline CCD (cMyo, Photometrics). Time-lapse microscopy was used to measure the flux of dextran into collagen gel. Using MATLAB, the resulting diffusion profile was fitted to a dynamic mass-conservation equation, with the diffusive-permeability coefficient (P_D) defined by $J = P_D(c_{vessel} - c_{ECM})$, where J is mass flux of dextran, c_{vessel} is concentration of dextran in the vessel, and c_{ECM} is concentration of dextran in perivascular ECM.

Devices were fixed immediately after barrier function measurements with 4% paraformaldehyde in PBS with calcium and magnesium at 37°C for 15 minutes. Devices were rinsed three times with PBS and fixative was quenched with 100mM glycine for 30 minutes. Devices were permeabilized with 0.25% Triton X-100 in PBS for 10 minutes and blocked with 2% bovine serum albumin (BSA) in PBS for 1 hour. Primary and secondary antibodies were applied in 2% BSA in PBS for 1 hour each and were rinsed with PBS for 30 minutes between each incubation. Immunostained devices were imaged using a 20x air objective on either a Yokogawa CSU-W1 SoRA spinning disk confocal on a Nikon Ti-2 microscope with a sCMOS camera (ORCA-Fusion BT, Hamamatsu Photonics), or a CSU-10 spinning disk confocal on a Nikon Ti-E microscope with a CoolSnap HQ2 cooled charge-coupled camera (Photometrics).

Fluorescence-activated cell sorting (FACS) & high-dimensional flow cytometry

To isolate immune cells from prenatal human brain tissues, we adapted a previously published protocol (Crouch et al., 2022). Briefly, brain tissue was minced with a scalpel and digested with collagenase/dispase (3 mg/ml, Sigma) for 30 min at 37 °C with rotation, triturated in 2% FBS in PBS with DNase (0.25 mg/ml), and centrifuged through 22% Percoll (Sigma) to remove debris. Cells were then stained with AO/PI cell viability dye and counted with the Cellaca MX High-throughput Automated Cell Counter (Nexelcom). Approximately 3 million cells were aliquoted from each sample into a 96 v-well plate (Corning), and incubated with Zombie Aqua Fixable Viability Dye (Thermo) for 20 minutes on ice and in the dark. After viability dye incubation, cells were washed with sort buffer (PBS/2% FCS/2mM EDTA) and incubated with Human Fcx (Biolegend) to block non-specific antibody binding. Cells were then washed with sort buffer and incubated with cell surface antibody mix diluted in BV stain buffer (BD Biosciences) for 30 minutes on ice and in the dark. Following antibody staining, cells were washed twice with sort buffer. Cells were then resuspended in Fixation Buffer (BD Bioscience) for 20 minutes on ice and in the dark. Flow cytometry data were acquired using FACS Diva software v.7 (BD) and the data obtained were analyzed using FlowJo v10.8.2 (LLC).

In vitro angiogenesis assay and RNA sequencing

Following Percoll centrifuge, samples were incubated on ice for 15 min with PECy7-conjugated mouse anti-hCD45 (1:200, BD Biosciences). After washing, samples were resuspended in HBSS buffer with DAPI (1:500, Thermo Fisher) to exclude dead cells. Cells were sorted using Becton Dickinson FACSAria with 13 psi pressure and 100

µm nozzle aperture. All FACS gates were set using unlabeled cells, single-color and isotype controls from human samples. FACS-processed cells were immediately used for scRNA-seq or angiogenesis assays. FACS graphs were made with FlowJo (v10.6.2).

Bulk RNA sequencing, analysis, and GSEA

For each sample, RNA was extracted from 1,000 cells and loaded as input for cDNA amplification. cDNA concentration was measured with NanoDrop and diluted to 0.4 ng/µL. Libraries were constructed using Takara SMART-seq (v4) and Illumina Nextera XT following the manufacturer's instructions. Library pools were quality-controlled and normalized using Illumina MiniSeq before pair-ended (100-bp reads) sequencing with Illumina HiSeq4000. Finally, reads were aligned to hg38 using STAR (v2.7.2.b). EdgeR (version 3.34.1) in R software was used to normalize raw counts and perform differential gene expression analyses. In addition, DESeq2 (version 1.32.0) was used to generate heatmaps with variance stabilizing transformation (vst). Gene set enrichment analysis (GSEA) was performed with biological pathways in Gene ontology (c5.go.bp) from MSigDB (https://www.gsea-msigdb.org/gsea/msigdb/).

Single-cell RNA sequencing (scRNA-seq)

Sample preparation: Cells after FACS were processed with Single Cell 3' v3 and v3.1 kits (10X Genomics) following manufacturer's instructions. In each sample, 10,000 cells were targeted for capture and 12 cycles of thermal cycling were used for cDNA amplification and library amplification. Libraries were sequenced as per manufacturer recommendation on a NovaSeq S2 flow cell.

scRNA-seq data processing, UMAP visualization, and clustering: Gene counts were obtained by aligning reads to the hg38 genome (refdata-gex-GRCh38-2020- A) using CellRanger (v.3.1.0) (10x Genomics). Only high-quality cells were included for further analysis with the following criteria: number of genes per cell between 200 and 6000, number of RNA molecules per cell less than 40000, and mitochondrial RNAs per cell less than 5%. Doublets were checked with Scrublet, which predicted that minimal doublets were present in the dataset after filtering. After applying these quality control steps, control samples yielded 56,314 cells and germinal matrix hemorrhage (GMH) samples yielded 17,187 cells. After filtering, the dataset was first batch corrected by sample using SCTransform from Seurat (version 4.1.0). UMAP was then used to project the dataset into two-dimensional space with the top 30 principal components. Clustering was performed with the Louvain-Jaccard method and top expressed genes in more than 50% of cells in each cluster were designated as marker genes.

scRNA-seq cell type annotation, differential gene expression, and gene ontology (GO) analysis: Cell types were annotated based on UMAP reduction and gene marker analysis using Seurat's FindAllMarkers function. Genes expressed in >50% of cells in each cluster with log fold change >1.52 were selected as cell type markers. For pseudo-bulk differential expression analysis between control CD45^{+} cells from the GE and the cortex, as well as between CD45^{+} cells from control and GMH cases, we used Seurat's DESeq2 function. For GO analysis, we used Metascape to perform statistical overrepresentation tests for differentially expressed genes in each condition. GO Biological Processes were chosen to represent enriched functional properties. Processes with false discovery rate (FDR) <0.05 were considered to be significant.

scRNAseq integration with published scRNAseq data: Published or shared scRNA-seq data were projected onto UMAP plots of our dataset using ProjecTILs according to its instructions (Andreatta et al., 2021). Mouse genes were converted to human ortholog genes using Ensembl accordingly.

scRNAseq ligand-receptor matching (CellphoneDB and NicheNet): For inputs into CellphoneDB (v2), normalized counts and their cell type information were exported from Seurat. Only ligands and receptors expressed in more than 25% of cells in each cluster were considered. 3000 cells were sub-sampled to produce the heatmaps due to limited computational power, but they should accurately reflect the interaction frequencies between cell types. For NicheNet (v1.1.0) (Browaeys et al., 2020), previously defined Seurat objects with their cell type information were used as inputs. Only ligands and receptors expressed in more than 20% of CD45$^+$ cells or endothelial cells were considered. Only the top 200 differentially expressed target genes in > 10% of the receiver cell type (i.e. endothelial cells) were used for downstream analysis. Ligands from sender cells (i.e. CD45$^+$ cells) that were predicted to differentially regulate target gene expression in receiver cells were filtered to only include those that were enriched in either the GE or in GMH cases. Both width and transparency of arrows in circularized plots indicate interaction strengths between predicted ligand-receptor pairs.

Statistical Analyses

For all statistical analysis, a P value less than 0.05 was considered significant. * indicates $P < 0.05$, ** $P < 0.01$, *** $P < 0.005$, **** $P < 0.001$, ns, not significant. Data represents mean ± SEM. The exact numbers of samples, including images and

biological replicates, are indicated in the figure legends. Statistical analyses were done using Prism 10 (GraphPad). For comparisons between two groups, if normally distributed, two-tailed unpaired Student's *t* tests were performed.

Acknowledgements

Author Contributions

J.C. and E.J.H. conceived the project, designed the experiments, interpreted the results, and wrote the manuscript with inputs from all authors. J.C. performed immunohistochemistry and immunofluorescence microscopy with assistance from J.J.C. J.C. performed quantification of blood vessel and microglial densities, HUVEC cell culture experiments and quantification, bulk and scRNA-seq on CD45$^+$ cells, and bioinformatics analyses of the RNA-seq data, including gene ontology (GO), GSEA, CellPhone DB, and NicheNet. E.E.C., L.N.D., K.W-P., E.J.V., J.O.B. and J.C. performed FACS experiments for CD45$^+$ cells from prenatal human brain. M.E.Z. performed live imaging of *Cx3cr1$^{+/GFP}$* cells in E12.5 embryos with supervision from M.K.L., K.J. and L.M. performed experiments using microfluidic device-based vascular channels with supervision from M.L.K., S.S., J.C., J.T. performed high-dimensional flow cytometry with supervision from A.J.C. S.G-G. performed IBA1 IEM with supervision and interpretations from J.M.G-V. S.W. and A.K. contributed to the collection of prenatal human brain tissues and performed and analyzed histopathology data from control and GMH cases. B. Di M., W.X., S.P.J.F., and J.A. contributed *Gpr124* and *S1pr1* mutant mice, and C.Z.H., N.G.C., and C.K.G. contributed scRNA-seq data from 12-14 GW prenatal human brain.

Chapter 4: Role of microglia in neuronal development in the prenatal brain

Introduction

Microglia play a crucial role in supporting the proliferation of cortical neural progenitor cells (NPCs) and ensuring the survival of neurons in the developing brain. Microglia selectively populate cortical proliferative zones and establish preferential connections with actively dividing NPCs (Noctor et al., 2001; Anthony et al., 2011; Cunningham et al., 2013; Barger et al., 2018). While interacting with NPCs, microglia secrete various cytokines such as IL-1β, IL-6, TNFα, and IFNγ to regulate their cell divisions (Shigemoto-Mogami et al., 2014). Moreover, microglia contribute to postnatal brain development by releasing neurotrophic factors like IGF-1, which support the survival of layer V neurons (Ueno et al., 2013).

In addition to their role in NPC maintenance, microglia are instrumental in guiding neuronal migration to the cortex. Disruptions in microglia activity lead to premature entry and abnormal distribution of interneurons in the embryonic cortical plate (Squarzoni et al., 2014). Conversely, microglia also phagocytose and cause the cell death of neural progenitors, influencing the size of neuronal pool (Cunningham et al., 2013; Barger et al., 2018; Marin-Teva et al., 2004). The intricate balance maintained by microglia in regulating various aspects of neurodevelopment, including proliferation, migration, and apoptosis of neurons and their progenitors, presents a complex puzzle that needs further investigation, particularly in understanding microglia heterogeneity and their interactions with distinct neuronal types in different brain regions.

Here, we show that IBA1$^+$ cells primarily interact with radial glia, avoiding DCX$^+$ young neurons in the GE. A negative correlation with an increase in IBA1$^+$ cell density

and a decrease in radial glia and proliferating cell densities hints at a potential role of microglia/macrophages in pruning NPCs. Indeed, depletion of microglia/macrophages in mouse embryos results in elevated radial glia density at E17.5 in the GE. Additionally, microglia/macrophage depletion leads to abnormal patterning of proliferating NPCs. Finally, transplantation of human immune cells into neural organoids highlights their activated morphology near SOX2$^+$ cells, suggesting potential roles in pruning human NPCs by microglia and macrophages.

Results

Microglia/macrophage density negatively correlates with neural progenitor density

To characterize the interaction between microglia/macrophages and neural progenitors in the prenatal human brain, we studied the relationship of IBA1$^+$ cells with SOX2$^+$ NPCs in the GE (**Fig. 4.1a**). While abundant IBA1$^+$ cells were found in proliferative regions enriched with SOX2$^+$ NPCs, they were often not co-localized with NPCs. Further investigations using radial glia marker Nestin and young neuron marker doublecortin (DCX) showed that IBA1$^+$ cells preferentially interacted with radial glia and avoided DCX$^+$ clusters in the MGE (**Fig. 4.1b-c**). While the density of IBA1$^+$ cells increased with age up to 30 GW in the GE, densities of radial glia and proliferating NPCs (Ki67$^+$ SOX2$^+$) dropped (**Fig. 4.1d-f**). This negative correlation between densities of IBA1$^+$ cells and NPCs suggested a potential role of microglia/macrophages in pruning NPCs. Indeed, immunostaining using cleaved caspase-3 showed that IBA1$^+$ cells could engulf apoptotic fragments in the MGE and LGE at 17 and 24 GW (**Fig. 4.1g**).

We next asked whether similar interactions between IBA1$^+$ cells and Nestin$^+$ radial glia could be observed in the embryonic mouse brain. Consistent with our results in the prenatal human brain, IBA1$^+$ microglia/macrophages preferentially interacted with radial glia fibers, and not with DCX$^+$ neurons (**Fig. 4.2a**). Intriguingly, we also found a negative correlation between densities of IBA1$^+$ cells and radial glia, proliferating cells, or PH3$^+$ mitotic cells, particularly between E15.5 and E17.5 (**Fig. 4.2b-d**). Taken together, IBA1$^+$ microglia/macrophages were found in abundance within the proliferative zones enriched in radial glia, and their negative correlation with the density of NPCs suggest a role in pruning the neural progenitor and proliferating cell population.

Microglia/macrophage prune radial glia and ensure accurate positioning of neural progenitors in the embryonic GE

To test whether IBA1$^+$ cells negatively regulated the NPC population, we used multiple mouse models to examine the effects of microglia/macrophage depletion on radial glia density. Compared to control embryos with no injection, embryos injected with CSF1R inhibitor PLX5622 contained significantly higher radial glia density at E17.5 in the GE, but not at E13.5 or in the cortical plate (**Fig. 4.3a-b**). Similarly, microglia/macrophage depletion in *Csf1r*$^{-/-}$ embryos led to a much higher radial glia density at E17.5 in the GE, but not at E13.5 or in the cortical plate (**Fig. 4.3c**). Intriguingly, *Csf1r*$^{+/-}$ embryos did not exhibit changes in radial glia density. On the other hand, when microglia were activated with LPS injection at E12.5, radial glia density also increased in the GE at E17.5 when compared with age-matched embryos with no injection (**Fig. 4.3d**). Collectively, these findings suggested that an altered state of

microglia contributed to increased radial glia density, underscoring the crucial role of microglia/macrophages in negatively modulating the radial glia population.

Furthermore, we explored the effects of microglia/macrophage depletion on neural progenitor positioning in the embryonic GE. Using both PLX5622-injected embryos and DT-induced CD11b-DTR embryos, we demonstrated that there was not only a higher density of PH3$^+$ mitotic cells in microglia-depleted embryos, but also an abnormal patterning of these mitotic cells in the GE at E13.5 and E17.5 (**Fig. 4.4a-b**). Similarly, the positionings of Ki67$^+$ proliferating cells, SOX2$^+$ or MASH1$^+$ NPCs, and OLIG2$^+$ oligodendrocyte progenitors were dysregulated in microglia-depleted embryos at E13.5, E17.5, and P0 (**Fig. 4.4c-e**). These results highlighted the additional role of microglia and macrophages in regulating neural progenitor migration within the GE.

Transplantation of microglia/macrophages into neural organoids

In our attempt to study the effects of IBA1$^+$ cells on human NPCs, we transplanted FACS-isolated and AAV-CMV-GFP-transfected CD45$^+$ CD11b$^+$ cells from second trimester human brains into 8-week old neural organoids that contained rosettes of SOX2$^+$ NPCs (**Fig. 4.5a**). Instead of the ramified morphology of resting microglia, these amoeboid IBA1$^+$ cells adopted an activated morphology near SOX2$^+$ cell clusters. Three weeks after transplantation, the density of these immune cells remained relatively similar across ages, except for at 18 GW, when both the density of IBA1$^+$ cells and their transfection efficiency by AAV-CMV-GFP peaked (**Fig. 4.5b**). This suggested potentially more proliferative IBA1$^+$ cells at 18 GW. Together, it seemed like microglia and

macrophages could adopt a phagocytic-like morphology near human NPCs in organoids. However, these results remain preliminary and warrant further investigation.

Discussion

To explore the interaction between microglia/macrophages and neural progenitors in the prenatal brain, we first show that IBA1$^+$ cells predominantly interact with radial glia, avoiding DCX$^+$ young neurons in the GE (**Fig. 4.1-2**). Additionally, the density of IBA1$^+$ cells increases while radial glia and proliferating NPC densities decrease, indicating a negative correlation. This suggests a potential role of microglia/macrophages in pruning NPCs, supported by immunostaining showing IBA1$^+$ cells engulfing apoptotic fragments in the human GE (**Fig. 4.1g**).

To investigate the negative regulation of NPC population by IBA1$^+$ cells, we use various mouse models to modulate microglia/macrophage states. These models show that either depletion or activation of microglia/macrophages in mouse embryos results in elevated radial glia density at E17.5 in the GE (**Fig. 4.3**). Moreover, microglia/macrophage depletion also leads to abnormal patterning of proliferating cells and NPCs in the GE (**Fig. 4.4**). Together, these results indicate that microglia/macrophages are involved in negatively modulating the radial glia population, as well as regulating the migration of neural progenitors.

To study the effects of microglia/macrophages on human NPCs, CD45$^+$ CD11b$^+$ cells from second-trimester human brains are transplanted into neural organoids (**Fig. 4.5**). These transplanted immune cells, adopting an activated morphology, remain near SOX2$^+$ cell clusters. However, further investigation is needed to understand the implication of these findings.
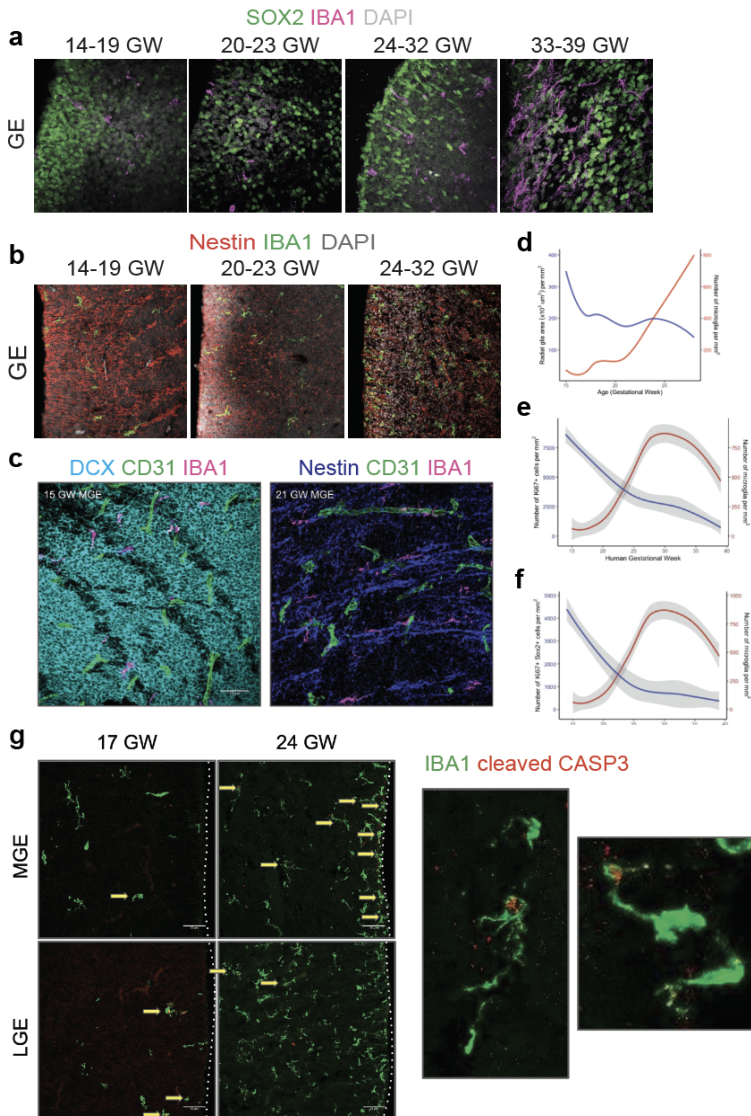
Figure 4.1: IBA1+ cell density negatively correlates with densities of radial glia, neural progenitors, and proliferating cells in the prenatal human GE.

(**a-c**) Confocal images show abundant IBA1+ cells in neurogenic niches in the human GE enriched with (**a**) SOX2+ neural progenitors, (**b, c**) Nestin+ radial glia, and (**c**) DCX+ young neurons.

(**d-f**) Quantifications show that from 15 to 32 GW, increased numbers of IBA1+ cells correlate with decreasing densities of (**d**) Nestin+ radial glia, (**e**) Ki67+ proliferating cells, and (**f**) Ki67+ SOX2+ neural progenitors. Gray regions in (**d**) and (**e**) indicate SEM intervals.

(**g**) Confocal images show IBA1+ cells in the human GE engulfing fragments of cleaved Caspase 3+ apoptotic cells.
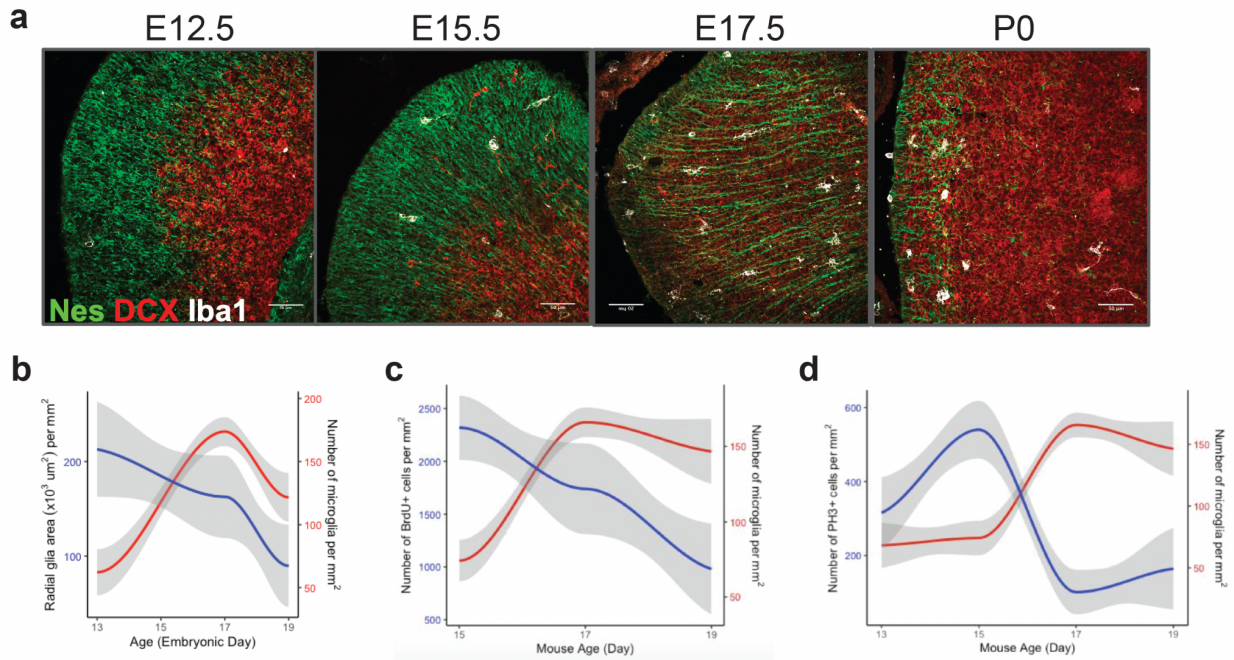
Figure 4.2: IBA1+ cell density negatively correlates with densities of radial glia and proliferating cells in the embryonic mouse GE.
(**a**) Confocal images show abundant IBA1+ cells in neurogenic niches in the mouse GE enriched with Nestin+ radial glia and DCX+ young neurons.
(**b-d**) Quantifications show that from E15.5 to E17.5, increased numbers of IBA1+ cells correlate with decreasing densities of (**b**) Nestin+ radial glia, (**c**) BrdU+ proliferating cells, and (**d**) PH3+ mitotic cells. Gray regions in (**b-d**) indicate SEM intervals.
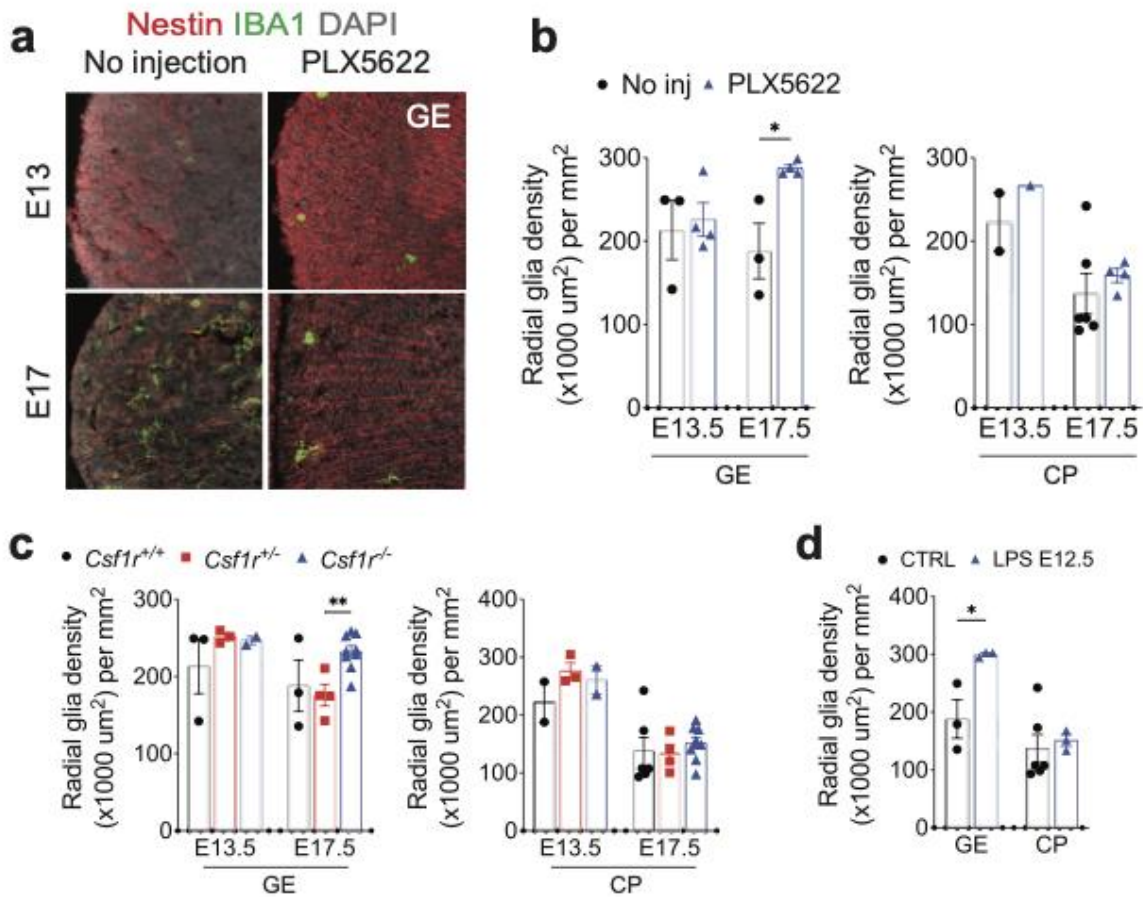
Figure 4.3: IBA1+ cells selectively prune radial glia in the embryonic GE.
(**a**) Confocal images show overgrowth of Nestin+ radial glia at E17.5 as a result of IBA1+ cell depletion by CSF1R inhibitor PLX5622.
(**b**) Quantification of radial glia density in GE and CP of mice with no injection or injected with PLX5622.
(**c**) Quantification of radial glia density in GE and CP of Csf1r+/+, Csf1r+/-, Csf1r-/- mice.
(**d**) Quantification of radial glia density at E17.5 in the GE and CP of control (CTRL) mice and those injected with lipopolysaccharide (LPS) at E12.5.
Error bars in (**b-d**) indicate SEM.
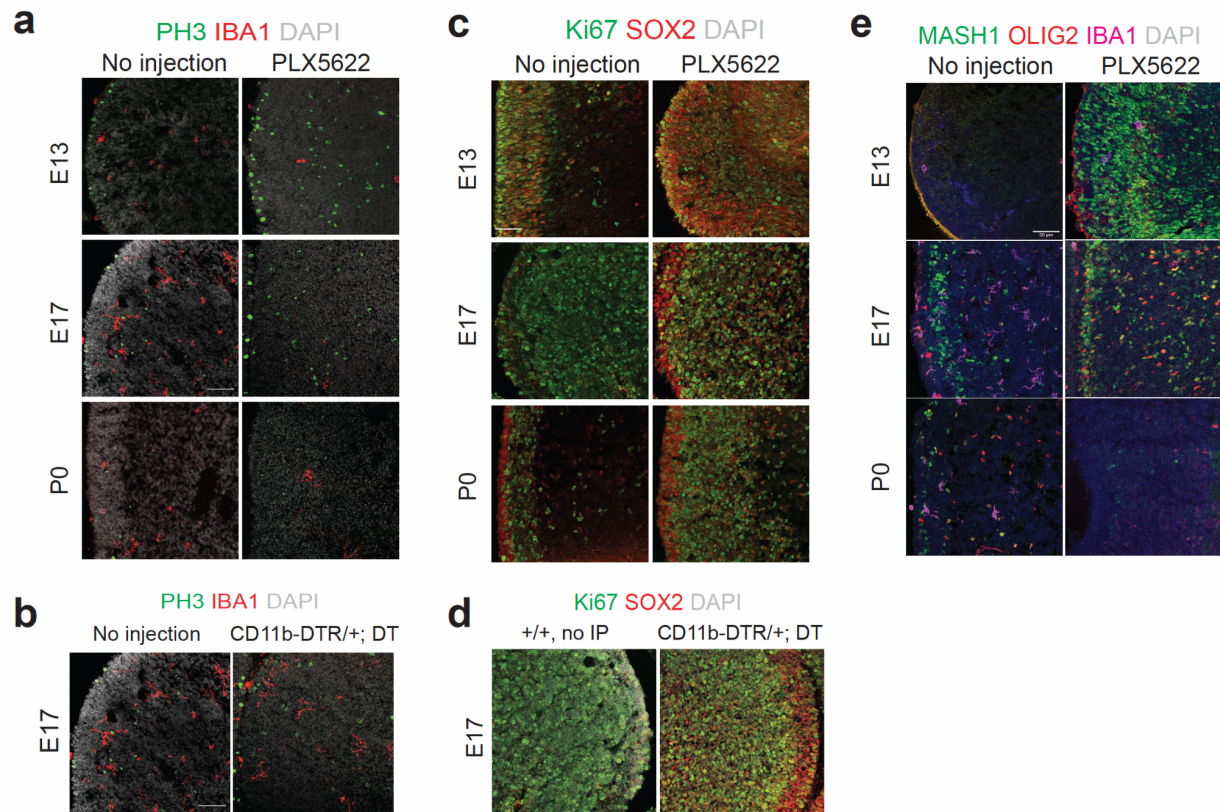
Figure 4.4: IBA1⁺ cell depletion leads to dysregulated positioning of proliferating cells and neural progenitors.

(**a, b**) Confocal images show increased density and perturbed layering of PH3⁺ mitotic cells in the GE as a result of IBA1⁺ cell depletion in (**a**) PLX5622-injected mice and (**b**) diphtheria toxin (DT)-injected CD11b-DTR/+ mice.

(**c, d**) Confocal images show perturbed layering of Ki67⁺ proliferating cells and SOX2⁺ neural progenitors in the GE as a result of IBA1⁺ cell depletion in (**c**) PLX5622-injected mice and (**d**) diphtheria toxin (DT)-injected CD11b-DTR/+ mice.

(**e**) Confocal images show increased density and perturbed layering of MASH1⁺ neural progenitors in the GE as a result of IBA1⁺ cell depletion in PLX5622-injected mice.
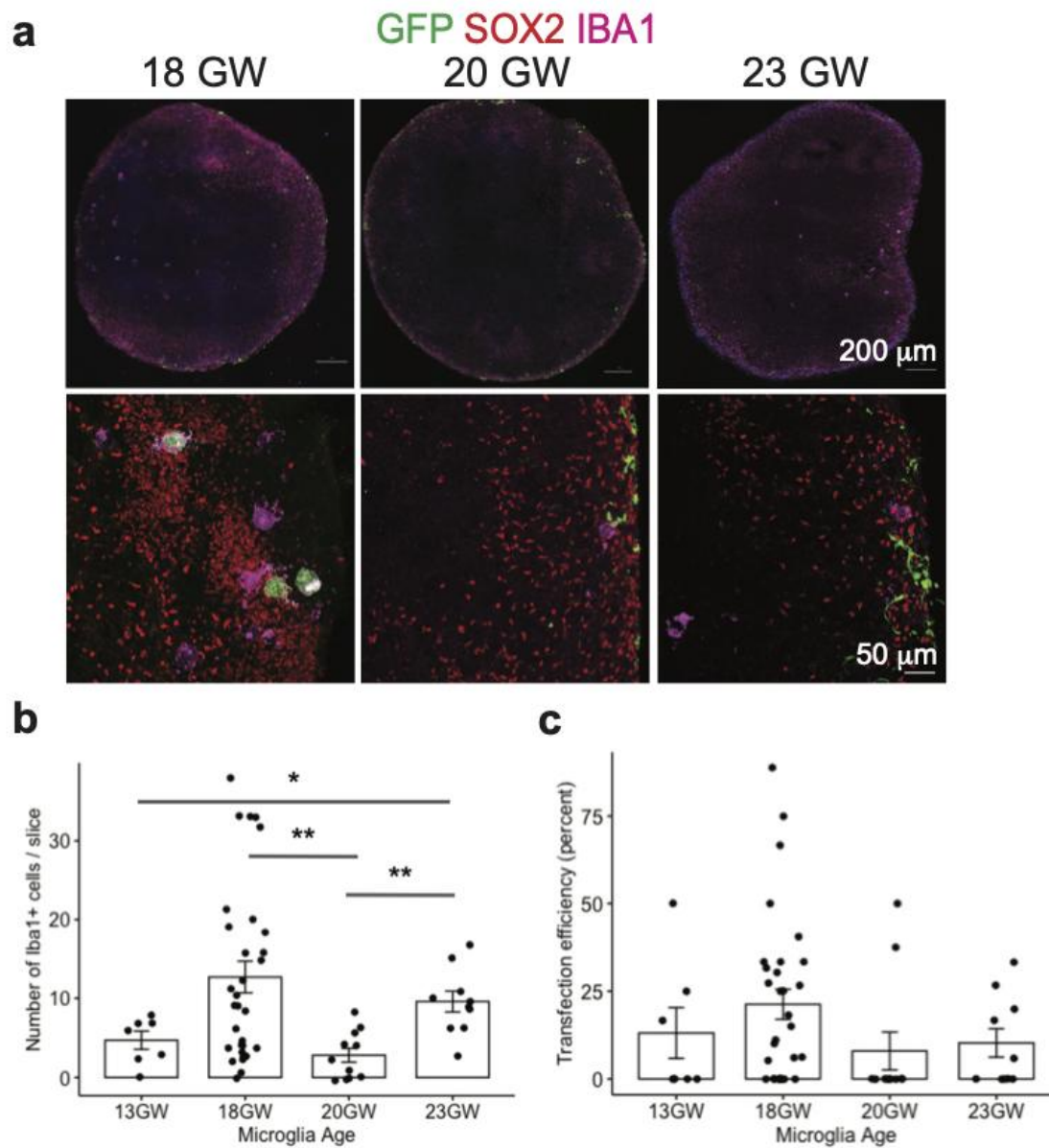
Figure 4.5: Amoeboid IBA1⁺ cells are found close to SOX2⁺ cell clusters after transplantation into neural organoids.

(**a**) Confocal images show amoeboid IBA1⁺ cells close to SOX2⁺ neural progenitor clusters upon transplantation into neural organoids.

(**b**) Quantifications show densities of IBA1⁺ cells from 13 to 23 GW transplanted into neural organoids.

(**c**) Quantifications show transfection efficiency of AAV-CMV-GFP in IBA1⁺ cells from 13 to 23 GW.

Error bars in (**b, c**) indicate SEM.

Methods and Materials

For the following methods, please see the end of Chapter 3 for details:

- Human tissue collection and Animals

- Secondary antibodies and Immunofluorescent staining

- Confocal imaging, processing and quantifications

- Fluorescence-activated cell sorting (FACS)

- Statistical Analyses

Additional methods and materials

Primary antibodies: Mouse anti-SOX2 (Santa Cruz Biotechnology, sc-365823, 1:200), Mouse anti-Nestin (Millipore, MAB5326, 1:500), Chicken anti-Nestin (Novus Biological, NB100-1604, 1:200), Rabbit anti-DCX (Abcam, ab18723, 1:200), Rat anti-Phospho-Histone 3 (Abcam, ab10543, 1:200), Rabbit anti-Ki67 (Abcam, ab16667, 1:200), Rabbit anti-MASH1 (Abcam, ab74065, 1:250), Mouse anti-OLIG2 (Millipore, MABN50, 1:500), Chicken anti-GFP (Aves Labs, GFP-1020, 1:500).

Animals

BrdU injections: BrdU was intraperitoneally injected into wild-type pregnant dams, and embryos were collected 30 minutes after.

iPSC and Organoid Culture (adapted from Bhaduri et al., 2021)

Human induced pluripotent stem cells (iPSCs) from the H28126 line were maintained using feeder-free conditions on Matrigel (BD) coated dishes in mTESR

(Stem Cell Technologies) medium. iPSCs were differentiated using a modified Sasai organoid protocol (Kadoshima et al., 2013) for directed telencephalon differentiation. iPSCs were dissociated using Accutase (Stem Cell Technologies) and aggregated into 96 well v-bottom low adhesion plates (S-bio). Aggregates were cultured in media containing Glasgow-MEM, 20% Knockout Serum Replacer, 0.1mM NEAA, 1mM sodium pyruvate, 0.1mM β-ME, 100 U/mL penicillin/streptomycin and supplemented with Rho Kinase, Wnt and TGFβ inhibitors, 20uM Y-27632 (Tocris), 3uM IWR1endo (Cayman), and 5uM SB431542, respectively (Tocris). Rho Kinase inhibitor was removed after 6 days. Media was changed every other day throughout differentiation. After 18 days, organoids were transferred into 6 well low-adhesion plates in media containing DMEM/F12 with 1x Glutamax, 1x N2, 1x Lipid Concentrate, and 100 U/mL penicillin/streptomycin. After five weeks, organoids are matured in media containing DMEM/F12 with Glutamax, 1x N2, 1x Lipid Concentrate, 100 U/mL penicillin/streptomycin, 10x Fetal Bovine Serum (Hyclone), 5ug/ml Heparin and 0.5% Growth factor-reduced Matrigel. After 10 weeks the concentration of Matrigel is increased to 1% and the media is additionally supplemented with 1x B-27. CD45^{+} CD11b^{+} cells (isolation method described previously at the end of Chapter 3) was then added to 8 week-old organoids at a concentration of 60,000 microglia per organoid. Histological analyses were carried out at 3 weeks after microglia transplantation.

Acknowledgements

Chapter 5: Conclusion and Future Directions

Conclusion

The study investigates the role of immune cells, specifically macrophages and microglia, in angiogenesis and neurogenesis during brain development and their contribution to germinal matrix hemorrhage (GMH) in preterm infants. Previous work suggested a positive role of immune cells in cerebrovascular formation, but the current study explores region- and stage-dependent differences in angiogenesis facilitated by microglia and macrophages. Our results reveal that immune cells play a crucial role in promoting complex vascular networks in the ganglionic eminence/germinal matrix of the prenatal brain. In GMH cases, activated neutrophils and monocytes disrupt the nascent vasculature, contributing to hemorrhage. This study identifies specific mechanisms, such as the production of bactericidal factors (AZU1, ELANE) and proinflammatory signals (CXCL16), through which immune-vascular interactions lose their homeostasis, leading to GMH. Additionally, it explores how altered microglia states negatively regulate radial glia density and affect neural progenitor positioning. Overall, this study provides valuable insights into the intricate tripartite interactions among immune, vascular, and neuronal cells during brain development and their implications for pathogenesis in GMH.

Future Directions

Despite our comprehensive studies, there remain many topics to be further investigated. First, nascent vasculatures in the human GE during the second trimester contain an ensemble of immature endothelial and mural cells that exhibit dynamic

stage-dependent transcriptomic changes and metabolic profiles (Crouch et al., 2022).

The intrinsic properties of these vascular cells, when challenged with exogenous insults, such as hypoxia, may weaken the nascent vasculature. These conditions could activate and attract immune cells, such as neutrophils and monocytes, which can further exacerbate hemorrhage. Second, given the intricate interplay among immune cells, vascular cells, and neural stem/progenitor cells, it remains unclear how disruption to any component in this tripartite relationship due to infection, inflammation, and/or hypoxic-ischemic injury could impact the homeostatic interactions between angiogenesis and neurogenesis in the GE. Finally, the direct interaction between CXCL16 in subsets of CD45$^+$ cells and S1PR1 in endothelial cells in GMH cases remains unclear. Future studies are required to delineate this relationship.

References

Andreatta, M., Corria-Osorio, J., Müller, S., Cubas, R., Coukos, G., & Carmona, S. J. (2021). Interpretation of T cell states from single-cell transcriptomics data using reference atlases. Nature communications, 12(1), 2965.

Antony, J. M., Paquin, A., Nutt, S. L., Kaplan, D. R., & Miller, F. D. (2011). Endogenous microglia regulate development of embryonic cortical precursor cells. Journal of Neuroscience Research, 89(3), 286–298.

Ballabh P. (2010). Intraventricular hemorrhage in premature infants: mechanism of disease. Pediatric research, 67(1), 1–8.

Ballabh P. (2014). Pathogenesis and prevention of intraventricular hemorrhage. Clinics in perinatology, 41(1), 47–67.

Ballabh, P., & de Vries, L. S. (2021). White matter injury in infants with intraventricular haemorrhage: mechanisms and therapies. Nature Reviews Neurology, 17(4), 199–214.

Barger, N., Keiter, J., Kreutz, A., Krishnamurthy, A., Weidenthaler, C., Martínez-Cerdeño, V., Tarantal, A. F., & Noctor, S. C. (2019). Microglia: An Intrinsic Component of the Proliferative Zones in the Fetal Rhesus Monkey (Macaca mulatta) Cerebral Cortex. Cerebral cortex, 29(7), 2782–2796.

Bassan, H., Limperopoulos, C., Visconti, K., Mayer, D. L., Feldman, H. A., Avery, L., Benson, C. B., Stewart, J., Ringer, S. A., Soul, J. S., Volpe, J. J., & du Plessis, A. J. (2007). Neurodevelopmental outcome in survivors of periventricular hemorrhagic infarction. Pediatrics, 120(4), 785–792.

Bennett, M. L., Bennett, F. C., Liddelow, S. A., Ajami, B., Zamanian, J. L., Fernhoff, N. B., Mulinyawe, S. B., Bohlen, C. J., Adil, A., Tucker, A., Weissman, I. L., Chang, E. F., Li, G., Grant, G. A., Hayden Gephart, M. G., & Barres, B. A. (2016). New tools for studying microglia in the mouse and human CNS. Proceedings of the National Academy of Sciences of the United States of America, 113(12), E1738–E1746.

Bhaduri A, Di Lullo E, Jung D, Müller S, Crouch EE, Espinosa CS, Ozawa T, Alvarado B, Spatazza J, Cadwell CR, Wilkins G, Velmeshev D, Liu SJ, Malatesta M, Andrews MG, Mostajo-Radji MA, Huang EJ, Nowakowski TJ, Lim DA, Diaz A, Raleigh DR, Kriegstein AR. Outer Radial Glia-like Cancer Stem Cells Contribute to Heterogeneity of Glioblastoma. Cell Stem Cell. 2020 Jan 2;26(1):48-63.e6.

Bisht, K., Okojie, K. A., Sharma, K., Lentferink, D. H., Sun, Y. Y., Chen, H. R., Uweru, J. O., Amancherla, S., Calcuttawala, Z., Campos-Salazar, A. B., Corliss, B., Jabbour, L., Benderoth, J., Friestad, B., Mills, W. A., 3rd, Isakson, B. E., Tremblay, M. È., Kuan, C. Y., & Eyo, U. B. (2021). Capillary-associated microglia regulate vascular structure and function through PANX1-P2RY12 coupling in mice. Nature communications, 12(1), 5289.

Browaeys, R., Saelens, W., & Saeys, Y. (2020). NicheNet: modeling intercellular communication by linking ligands to target genes. Nature Methods, 17(2), 159–162.

Burn, G. L., Foti, A., Marsman, G., Patel, D. F., & Zychlinsky, A. (2021). The Neutrophil. Immunity, 54(7), 1377–1391.

Butovsky, O., Jedrychowski, M. P., Moore, C. S., Cialic, R., Lanser, A. J., Gabriely, G.,

Koeglsperger, T., Dake, B., Wu, P. M., Doykan, C. E., Fanek, Z., Liu, L., Chen, Z.,

Rothstein, J. D., Ransohoff, R. M., Gygi, S. P., Antel, J. P., & Weiner, H. L.

(2014). Identification of a unique TGF-β-dependent molecular and functional

signature in microglia. Nature Neuroscience, 17(1), 131–143.

Buttgereit, A., Lelios, I., Yu, X., Vrohlings, M., Krakoski, N. R., Gautier, E. L.,

Nishinakamura, R., Becher, B., & Greter, M. (2016). Sall1 is a transcriptional

regulator defining microglia identity and function. Nature Immunology, 17(12),

1397–1406.

Casano, A. M., Albert, M., & Peri, F. (2016). Developmental Apoptosis Mediates Entry

and Positioning of Microglia in the Zebrafish Brain. Cell reports, 16(4), 897–906.

Crouch, E. E., Bhaduri, A., Andrews, M. G., Cebrian-Silla, A., Diafos, L. N., Birrueta, J.

O., Wedderburn-Pugh, K., Valenzuela, E. J., Bennett, N. K., Eze, U. C.,

Sandoval-Espinosa, C., Chen, J., Mora, C., Ross, J. M., Howard, C. E.,

Gonzalez-Granero, S., Lozano, J. F., Vento, M., Haeussler, M., Paredes, M. F., …

Huang, E. J. (2022). Ensembles of endothelial and mural cells promote

angiogenesis in prenatal human brain. Cell, 185(20), 3753–3769.

Cui, J., Shipley, F. B., Shannon, M. L., Alturkistani, O., Dani, N., Webb, M. D., Sugden,

A. U., Andermann, M. L., & Lehtinen, M. K. (2020). Inflammation of the

Embryonic Choroid Plexus Barrier following Maternal Immune Activation.

Developmental Cell, 55(5), 617–628.

Cunningham, C. L., Martínez-Cerdeño, V., & Noctor, S. C. (2013). Microglia regulate the

number of neural precursor cells in the developing cerebral cortex. The Journal

of Neuroscience, 33(10), 4216–4233.

Cyster, J. G., & Schwab, S. R. (2012). Sphingosine-1-phosphate and lymphocyte

egress from lymphoid organs. Annual Review of Immunology, 30, 69–94.

Darash-Yahana, M., Gillespie, J. W., Hewitt, S. M., Chen, Y. Y., Maeda, S., Stein, I.,

Singh, S. P., Bedolla, R. B., Peled, A., Troyer, D. A., Pikarsky, E., Karin, M., &

Farber, J. M. (2009). The chemokine CXCL16 and its receptor, CXCR6, as

markers and promoters of inflammation-associated cancers. PloS One, 4(8),

e6695.

Di Marco, B., Crouch, E. E., Shah, B., Duman, C., Paredes, M. F., Ruiz de Almodovar,

C., Huang, E. J., & Alfonso, J. (2020). Reciprocal Interaction between Vascular

Filopodia and Neural Stem Cells Shapes Neurogenesis in the Ventral

Telencephalon. Cell Reports, 33(2), 108256.

Dumas, A. A., Borst, K., & Prinz, M. (2021). Current tools to interrogate microglial

biology. Neuron, 109(18), 2805–2819.

Edens, H. A., & Parkos, C. A. (2003). Neutrophil transendothelial migration and

alteration in vascular permeability: focus on neutrophil-derived azurocidin.

Current Opinion in Hematology, 10(1), 25–30.

Efremova, M., Vento-Tormo, M., Teichmann, S. A., & Vento-Tormo, R. (2020).

CellPhoneDB: inferring cell-cell communication from combined expression of

multi-subunit ligand-receptor complexes. Nature Protocols, 15(4), 1484–1506.

Egesa, W. I., Odoch, S., Odong, R. J., Nakalema, G., Asiimwe, D., Ekuk, E.,

    Twesigemukama, S., Turyasiima, M., Lokengama, R. K., Waibi, W. M.,

    Abdirashid, S., Kajoba, D., & Kumbakulu, P. K. (2021). Germinal

    Matrix-Intraventricular Hemorrhage: A Tale of Preterm Infants. International

    Journal of Pediatrics, 2021, 6622598.

Fantin, A., Vieira, J. M., Gestri, G., Denti, L., Schwarz, Q., Prykhozhij, S., Peri, F.,

    Wilson, S. W., & Ruhrberg, C. (2010). Tissue macrophages act as cellular

    chaperones for vascular anastomosis downstream of VEGF-mediated endothelial

    tip cell induction. Blood, 116(5), 829–840.

Friebel, E., Kapolou, K., Unger, S., Núñez, N. G., Utz, S., Rushing, E. J., Regli, L.,

    Weller, M., Greter, M., Tugues, S., Neidert, M. C., & Becher, B. (2020).

    Single-Cell Mapping of Human Brain Cancer Reveals Tumor-Specific Instruction

    of Tissue-Invading Leukocytes. Cell, 181(7), 1626–1642.

Gerhardt, T., & Ley, K. (2015). Monocyte trafficking across the vessel wall.

    Cardiovascular Research, 107(3), 321–330.

Ginhoux, F., Greter, M., Leboeuf, M., Nandi, S., See, P., Gokhan, S., Mehler, M. F.,

    Conway, S. J., Ng, L. G., Stanley, E. R., Samokhvalov, I. M., & Merad, M. (2010).

    Fate mapping analysis reveals that adult microglia derive from primitive

    macrophages. Science, 330(6005), 841–845.

Gosselin, D., Skola, D., Coufal, N. G., Holtman, I. R., Schlachetzki, J. C. M., Sajti, E.,

    Jaeger, B. N., O'Connor, C., Fitzpatrick, C., Pasillas, M. P., Pena, M., Adair, A.,

    Gonda, D. D., Levy, M. L., Ransohoff, R. M., Gage, F. H., & Glass, C. K. (2017).

An environment-dependent transcriptional network specifies human microglia
identity. Science, 356(6344), eaal3222.

Hammond, T. R., Dufort, C., Dissing-Olesen, L., Giera, S., Young, A., Wysoker, A.,
Walker, A. J., Gergits, F., Segel, M., Nemesh, J., Marsh, S. E., Saunders, A.,
Macosko, E., Ginhoux, F., Chen, J., Franklin, R. J. M., Piao, X., McCarroll, S. A.,
& Stevens, B. (2019). Single-Cell RNA Sequencing of Microglia throughout the
Mouse Lifespan and in the Injured Brain Reveals Complex Cell-State Changes.
Immunity, 50(1), 253–271.

Han, C. Z., Li, R. Z., Hansen, E., Trescott, S., Fixsen, B. R., Nguyen, C. T., Mora, C. M.,
Spann, N. J., Bennett, H. R., Poirion, O., Buchanan, J., Warden, A. S., Xia, B.,
Schlachetzki, J. C. M., Pasillas, M. P., Preissl, S., Wang, A., O'Connor, C.,
Shriram, S., Kim, R., … Coufal, N. G. (2023). Human microglia maturation is
underpinned by specific gene regulatory networks. Immunity, 56(9), 2152–2171.

Hansen, D. V., Lui, J. H., Flandin, P., Yoshikawa, K., Rubenstein, J. L., Alvarez-Buylla,
A., & Kriegstein, A. R. (2013). Non-epithelial stem cells and cortical interneuron
production in the human ganglionic eminences. Nature Neuroscience, 16(11),
1576–1587.

Haruwaka, K., Ikegami, A., Tachibana, Y., Ohno, N., Konishi, H., Hashimoto, A.,
Matsumoto, M., Kato, D., Ono, R., Kiyama, H., Moorhouse, A. J., Nabekura, J., &
Wake, H. (2019). Dual microglia effects on blood brain barrier permeability
induced by systemic inflammation. Nature communications, 10(1), 5816.

Holtman, I. R., Skola, D., & Glass, C. K. (2017). Transcriptional control of microglia

    phenotypes in health and disease. The Journal of Clinical Investigation, 127(9),

    3220–3229.

Howson, C. P., Kinney, M. V., McDougall, L., Lawn, J. E., & Born Too Soon Preterm

    Birth Action Group (2013). Born too soon: preterm birth matters. Reproductive

    Health, 10 Suppl 1(Suppl 1), S1.

Jain, S., Baer, R. J., McCulloch, C. E., Rogers, E., Rand, L., Jelliffe-Pawlowski, L., &

    Piao, X. (2021). Association of Maternal Immune Activation during Pregnancy

    and Neurologic Outcomes in Offspring. The Journal of Pediatrics, 238, 87–93.

Kadoshima T, Sakaguchi H, Nakano T, Soen M, Ando S, Eiraku M, Sasai Y.

    Self-organization of axial polarity, inside-out layer pattern, and species-specific

    progenitor dynamics in human ES cell-derived neocortex. Proc Natl Acad Sci U S

    A. 2013 Dec 10;110(50):20284-9.

Keren-Shaul, H., Spinrad, A., Weiner, A., Matcovitch-Natan, O., Dvir-Szternfeld, R.,

    Ulland, T. K., David, E., Baruch, K., Lara-Astaiso, D., Toth, B., Itzkovitz, S.,

    Colonna, M., Schwartz, M., & Amit, I. (2017). A Unique Microglia Type

    Associated with Restricting Development of Alzheimer's Disease. Cell, 169(7),

    1276–1290.

Kierdorf, K., Erny, D., Goldmann, T., Sander, V., Schulz, C., Perdiguero, E. G.,

    Wieghofer, P., Heinrich, A., Riemke, P., Hölscher, C., Müller, D. N., Luckow, B.,

    Brocker, T., Debowski, K., Fritz, G., Opdenakker, G., Diefenbach, A., Biber, K.,

    Heikenwalder, M., Geissmann, F., … Prinz, M. (2013). Microglia emerge from

erythromyeloid precursors via Pu.1- and Irf8-dependent pathways. Nature

neuroscience, 16(3), 273–280.

Kracht, L., Borggrewe, M., Eskandar, S., Brouwer, N., Chuva de Sousa Lopes, S. M.,

Laman, J. D., Scherjon, S. A., Prins, J. R., Kooistra, S. M., & Eggen, B. J. L.

(2020). Human fetal microglia acquire homeostatic immune-sensing properties

early in development. Science, 369(6503), 530–537.

Li, J., Chen, K., Zhu, L., & Pollard, J. W. (2006). Conditional deletion of the colony

stimulating factor-1 receptor (c-fms proto-oncogene) in mice. Genesis, 44(7),

328–335.

Li, Q., & Barres, B. A. (2018). Microglia and macrophages in brain homeostasis and

disease. Nature reviews. Immunology, 18(4), 225–242.

Li, Q., Cheng, Z., Zhou, L., Darmanis, S., Neff, N. F., Okamoto, J., Gulati, G., Bennett,

M. L., Sun, L. O., Clarke, L. E., Marschallinger, J., Yu, G., Quake, S. R.,

Wyss-Coray, T., & Barres, B. A. (2019). Developmental Heterogeneity of

Microglia and Brain Myeloid Cells Revealed by Deep Single-Cell RNA

Sequencing. Neuron, 101(2), 207–223.

Ma, T., Wang, C., Wang, L., Zhou, X., Tian, M., Zhang, Q., Zhang, Y., Li, J., Liu, Z., Cai,

Y., Liu, F., You, Y., Chen, C., Campbell, K., Song, H., Ma, L., Rubenstein, J. L., &

Yang, Z. (2013). Subcortical origins of human and monkey neocortical

interneurons. Nature Neuroscience, 16(11), 1588–1597.

Marín-Teva, J. L., Dusart, I., Colin, C., Gervais, A., van Rooijen, N., & Mallat, M. (2004).

Microglia promote the death of developing Purkinje cells. Neuron, 41(4),

535–547.

Masuda, T., Amann, L., Monaco, G., Sankowski, R., Staszewski, O., Krueger, M., Del

    Gaudio, F., He, L., Paterson, N., Nent, E., Fernández-Klett, F., Yamasaki, A.,

    Frosch, M., Fliegauf, M., Bosch, L. F. P., Ulupinar, H., Hagemeyer, N., Schreiner,

    D., Dorrier, C., Tsuda, M., … Prinz, M. (2022). Specification of CNS macrophage

    subsets occurs postnatally in defined niches. Nature, 604(7907), 740–748.

McCrea, H. J., & Ment, L. R. (2008). The diagnosis, management, and postnatal

    prevention of intraventricular hemorrhage in the preterm neonate. Clinics in

    Perinatology, 35(4), 777–vii.

Menassa, D. A., & Gomez-Nicola, D. (2018). Microglial Dynamics During Human Brain

    Development. Frontiers in immunology, 9, 1014.

Mendelson, K., Evans, T., & Hla, T. (2014). Sphingosine 1-phosphate signalling.

    Development, 141(1), 5–9.

Mondo, E., Becker, S. C., Kautzman, A. G., Schifferer, M., Baer, C. E., Chen, J., Huang,

    E. J., Simons, M., & Schafer, D. P. (2020). A Developmental Analysis of

    Juxtavascular Microglia Dynamics and Interactions with the Vasculature. The

    Journal of Neuroscience, 40(34), 6503–6521.

Monier, A., Evrard, P., Gressens, P., & Verney, C. (2006). Distribution and differentiation

    of microglia in the human encephalon during the first two trimesters of gestation.

    The Journal of Comparative Neurology, 499(4), 565–582.

Mrdjen, D., Pavlovic, A., Hartmann, F. J., Schreiner, B., Utz, S. G., Leung, B. P., Lelios,

    I., Heppner, F. L., Kipnis, J., Merkler, D., Greter, M., & Becher, B. (2018).

    High-Dimensional Single-Cell Mapping of Central Nervous System Immune Cells

Reveals Distinct Myeloid Subsets in Health, Aging, and Disease. Immunity, 48(2), 380–395.

Noctor, S. C., Flint, A. C., Weissman, T. A., Dammerman, R. S., & Kriegstein, A. R. (2001). Neurons derived from radial glial cells establish radial units in neocortex. Nature, 409(6821), 714–720.

Paredes, M. F., Mora, C., Flores-Ramirez, Q., Cebrian-Silla, A., Del Dosso, A., Larimer, P., Chen, J., Kang, G., Gonzalez Granero, S., Garcia, E., Chu, J., Delgado, R., Cotter, J. A., Tang, V., Spatazza, J., Obernier, K., Ferrer Lozano, J., Vento, M., Scott, J., Studholme, C., … Huang, E. J. (2022). Nests of dividing neuroblasts sustain interneuron production for the developing human brain. Science, 375(6579), eabk2346.

Park, Y. G., Sohn, C. H., Chen, R., McCue, M., Yun, D. H., Drummond, G. T., Ku, T., Evans, N. B., Oak, H. C., Trieu, W., Choi, H., Jin, X., Lilascharoen, V., Wang, J., Truttmann, M. C., Qi, H. W., Ploegh, H. L., Golub, T. R., Chen, S. C., Frosch, M. P., … Chung, K. (2018). Protection of tissue physicochemical properties using polyfunctional crosslinkers. Nature Biotechnology, 10.1038/nbt.4281.

Polacheck, W. J., Kutys, M. L., Tefft, J. B., & Chen, C. S. (2019). Microfabricated blood vessels for modeling the vascular transport barrier. Nature Protocols, 14(5), 1425–1454.

Preibisch, S., Saalfeld, S., Schindelin, J., & Tomancak, P. (2010). Software for bead-based registration of selective plane illumination microscopy data. Nature Methods, 7(6), 418–419.

Renier, N., Wu, Z., Simon, D. J., Yang, J., Ariel, P., & Tessier-Lavigne, M. (2014).
iDISCO: a simple, rapid method to immunolabel large tissue samples for volume
imaging. Cell, 159(4), 896–910.

Rezaie, P., Dean, A., Male, D., & Ulfig, N. (2005). Microglia in the cerebral wall of the
human telencephalon at second trimester. Cerebral cortex, 15(7), 938–949.

Shigemoto-Mogami, Y., Hoshikawa, K., Goldman, J. E., Sekino, Y., & Sato, K. (2014).
Microglia enhance neurogenesis and oligodendrogenesis in the early postnatal
subventricular zone. The Journal of Neuroscience, 34(6), 2231–2243.

Sirerol-Piquer, M. S., Cebrián-Silla, A., Alfaro-Cervelló, C., Gomez-Pinedo, U.,
Soriano-Navarro, M., & Verdugo, J. M. (2012). GFP immunogold staining, from
light to electron microscopy, in mammalian cells. Micron, 43(5), 589–599.

Smith, L. E., Shen, W., Perruzzi, C., Soker, S., Kinose, F., Xu, X., Robinson, G., Driver,
S., Bischoff, J., Zhang, B., Schaeffer, J. M., & Senger, D. R. (1999). Regulation of
vascular endothelial growth factor-dependent retinal neovascularization by
insulin-like growth factor-1 receptor. Nature Medicine, 5(12), 1390–1395.

Spangenberg, E., Severson, P. L., Hohsfield, L. A., Crapser, J., Zhang, J., Burton, E. A.,
Zhang, Y., Spevak, W., Lin, J., Phan, N. Y., Habets, G., Rymar, A., Tsang, G.,
Walters, J., Nespi, M., Singh, P., Broome, S., Ibrahim, P., Zhang, C., Bollag, G.,
… Green, K. N. (2019). Sustained microglial depletion with CSF1R inhibitor
impairs parenchymal plaque development in an Alzheimer's disease model.
Nature communications, 10(1), 3758.

Squarzoni, P., Oller, G., Hoeffel, G., Pont-Lezica, L., Rostaing, P., Low, D., Bessis, A., Ginhoux, F., & Garel, S. (2014). Microglia modulate wiring of the embryonic forebrain. Cell reports, 8(5), 1271–1279.

Ueno, M., Fujita, Y., Tanaka, T., Nakamura, Y., Kikuta, J., Ishii, M., & Yamashita, T. (2013). Layer V cortical neurons require microglial support for survival during postnatal development. Nature neuroscience, 16(5), 543–551.

Utz, S. G., See, P., Mildenberger, W., Thion, M. S., Silvin, A., Lutz, M., Ingelfinger, F., Rayan, N. A., Lelios, I., Buttgereit, A., Asano, K., Prabhakar, S., Garel, S., Becher, B., Ginhoux, F., & Greter, M. (2020). Early Fate Defines Microglia and Non-parenchymal Brain Macrophage Development. Cell, 181(3), 557–573.

Verney, C., Monier, A., Fallet-Bianco, C., & Gressens, P. (2010). Early microglial colonization of the human forebrain and possible involvement in periventricular white-matter injury of preterm infants. Journal of anatomy, 217(4), 436–448.

Volpe J. J. (2015). Impaired Neurodevelopmental Outcome After Mild Germinal Matrix-Intraventricular Hemorrhage. Pediatrics, 136(6), 1185–1187.

Publishing Agreement

It is the policy of the University to encourage open access and broad distribution of all theses, dissertations, and manuscripts. The Graduate Division will facilitate the distribution of UCSF theses, dissertations, and manuscripts to the UCSF Library for open access and distribution. UCSF will make such theses, dissertations, and manuscripts accessible to the public and will take reasonable steps to preserve these works in perpetuity.

I hereby grant the non-exclusive, perpetual right to The Regents of the University of California to reproduce, publicly display, distribute, preserve, and publish copies of my thesis, dissertation, or manuscript in any form or media, now existing or later derived, including access online for teaching, research, and public service purposes.

DocuSigned by:

Jiapei Chen

AB28923A44AD44C...   Author Signature

11/20/2023

Date